

https://dspace.org/

Microwave-assisted synthesis of Zeolite-based catalysts for pyrolysis of Lignocellosic biomass

Nyembe, Nhlanhla

2025

University of the Witwatersrand, Johannesburg

https://hdl.handle.net/10539/47599

Nyembe, Nhlanhla . (2025). Microwave-assisted synthesis of Zeolite-based catalysts for pyrolysis of Lignocellosic biomass [Master`s dissertation, University of the Witwatersrand, Johannesburg]. WIReDSpace. https://hdl.handle.net/10539/47599

Downloaded from a DSpace repository. https://dspace.org/



Microwave-assisted synthesis of Zeolite-based catalysts for pyrolysis of Lignocellosic biomass

MSc RESEARCH DISSERTATION

Prepared by

Nhlanhla Nyembe

474649

Submitted to

School of Chemical and Metallurgical Engineering, Faculty of Engineering and the Built Environment, University of the Witwatersrand, Johannesburg, South Africa

Supervisor(s): Prof. Y.M. Isa

March, 2025

DECLARATION

I hereby affirm that this dissertation is an original intellectual product of my individual labour, and all the resources I have utilized or cited have been duly recognized through comprehensive bibliographic citations.

I further affirm that I have rigorously submitted the dissertation in question to a comprehensive originality verification software. I can confidently attest that the similarity results align with the university's acceptable threshold for originality in academic work.

I declare that this dissertation is my own unaided work. It is being submitted to the degree of Master of Science in Engineering at the University of the Witwatersrand, Johannesburg. It has not been submitted before for any degree or examination to any other university.

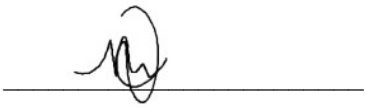

(Signature of candidate)

_____06th_____ day of _____May_____ year __2024_____.

ACKNOWLEDGMENTS

My sincere gratitude is extended to the following people and institutions for their contribution:

1. First, to my immediate family, who, above all, supported me throughout my journey.
2. My supervisor Prof. Y.M. Isa.
3. Dr. L. Shoko, from VUT, also made a remarkable contribution to this work.
4. Prof. L. Rutto, who linked me up with my current supervisor.
5. Mr. M. Phali, I am grateful for his support.
6. VUT for financial support, paid for my fees.
7. The Fuel and Petrochemical Synthesis (FPS) group that assisted with their valuable contributions and collaborations.
8. Microscopy and Microanalysis Unit (MMU) for access to a variety of analytical instrumentation.
9. Above all, sincere gratitude is extended to the University of the Witwatersrand (Wits) for all the opportunities it continues to grant me.

TABLE OF CONTENTS

LIST OF FIGURES vii
LIST OF TABLES ix
LIST OF ABBREVIATIONS, SYMBOLS, AND NOMENCLATURES x
ABSTRACT xiii
CHAPTER 1 1
1. Introduction 1
1.1. Background and Context 1
1.2. Problem Statement 3
1.3. Research Rationale 3
1.4. Research Objectives 4
1.4.1. Aim 4
1.4.2. Objectives 4
1.5. Structure of Thesis 4
References 5
CHAPTER 2 7
2. From Waste to Catalyst: Zeolite Synthesis and Application in Lignocellulosic Biomass Pyrolysis 7
2.1. Introduction 7
2.2. Lignocellulosic Biomass 9
2.2.1. Lignin 11
2.2.2. Cellulose 11
2.2.3. Hemicellulose 12
2.2.4. Major Sources of Biomass 13
2.3. Thermochemical Conversion of Biomass 14
2.4. Pyrolysis Using Zeolite-based Catalysts 15
2.5. Bottom-up Zeolite Synthesis Approaches 16
2.5.1. Hard Templating 16
2.5.2. Soft Templating 17
2.5.3. Non-Templating 17
2.6. Top-down Zeolite Synthesis Approaches 18
2.6.1. Demetallation Approach (dealumination and desilication) 18
2.6.2. Dealumination and Assembly Approach 19

2.6.3. Dissolution and Recrystallization 19
2.7. Modern Approaches to Zeolite Synthesis 20
2.7.1. Solvent-free Method 20
2.7.2. Green Starting Materials 20
2.7.3. Mesoporogen-free Method 21
2.8. Zeolite Influences in Catalytic Application 21
2.8.1. Zeolite Structure (crystalline framework, size, and shape) 21
2.8.2. Effect of Crystalline Framework, Size and Shape on Catalytic Performance 22
2.8.3. Active Acid Sites 24
2.8.4. Effect of Acid Sites on Catalytic Activity 25
2.8.5. Modification of Zeolite through Si/Al Ratio 26
2.8.6. Modification of Zeolite with Various Elements 26
2.9. Industrial Waste Resources for Zeolite Production 28
2.9.1. Coal Ash Residues 28
2.9.2. Fly Ash from Municipal Solid Waste Incinerator (MSWI) 30
2.9.3. Biomass Ash 30
2.9.4. Iron and Steel Slags 31
2.9.5. Non-ferrous Metallurgical Slags 32
2.9.6. Waste Foundry Sand (WFS) 33
2.9.7. Bauxite Residue 33
2.10. Microwave-assisted Pyrolysis 34
2.10.1. Microwave Theory 34
2.11. Conclusion 35
References 36
CHAPTER 3 52
3. Acid Leaching of Blast Furnace Slag for Enhanced Zeolite Synthesis 52
3.1. Introduction 53
3.2. Materials and Methods 54
3.2.1. Chemicals and Materials 54
3.2.2. Acid Leaching Process 54
3.2.3. Experimental Design 55
3.2.4. Zeolite Synthesis 56
3.2.5. Analytical Methods 56

3.3. Results and Discussion 57
3.3.1. Leaching Efficiency 57
3.3.2. Effect of Leaching Conditions 59
3.3.3. Chemical Composition of Powdered Samples 60
3.3.4. X-ray Diffraction Patterns of Powdered Samples 61
3.3.5. Scanning Electron Microscopy (SEM) Images of Powdered Samples 63
3.3.6. Fourier-Transform Infrared Spectroscopy (FTIR) 64
3.4. Conclusion 65
References 66
CHAPTER 4 68
4. Synthesis and Characterization of Zeolite-based Catalyst Derived From Slag Waste 68
4.1. Introduction 69
4.2. Materials and Methods 70
4.2.1. Chemical and Materials 70
4.2.2. Blast Furnace Slag Beneficiation 71
4.2.3. Microwave-assisted Hydrothermal Synthesis 71
4.3.4. Characterization Methods 72
4.3. Results and Discussion 73
4.3.1. Slag Beneficiation 73
4.3.2. Diffraction Patterns of the Synthesized Products 73
4.3.3. Morphology of the Synthesized Products 75
4.3.4. Framework Structure of Synthesized Products 76
4.3.5. Texture Properties of the Synthesized Properties 77
4.3.6. Chemical Composition of ZSM-5 79
4.4. Conclusion 80
References 81
CHAPTER 5 84
5. Catalytic Performance and Selectivity of Synthesized ZSM-5 Catalyst in Biomass Pyrolysis 84
5.1. Introduction 85
5.2. Materials and Methods 87
5.2.1. Chemicals and Materials 87
5.2.2. ZSM-5 Synthesis Method 87
5.2.3. Microwave-assisted Pyrolysis Experiments 88

5.2.4. Biomass and Catalyst Characterization 89
5.2.5. Pyrolysis Product Characterization 89
5.3. Results and Discussion 90
5.3.1. Proximate Analysis of Corn Cob (CC) 90
5.3.2. Diffraction Patterns of the Catalysts 90
5.3.3. Texture Properties of the Catalysts 91
5.3.4. Chemical Composition of the Catalysts 92
5.3.5. Effect of Temperature on Product Distribution 93
5.3.6. Effect of Catalyst-to-Biomass Ratio on Product Distribution 94
5.3.7. Effect of Time on Product Distribution 95
5.3.8. Bio-oil Conversion 96
5.3.9. Chemical Component Analysis of Bio-oil by GC-MS 97
5.3.10. Chemical Compounds Identified by GC-MS 98
5.3.11. Chemical Composition of Gases 99
5.4. Conclusion 100
References 100
CHAPTER 6 105
6.1. Overall Conclusion 105
6.1. Recommendations and Future Work 107
7. Appendices 108
7.1 Appendix A (Acid Leaching Experiments) 108
7.2. Appendix B (Microwave-assisted Pyrolysis Experiments) 110
7.3. Appendix C (Compounds Identified by GC-MS) 111

LIST OF FIGURES

Figure 2.1. Key sources of biomass. 10
Figure 2.2. Composition and pyrolysis reaction pathway of lignin [adapted from: Lu & Gu (2022)]. 11
Figure 2.3. Composition and pyrolysis reaction pathway of cellulose [adapted from: Lu & Gu (2022)]. 12
Figure 2.4. Composition and pyrolysis reaction pathway of hemicellulose [adapted from: Lu & Gu (2022)]. 13
Figure 2.5. Tetrahedrons Structure of ZSM-5 zeolite [adapted from Lounis & Belarbi (2018)]. (Copyright 2023, with permission from Elsevier). 22
Figure 2.6. Comparison between conventional and microwave heating [adapted from Morgan et al. (2017)]. (Copyright 2022, with permission from Elsevier). 35
Figure 3.1. Leaching experimental setup. 1) Flat-bottomed flask, 2) heating-magnetic stirring plate, 3) Allihn glass condenser, 4) Clamp stand, 5) HCl solution and 6) Raw slag. 55
Figure 3.2. Effect of various parameters on the leaching process based on Run 10. 60
Figure 3.3. Powder X-ray diffractograms: a) Blast furnace slag [BFS], b) pretreat slag [PTS], c) product derived from BFS, and d) product derived from PTS. 63
Figure 3.4. SEM micrographs: a) BFS, b) PTS, c) product synthesized from BFS, and d) product synthesized PTS. 64
Figure 3.5. FTIR spectra of powdered products. 65
Figure 4.1. Hydrothermal synthesis process. 1) heating-magnetic stirring plate, 2) glass beaker, 3) flat-bottomed flask, 4) glass condenser, 5) clamp stand, 6) deionized water, 7) deionized water and NaOH solution, 8) TPABr, 9) pretreated slag, and 10) microwave system. 72
Figure 4.2. XRD patterns of the powered samples: a) Effect of synthesis time at 180°C, b) Effect of synthesis temperature at 13h, and (●) Augite mineral. 75
Figure 4.3. SEM micro-images of powered samples at different synthesis times at 180°C… 76
Figure 4.4. FT-IT spectra of powdered samples: a) Effect of synthesis time at 180°C and b) Effect of synthesis temperature at 13h. 77
Figure 4.5. Nitrogen sorption isotherms of powdered samples. 79
Figure 5.1. Microwave-assisted pyrolysis setup: 1) nitrogen gas tank, 2) microwave lab station, 3) weflon base plate, 4) round-bottomed flask, 5) glass connecting tube, 6) Allihn condenser, 7) bio-oil collection vessel, and 8) gas collection bag. 88
Figure 5.2. XRD patterns of commercial and synthesized catalysts. 91

Figure 5.3. Physical adsorption isotherms. 92
Figure 5.4. Effect of pyrolysis temperature on Product Distribution (time of 3 min & catalyst-to-biomass ratio of 1:9). 94
Figure 5.5. Effect of catalyst-to-biomass ratio on product distribution (time of 3 min & temperature of 350°C). 95
Figure 5.6. Effect of time on product distribution (temperature of 350°C & catalyst-to-biomass ratio of 1:9). 96
Figure 5.7. Effect of catalyst type on bio-oil conversion (350°C, 3 min, and 1:9). 97
Figure 5.8. GC-MS analysis of the chemical composition of bio-oils. 98

LIST OF TABLES

Table 2.1. A summary of compositions (wt.%) for low-cost industrial wastes for zeolite production [adapted from Sayehi et al. (2020)]. (Copyright 2022, with permission from Elsevier). 28

Table 2.2. Typical coal fly ash chemical composition [adapted from Zhang et al. (2022)]. (Copyright 2022, with permission from Elsevier). 29

Table 2.3. Typical chemical compositions of EAF, BOF, and BF slags [adapted from Jiang et al. (2018) and Manchisi et al. (2020)]. (Copyright 2022, with permission from Elsevier). 32

Table 3.1. Leaching experimental matrix..... 56

Table 3.2. Acid leaching efficiency. 58

Table 3.3. Chemical composition of BFS. 61

Table 4.1. Chemical analysis of BFS and PTS as determined by XRF. 73

Table 4.2. Textural and structural properties of the powdered samples. 78

Table 4.3. Chemical composition of ZSM-5..... 80

Table 5.1. Proximate analysis of corn cob. 90

Table 5.2. Structural properties of commercial and synthesized catalysts..... 92

Table 5.3. Chemical composition of the catalysts..... 93

Table 5.4. Major compounds identified by GC-MS: Bio-oil from microwave-assisted pyrolysis of corn cob at maximum conditions..... 99

Table 5.5. Pyrolysis gas composition..... 100

LIST OF ABBREVIATIONS, SYMBOLS, AND NOMENCLATURES

AAS	Atomic absorption spectrometry
AC	Activated carbon
AR	Analytical reagent
BB	Box Behnken
BEA	Beta zeolite
BFS	Blast furnace slag
BOF	Basic oxygen furnace
CC	Corn cob
CEC	Cation exchange capacity
CFA	Coal fly ash
Comm.	Commercial
CTA	Cetyltrimethylammonium
CTAB	Cetyltrimethylammonium bromide
CTACl	Cetyltrimethylammonium chloride
D_5R	Double five ring
DGC	Dry gel conversion
DIPB	Di-ispropylbenzene
EAF	Electric arc furnace
EDS	Energy-dispersive spectroscopy
FAU	Faujasite zeolite
FC	Fixed carbon
FTIR	Fourier-Transform Infrared Spectroscopy
GAC	Granular activated carbon
GC	Gas chromatography
GC-MS	Gas chromatography–mass spectrometry
HV	Heating value
HZSM-5	Hierarchical Zeolite Socony Mobil-5
LTA	Linde Type A zeolite
MAH	Monoaromatic hydrocarbons

MAS NMR	Magic angle spinning Nuclear magnetic resonance
MC	Moisture content
MFI	Mobil five zeolite
MgO	Magnesium oxide
min	Minute
MSWI	Municipal Solid Waste Incinerator
OSDA	Organic structure directing agent
P/E	Propylene to ethylene ratio
PSA	Paper sludge ash
PTS	pretreated slag
RE	Rare earth
RHA	Rice husk ash
SA	South Africa
SDA	Structure directing agent
SEM	Scanning electron microscopy
Si/Al ratio	Silicon to aluminium molar ratio
Synth.	Synthesis
TEOS	Tetraethyl orthosilicate
TGA	Thermogravimetric analysis
TIPB	Tri-isopropylbenzene
TO_4	Tetrahedra building block
TPABr	Tetrapropylammonium bromide
TPAOH	Tetrapropylammonium hydroxide
USA	United States of America
VM	Volatile matter
V_{macro}	Macroporous volume
V_{micro}	Microporous volume
V_{TOT}	Total volume
WFS	Waste foundry sand
wt%	Weight percentage

XRD	X-ray diffraction
XRF	X-ray fluorescence
ZSM-5	Zeolite Socony Mobil-5

ABSTRACT

This work evaluated blast furnace slag as a potential industrial waste resource for zeolite synthesis. The primary objective of employing blast furnace slag was to develop a sustainable downstream beneficiation process for the iron and steel manufacturing industry to curb its impact on the environment. This entailed the beneficiation of the slag for the removal of impurities (Ca and Mg), the use of the pretreated slag as a silicon and aluminum precursor for the synthesis of ZSM-5, and the catalytic evaluation of the synthesized ZSM-5 for the conversion of lignocellulosic biomass (corn cob) into bio-oil.

The major compounds found in the slag waste were Al_2O_3 (16.1 wt.%), CaO (30.6 wt.%), SiO_2 (35.1 wt.%), and MgO (10.5 wt.%). The slag waste was pretreated using acid leaching to reduce the concentration of CaO and MgO to 4.83 wt.% and 2.54 wt.%, respectively. The optimal acid leaching conditions resulted in a leaching efficiency of 71.1% and 80.4% for Mg and Ca, respectively. The maximum leaching efficiencies were achieved using the following optimum leaching conditions: solids concentration of 8 wt.%, leaching time of 90 min, and HCl concentration of 3 mol/L. Morphological analysis of the raw and pretreated slags revealed that both slags consisted of irregular-shaped stonelike formations with diverse particle sizes and fibrous surfaces. However, the mineral composition was found to be akermanite for the raw slag and augite for the pretreated slag.

A comparative study was conducted by utilizing both slags (raw and pretreated) in the synthesis of zeolitic materials, and it was found that the concentration of CaO and MgO in the starting material significantly affected the zeolite synthesis process. Therefore, the microwave-assisted hydrothermal synthesis technique was used to convert the pretreated slag into ZSM-5. It was observed that the synthesis temperature significantly influenced the size of the crystals formed, whereas the synthesis time influenced the shape. The maximum synthesis conditions were found to be 13h and 180°C. The ZSM-5 obtained using the maximum conditions was found to consist of the major characteristic diffraction peaks similar to commercial ZSM-5. However, additional peaks observed were attributed to the presence of augite in small quantities. The synthesized ZSM-5 consisted of well-defined cubic prism shapes with small intergrown rectangular crystals. Furthermore, the morphology of the crystals changed as the synthesis time was varied. The crystalline structure of the synthesized ZSM-5 was found to be mesoporous with moderate relative crystallinity (52.4%). The pore size was relatively high (14.8 nm) with a relatively low BET surface area (108.4 m^2/g). The change in the synthesis conditions (time and temperature) did not affect the chemical composition of the resulting product.

Corn cob residue used was obtained from farm-works and consisted of 75.98 wt.% of volatile matter, making them suitable as a biomass substrate. The synthesized catalyst was evaluated against the commercial catalyst for bio-oil conversion, with performance differences attributed to the presence of trace metal elements. The product distribution was significantly affected by varying the pyrolysis conditions, such as catalyst-to-biomass ratio, pyrolysis time, and pyrolysis temperature. The effect of pyrolysis conditions showed that an increase in pyrolysis temperature positively improved the bio-oil and gas yield. Since ZSM-5 is a bifunctional catalyst, a high catalyst-to-biomass ratio promoted deoxygenation, and a low catalyst-to-biomass ratio resulted in shape selectivity. The pyrolysis time had the least impact on the

product distribution. The maximum pyrolysis conditions were found to be 350°C, 3 min, and catalyst-to-biomass of 1:9. The primary product was bio-oil. However, the gas yield superseded that of the oil. Both catalysts (synthesized and commercial ZSM-5) had a selectivity towards phenols and ketones; however, their compositions varied significantly. The most prominent chemical compounds identified in each group were catechol and cresol for phenol and ethenone and cyclohexanone for ketone. The considerable presence of ketones and phenols in the bio-oil derived in this study exhibits the potential applicability of the synthesized catalyst (ZSM-5) for the production of alternative fuels that mimic fossil fuels subsequent to the removal of oxygenates.

CHAPTER 1

1. INTRODUCTION

1.1. Background and Context

The socio-economic benefits and infrastructural development of a country are largely dependent on its energy generation, transmission, and consumption. These aspects have positioned South Africa (SA) among the largest energy consumers in Africa (Akinbami et al., 2021). South Africa's energy requirements are primarily met by coal, which is the dominant indigenous energy resource. This dominant fossil fuel is reported to be abundant and affordable and supplied 69% of SA's energy needs in 2016. Moreover, SA imports 60% of its crude oil from the Middle East and parts of Africa (Ratshomo & Nembahe, 2019). This persistent usage of fossil fuels in SA and the world at large has led to considerable damage to the environment, climate change issues, and impacts on human health. As such, this has driven researchers and government regulators to adopt environmentally friendly policy instruments and find sustainable solutions that will mitigate the adverse effects caused by fossil fuels (Akinbami et al., 2021).

The most promising alternative to fossil fuels is biofuels, which are energy-valuable materials that are derived from biomass. Biomass is a renewable source that is abundantly available (preferably as waste), low cost, and can be manipulated for energy production. Studies on biomass have revealed its environmental benefits and contribution to sustainable energy supply. Maize is a type of biomass and the largest crop produced in SA (10 million tons per annum), mainly for animal feed. The projected production of maize leaves behind an enormous corn cob (CC) waste [~20% of maize produced annually] (Statistics, 2020). Literature has shown the potential use of corn cob as a biomass substrate for energy production due to its lignocellulosic content (Danje, 2011). In recent years, pyrolysis has been reported as an attractive method to recycle and manage corn cob waste (biomass).

Pyrolysis is a thermochemical conversion technology that converts materials (biomass) in an oxygen-deprived environment into various energy-valuable products, where liquid bio-oil is the main product. The process operates at elevated temperatures to convert the lignocellulosic material found in biomass to produce bio-oil consisting of aromatics, aliphatics, alcohols, and by-products. The by-products are what cause bio-oil to be less desirable for commercial applications and less competitive to petrochemical fuels (Muneer et al., 2019). Organic acids, sugars, and oxygenates make the by-products and structure of the bio-oil have a low calorific value, high viscosity, thermal instability, corrosive nature, incomplete volatility, and reduced combustion efficiency (Hassan et al., 2020). The bio-oil quality can be improved through catalytic pyrolysis. This involves the addition of a catalyst into the pyrolysis process.

Deoxygenation of bio-oil, which leads to high yields of aromatic hydrocarbons, can be achieved during pyrolysis through the use of mesoporous materials or zeolite-based catalysts. Catalytic pyrolysis of various biomass feedstocks (pulp, soap stock, and oil palm fibre) using zeolite-based catalysts has been examined for the production of high-value hydrocarbons (Morgan et al., 2018). Extensive research has been conducted on zeolites (ZSM-5, zeolite Y, and zeolite beta) for the catalytic upgrading of bio-oil. The pore structure of these catalysts, along with their acidic active sites, can control the product distribution and composition of the bio-oil. Wang et al. (2017) investigated the

hierarchical pore architecture of the HZSM-5 catalyst for the aromatization of glycerol. The study reported that dehydration and deoxygenation reactions were present during aromatization, which led to a significant drop in the oxygen content of the liquid product.

Zeolites are microporous materials that are associated with two compounds (SiO_2 and Al_2O_3) which are tetrahedrally linked to each other through their oxygen atoms and create a three-dimensional crystalline structure consisting of pore openings (0.3-1.0 nm) of defined sizes (Khaleque et al., 2020). The porous structure can be controlled by modifying the Si/Al ratio and varying the hydrothermal synthesis operating conditions. Zeolites can be synthesized from low-cost industrial solid wastes such as ashes (fly ash, rice husk ashes, and oil ashes), slags (steel, blast furnace), and clays (Kanda & Harada, 2022). The main requirement for the waste material is the presence of silica (SiO_2) and alumina (Al_2O_3). Metallurgical residues, such as blast furnace slag, are currently being used in cement and road construction due to their high calcium content, including SiO_2 and Al_2O_3. However, only a small amount of slag is being used as a supplemental material for roadbeds and cement. Therefore, there is a need to develop new recycling streams that involve the recovery of value-added minerals from blast furnace slag for secondary application. Numerous studies in literature have shown the potential of using blast furnace slag as an alternative material for the synthesis of zeolites. Kuwahara et al. (2008) used acid leaching followed by hydrothermal treatment to synthesize sodium-based zeolite Y and zeolite X as supporting mediums. Therefore, the current study employed BFS, generated by the iron- and steelmaking industry, as a SiO_2 and Al_2O_3 precursor for the synthesis of zeolite-based materials.

Zeolites are synthesized using the conventional hydrothermal synthesis technique, which entails heating the aluminosilicate-bearing material in an alkaline (NaOH) solution for a defined period of time (hour/days) in an autoclave reactor (Kanda & Harada, 2022). This method has been extensively reported in literature; Serrano et al. (2016) succeeded in synthesizing high crystalline ZSM-5 zeolite composed of micro-and-mesopores. Whereas Sugano et al. (2005) used a newly developed ball mill reaction vessel containing SiC balls to accelerate the hydrothermal reaction. The synthesized zeolite A was stable at a temperature of 600°C. Chaihad et al. (2021) removed silica from commercial HZSM-5 zeolite using hydrothermal treatment. The mesopores of the desilicated zeolite were controlled to maintain enough acid-active sites, which resulted in an increase in surface area. The aforementioned studies have proved the benefits of using hydrothermal synthesis to manipulate the structural features of zeolites. However, prolonged periods (> 48 h) are required to achieve zeolite synthesis. Alternatively, microwave irradiation can be used to significantly reduce synthesis periods.

The proposed zeolite-based materials were synthesized from blast furnace slag. The synthesized materials were applied in the pyrolysis of corn cob to evaluate their catalytic performance. The hydrothermal synthesis method was conducted using a microwave-heated unit. This is due to the fact that microwave irradiation increases the rate of dissolution of the slag waste and increases the crystallization kinetics (Zeng et al., 2021). This was done by accelerating the dissolution of the minerals, resulting in increased concentration of nuclei. Furthermore, microwave irradiation improves the uniformity and composition of the synthesized zeolite during crystallization (Gin et al., 2021). That is, the reactants (concentration of nuclei) are rapidly consumed during crystallization to form homogeneous particle sizes. This type of heating source is reported to be effective compared to conventional heating. A comparative study (conventional vs. microwave hydrothermal synthesis) was

conducted by Anuwattana et al. (2008) to synthesize a ZSM-5 catalyst from cupola slag. It was reported that microwave irradiation improved the dissolution of silica from the slag and increased the formation of zeolite crystals by 6 times. The current study reconstructed the porous structure of zeolite, from blast furnace slag, by controlling the synthesis conditions so as to synthesize zeolite-based materials with varying structural, physical, and chemical properties.

1.2. Problem Statement

Pyrolysis is a robust technology that has significantly contributed to the development of a circular economy and has been extensively investigated and used in the conversion of biomass. The main drawback of this process is the quality of the bio-oil produced. The number of oxygenated compounds in pyrolytic bio-oils negatively impacts the physicochemical properties of fuels, hence hindering their exploitation as transportation and industrial fuels. That is, bio-oil's suitability as a direct fuel substitute for transportation is severely limited due to inherent characteristics such as its low chemical stability, elevated oxygen and moisture levels, restricted storage duration, low caloric value, acidity, and distinctly high polarity, all of which render it immiscible with traditional fuels. Zeolite catalysts are naturally microporous inorganic materials, and their catalytic activity and shape selectivity are attributed to their uniform pore sizes and long channels. These features allow ZSM-5 to selectively adsorb and catalytically transform compounds with specific shapes and sizes. However, the presence of narrow micropores (0.5 nm - 0.6 nm) poses a limitation. That is, bulky organic molecules are unable to diffuse into the channels and access the active acidic sites, resulting in the formation of coke, reduced catalytic activity, and, ultimately, catalyst deactivation. The major components (Al_2O_3 and SiO_2) in blast furnace slag make it a suitable industrial waste resource for zeolite synthesis. However, the presence of CaO and MgO affects the synthesis process by inhibiting zeolite crystallization.

1.3. Research Rationale

South Africa is highly dependent on its oil imports to sustain its liquid fuel consumption levels. The major petroleum products currently consumed in SA include diesel and petrol, to which, their retail price is heavily fluctuating and regulated by the government (Akinbami et al., 2021). With the added surge in fuel prices, biofuels are becoming a sought-after solution, not only to combat the disparity of domestic fuel prices but also to mitigate the damages caused by fossil fuels. Thus, biomass, as a renewable source, has attracted much attention due to its net-zero emissions, sustainable energy supply, and abundance. The current study investigated the performance of zeolite-based catalysts for the pyrolysis of corn cob (biomass). The benefit of pyrolyzing biomass waste is to reduce its environmental impact and provide alternative waste recycling options.

The performance of a catalyst is largely influenced by its properties, whereas its procurement process significantly contributes to the operating costs of the process. A comprehensive literature survey led to the identification of a knowledge gap, that is, the secondary application of solid waste from the iron- and steelmaking process for the synthesis of zeolite-based catalysts. Hence, the catalyst used in this study was synthesized from solid waste (slag) generated by an iron and steel production plant. This is encouraged by the chemical and mineral composition of solid waste which contains the presence of value-added elements that can be of interest for secondary use (Azizi et al., 2021). A microwave-assisted hydrothermal synthesis method was applied to synthesize the zeolite-based catalysts from blast furnace slag. This method promises to provide diverse benefits such as slag waste management

and room to manipulate the physicochemical properties of the synthesized catalysts to fit process requirements.

1.4.Research Objectives

1.4.1. Aim

The socio-economic and environmental benefits that have been generated by the conversion of waste (biomass) into value-added products (bio-oil) are essential for technological advancement, urbanization, and human growth. Thus, the aim of this study was to synthesize zeolite-based catalysts from blast furnace slag. The microwave-assisted hydrothermal method was used to synthesize the zeolite-based catalysts.

1.4.2. Objectives

The objectives of the work were:

a) To establish the potential of acid leaching of blast furnace slag, in reducing the calcium and magnesium contents in the slag, thus improving the microwave-assisted hydrothermal synthesis method.
b) To synthesize the zeolite-based catalysts from the pretreated slag and characterize both the treated slag and synthesized catalysts so as to determine their respective physical and chemical properties.
c) To evaluate the catalytic performance and selectivity of the synthesized zeolite-based catalysts by employing pyrolysis of corn cob.

1.5. Structure of Thesis

The dissertation consists of 6 chapters, primarily focused on presenting the work through a series of articles. It is important to note that the articles, namely **CHAPTER 3, CHAPTER 4**, and **CHAPTER 5**, were developed based on the specific objectives and are presented in chronological order. Therefore, the findings and results from each article serve as a basis for the subsequent article. Each article is self-contained and can be read independently of the others.

CHAPTER 2 (Literature review) details various aspects of lignocellulosic biomass and its thermochemical conversion into valuable products such as biofuels. The chapter specifically examines the structure and composition of lignocellulosic biomass, the pyrolysis process utilizing zeolite-based catalysts, and the advancements in zeolite synthesis techniques. Moreover, the chapter dives into the influence of zeolite properties, such as structure, size, and shape, on catalytic performance, particularly in terms of active acid sites present in zeolites. The text highlights the significance of these factors in enhancing the catalytic efficiency of zeolites for hydrocarbon cracking and biofuel production. Furthermore, various industrial waste resources are surveyed, exploring the different processes that generate them and detailing their chemical compositions.

CHAPTER 3 focuses on the acid leaching of blast furnace slag (BFS) to improve zeolite synthesis. The study includes the characterization of the raw and pretreated slags, along with their synthesized products. The chapter also explores the impact of various leaching conditions. In **CHAPTER 4**, the study delves into the microwave-assisted synthesis of ZSM-5 zeolite using blast furnace slag as a precursor. Here, synthesis conditions such as crystallization time and temperature were varied to

explore their effects on the physicochemical and structural properties of the synthesized ZSM-5. **CHAPTER 5** focuses on the use of a slag-derived HZSM-5 zeolite catalyst in the microwave-assisted pyrolysis of corn cob. The chapter explores the effect of different pyrolysis conditions on product distribution and bio-oil composition. **CHAPTER 6** concludes with a summary of the overall findings from the three articles and detailed recommendations for future research.

References

Akinbami, O. M., Oke, S. R., & Bodunrin, M. O. (2021). The state of renewable energy development in South Africa: An overview. *Alexandria Engineering Journal*, *60*(6), 5077–5093. https://doi.org/10.1016/j.aej.2021.03.065

Anuwattana, R., Balkus, K. J., Asavapisit, S., & Khummongkol, P. (2008). Conventional and microwave hydrothermal synthesis of zeolite ZSM-5 from the cupola slag. *Microporous and Mesoporous Materials*, *111*, 260–266. https://doi.org/10.1016/j.micromeso.2007.07.039

Azizi, D., Ibsaine, F., Dionne, J., Pasquier, L. C., Coudert, L., & Blais, J. F. (2021). Microporous and macroporous materials state-of-the-art of the technologies in zeolitization of aluminosilicate bearing residues from mining and metallurgical industries: A comprehensive review. *Microporous and Mesoporous Materials*, *318*. https://doi.org/10.1016/j.micromeso.2021.111029

Chaihad, N., Situmorang, Y. A., Anniwaer, A., Kurnia, I., Karnjanakom, S., Kasai, Y., Abudula, A., Reubroycharoen, P., & Guan, G. (2021). Preparation of various hierarchical HZSM-5 based catalysts for in-situ fast upgrading of bio-oil. *Renewable Energy*, *169*, 283–292. https://doi.org/10.1016/j.renene.2021.01.013

Danje, S. (2011). Fast pyrolysis of corn residues for energy production. In *MSc Eng*. Stellenbosch University.

Gin, A. W., Hassan, H., Ahmad, M. A., Hameed, B. H., & Mohd Din, A. T. (2021). Recent progress on catalytic co-pyrolysis of plastic waste and lignocellulosic biomass to liquid fuel: The influence of technical and reaction kinetic parameters. *Arabian Journal of Chemistry*, *14*(4), 103035. https://doi.org/10.1016/j.arabjc.2021.103035

Hassan, H., Hameed, B. H., & Lim, J. K. (2020). Co-pyrolysis of sugarcane bagasse and waste high-density polyethylene: Synergistic effect and product distributions. *Energy*, *191*, 116545. https://doi.org/10.1016/j.energy.2019.116545

Kanda, Y., & Harada, S. (2022). Synthesis of zeolites from calcareous waste concrete powder. *Results in Materials*, *13*, 100250. https://doi.org/10.1016/j.rinma.2021.100250

Kuwahara, Y., Ohmichi, T., Mori, K., Katayama, I., & Yamashita, H. (2008). Synthesis of zeolite from steel slag and its application as a support of nano-sized TiO2 photocatalyst. *Journal of Materials Science*, *43*(7), 2407–2410. https://doi.org/10.1007/s10853-007-2073-0

Morgan, H. M., Bu, Q., Liang, J., Liu, Y., Mao, H., Shi, A., Lei, H., & Ruan, R. (2017). A review of catalytic microwave pyrolysis of lignocellulosic biomass for value-added fuel and chemicals. *Bioresource Technology*, *230*, 112–121. https://doi.org/10.1016/j.biortech.2017.01.059

Muneer, B., Zeeshan, M., Qaisar, S., Razzaq, M., & Iftikhar, H. (2019). Influence of in-situ and ex-situ HZSM-5 catalyst on co-pyrolysis of corn stalk and polystyrene with a focus on liquid yield and quality. *Journal of Cleaner Production*, *237*, 117762. https://doi.org/10.1016/j.jclepro.2019.117762

Ratshomo, K., & Nembahe, R. (2019). The South African Energy Sector Report 2019. In *Department of Energy*.

Serrano, D. P., Escola, J. M., Sanz, R., Garcia, R. A., Peral, A., Moreno, I., & Linares, M. (2016). Hierarchical ZSM-5 zeolite with uniform mesopores and improved catalytic properties. *New Journal of Chemistry*, *40*(5), 4206–4216. https://doi.org/10.1039/c5nj02856f

Sugano, Y., Sahara, R., Murakami, T., Narushima, T., Iguchi, Y., & Ouchi, C. (2005). Hydrothermal synthesis of zeolite a using blast furnace slag. *ISIJ International*, *45*(6), 937–945. https://doi.org/10.2355/isijinternational.45.937

Wang, F., Zhou, M. xi, Yang, X. hui, Gao, L. jing, & Xiao, G. min. (2017). The effect of hierarchical pore architecture on one-step catalytic aromatization of glycerol: Reaction routes and catalytic performances. *Molecular Catalysis*, *432*, 144–154. https://doi.org/10.1016/j.mcat.2017.01.017

Zeng, X., Hu, X., Song, H., Xia, G., Shen, Z. Y., Yu, R., & Moskovits, M. (2021). Microwave synthesis of zeolites and their related applications. *Microporous and Mesoporous Materials*, *323*, 111262. https://doi.org/10.1016/j.micromeso.2021.111262

CHAPTER 2

2. FROM WASTE TO CATALYST: ZEOLITE SYNTHESIS AND APPLICATION IN LIGNOCELLULOSIC BIOMASS PYROLYSIS

Review paper under review.

2.1. Introduction

Energy stands as a paramount resource for humanity, serving as a vital link between the natural world and human existence. The growing energy needs are a pressing concern as there are currently no viable alternatives to support a nation's social and economic growth. This issue demands immediate attention and comprehensive analysis. The conversion of biomass to biofuels has shown great potential to supplement growing energy needs. Primary biomass substrates that have received attention as renewable resources include forestry residues, animal waste, municipal trash, agricultural residues, and algae (Van Meerbeek et al., 2015). The conversion of biomass into bioenergy entails utilizing various thermochemical processes (such as pyrolysis, combustion, liquefaction, gasification, and combustion) that operate at elevated temperatures. Among these methods, pyrolysis is particularly advantageous due to its diverse range of products, including biochar, bio-oil, and syngas (Panwar et al., 2012). Introducing a catalyst during the biomass pyrolysis process emerges as a highly promising and effective approach for enhancing the physicochemical properties of the resulting products. Catalysts commonly employed in catalytic pyrolysis encompass activated carbon, metal oxides, dolomite, clay, and zeolites. Zeolites serve as prevalent industrial catalysts, facilitating reactions such as alkylation, isomerization, cracking and oligomerization (Tung et al., 2012).

Zeolites are traditionally classified under a family of open-framework materials consisting of pore spacings that are molecular in dimension and uniformly distributed. The framework in zeolites is established from a three-dimensional crystalline tetrahedral (TO_4); whose T can be represented by a metal ion (Al, Si, or P). This diversity in substituting different metal ions results in a variety of frameworks that can be achieved with varying compositions (Li et al., 2017). This was shown by Wang et al. (2023), where they synthesized a zeolite framework consisting of [SiO_4] and [TiO_4] units that were assembled in a MFI structure. The synthesized titanosilicate zeolite was reported to exhibit acceptable hydrothermal stability and was used for shape-selective catalytic oxidation reactions. The International Zeolite Association – Structure Commission (IZA-SC) has, to date, successfully approved more than 260 distinct zeolites identified as naturally occurring or synthesized inorganic substances, which are distinguished through their frameworks (three-letter code). Natural zeolites have limited applications due to their fixed channels and pore openings. Furthermore, they are formed with impurities (SO_4^{2-} and Fe^{2+}) and consist of amorphous phase (Yoldi et al., 2019). Therefore, synthetic zeolites are considered more effective than naturally occurring zeolites due to the allowance to manipulate the composition and pore structure of the framework to suit a particular application. However, synthetic zeolites are relatively expensive due to their production costs (Bouanga Boudiombo et al., 2023).

The framework of synthetic zeolites consists of membered rings that are connected to form channels consisting of molecular-sized pore openings. The pore openings are categorized into small pores (≤ 8-ring), medium pores (10-ring), large pores (12-ring), and extra-large pores (>12-ring) (Li et al., 2017). The leeway to control the shape and size of the pore opening gives synthetic zeolites the ability to be applied in a variety of industries. The commonly synthesized zeolites are type X, ZSM-5, type Y, type LTA, and USY, and these zeolites have a combined global market valued at USD 5.9 billion in 2023 (MarketsandMarkets, 2018) and is projected to reach USD 9.28 billion by 2032 (Fortune Business Insights, 2025). Due to their unique physicochemical properties, synthetic zeolites are traditionally found in applications such as a heterogeneous catalyst in petrochemical and oil-refining (Alkhlel & De Lasa, 2018), soil conditioners in agricultural activities (Nakhli et al., 2017) and adsorbent in wastewater treatment (Wen et al., 2018). Moreover, the application of synthetic zeolites has widened to include sustainable processes such as environmental remediation (Jendrlin et al., 2023) and green chemistry (Li et al., 2017). The conventional route to synthesize zeolites is using an aluminosilicate gel, which opened researchers to explore various synthesis methods and aluminium and silicone sources. The route involves mixing pure chemicals of Si and Al to form a supersaturated aluminosilicate gel, which is then heated to moderate temperatures in a pressurized vessel for several hours or days to induce nucleation and crystallization. This conventional route has led to the development of a range of synthesis techniques such as hydrothermal synthesis (Johnson & Arshad, 2014), sol-gel synthesis (Wang et al., 2018), alkali fusion (Belviso et al., 2017) and ultra-sound energy (Pal et al., 2013). However, the commercial production of zeolites from pure chemicals can be costly and environmentally damaging. Therefore, the use of industrial waste as a raw material for synthesizing zeolites has gained attention as a sustainable alternative that provides a solution for waste management while reducing the environmental impact of zeolite production (Yoldi et al., 2019).

Industrial waste is generated from various industries such as steel, coal, agriculture, mining, and chemicals. The by-products from these industries are often discarded in landfills, stagnant waters, or inadequately used for secondary purposes. This negatively impacts the environment, aquatic life, and freshwater bodies. To maintain sustainability in the manufacturing and allied processes, waste generated from these processes must be recycled. Delightfully, most of these wastes contain significant amounts of silicon and aluminium, thus making them potential candidates for use as low-cost raw materials to produce porous materials such as zeolites. Sayehi et al. (2022a) conducted work on valorizing aluminium scraps and waste glass (fluorescent tubes) for the synthesis of zeolite Na-LTA. It was concluded that the secondary utilization of aluminium scraps and waste glass was enhanced through the hydrothermal treatment to produce zeolite Na-LTA. Similar work was done by (Maatoug et al., 2018), where they valorized vitreous China waste to produce zeolites containing various frameworks (SOD, Na-P, FAU, EMT, and NA-X). Vitreous China is derived from heating powered glass and applied as an enamel coating. The conversion of the waste was a success, and it was reported that SiO_2 from an amorphous waste can be easily solubilized compared to waste with a crystalline phase (mullite or quartz). Although the conversion of various wastes has been well-researched, synthesizing zeolites from industrial waste presents unique challenges compared to synthesizing zeolites from conventional raw materials. One of the major challenges is the presence of impurities in the waste material, which can affect the purity and quality of the zeolite product. The waste can be beneficiated through various pre-treatment methods, such as acid leaching (Sugano et al., 2005), alkaline fusion (Ameh et al., 2020), or alkaline leaching (Cornelius, 2019). These beneficiation

processes are suited to solubilize the Si and Al or enrich the composition of Si and Al in the solid waste by removing the impurities. However, these processes can increase the cost of zeolite production and energy consumption. Another challenge is the variability in the composition and properties of the waste material, which can result in inconsistent zeolite product quality. Moreover, the synthesis conditions and the type of zeolite synthesized from waste materials may differ from those used for conventional raw materials, making the process more complex (Tauanov et al., 2018).

2.2. Lignocellulosic Biomass

Natural resources (land, air, and water) are constantly under threat due to numerous human activities which largely generate waste materials. These unwanted materials are usually solid in form and inherently organic (biomass). A distinct feature of biomass waste is its secondary application of being converted into a resource for energy generation or industrial production (Fatih Demirbas et al., 2011). Biomass refers to organic matter from plants and animals that can be used to produce various chemicals, heat, biofuels, or electricity. Biomass residues, deemed unsuitable for animal or human consumption, have emerged as a sustainable energy alternative, offering substantial environmental advantages, and demonstrating remarkable potential to mitigate greenhouse gas emissions (Reza et al., 2023). Biomass energy stands out as the most substantial renewable energy source in South Africa, primarily used in the form of wood fuel for cooking and heating purposes in remote locations. However, in 2010, a mere 10% of the nation's energy consumption was attributed to biomass energy, compared to the 67% provided by indigenous coal (Petrie & Macqueen, 2013). The use of biomass for energy generation presents several significant advantages. Firstly, the cost of biomass residues is relatively low, making it a cost-effective option compared to other methods reliant on fossil fuels. Additionally, the energy conversion efficiency of biomass is notably high, further contributing to its appeal. This higher efficiency leads to a reduction in the overall cost of energy generation. Furthermore, biomass technology also yields organic fertilizer, which enhances crop production and promotes a clean and environmentally friendly ecosystem. Biomass waste materials are readily accessible as municipal solid waste (MSW), agricultural crop residues, animal waste, wood and forest residues, and algae (***Figure 2.1***). It is worth noting that agricultural waste (corn cob) was used as a biomass substrate in the current study. Most biomass materials usually consist of a lignocellulosic content that comprises lignin (15–30%), hemicellulose (20–40%), and cellulose (40–60%). These lignocellulosic contents form a complex biomass structure due to their bonding arrangement (van der Waals' forces, intermolecular bridges, and covalent bonds). As such, biomass materials are insoluble in water and resistant to enzymatic hydrolysis (Ayeni & Daramola, 2017).

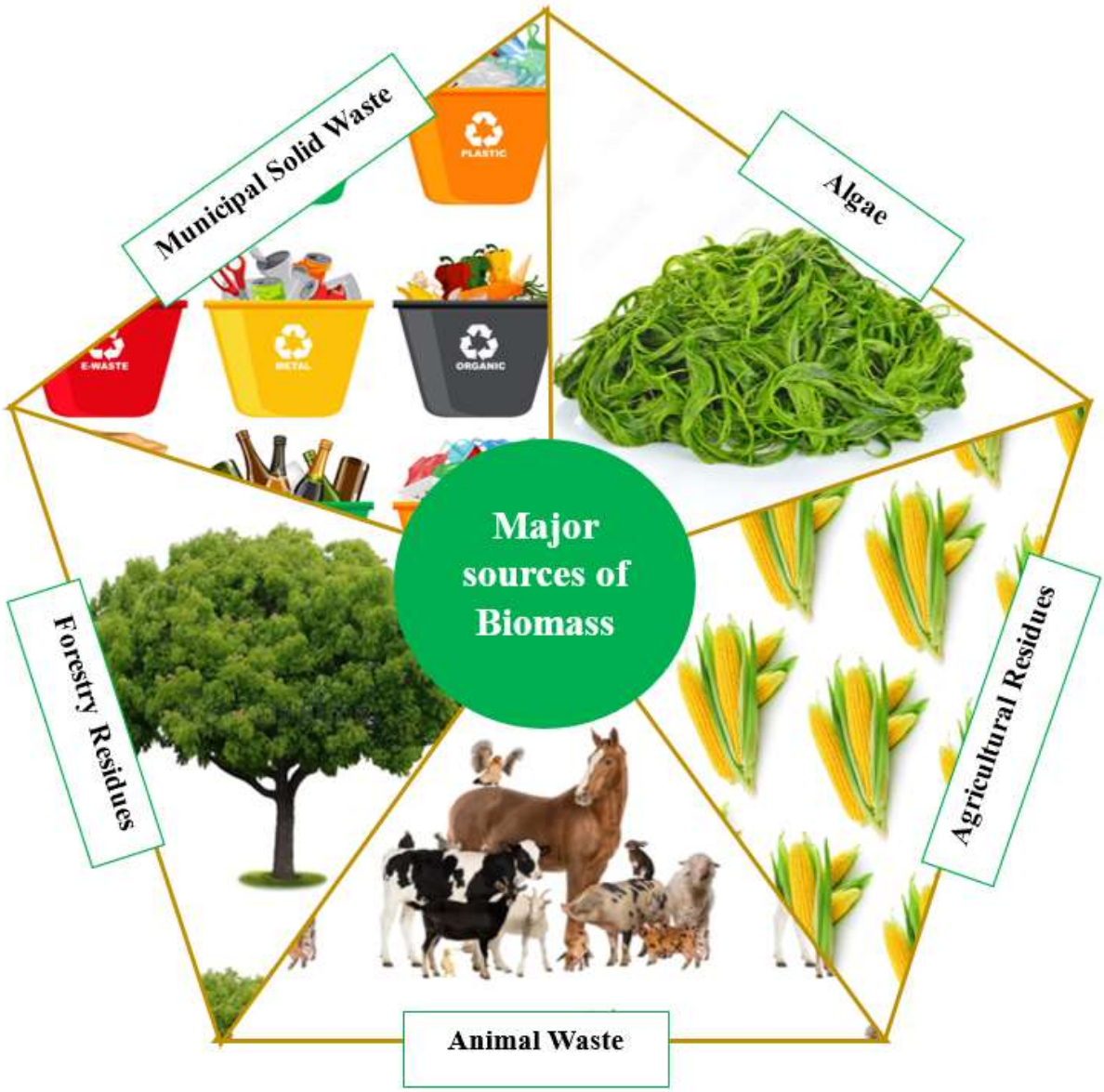

Figure 2.1. Key sources of biomass.

The pyrolysis product distribution (gas, solid, and liquid) obtained from recycling lignocellulosic biomass is highly dependent on the interaction between the lignocellulosic components (amongst other factors). That is, in considering the hierarchical structure of biomass, lignin is an aromatic polymer synthesized from phenylpropanoid precursors found on the structure's outer cell wall. Whereas cellulose is a glucose polymer whose structure is present with the lignin shell and consists of polymer chains tightly packed into crystalline structures that resist depolymerization and are water-insoluble (Kumar et al., 2020). Conversely, hemicellulose consists of pentose sugar chains that bind the cellulose fiber and micelles. Hence, it is located within the cellulose shell but can also be present between the lignin and cellulose shells (Fatih Demirbas et al., 2011). Usino et al. (2021) investigated the reaction interactions between the lignocellulosic contents and product distribution during fast pyrolysis. The biomass sample used was birchwood. The results from the study showed that lignin is responsible for producing phenolic compounds; however, this phenomenon is significantly reduced (62%) when

cellulose is present. Comparably, Wu et al. (2016) studied the interactions between lignin and cellulose on the distribution of light products. Milled wood was used as a lignin precursor, and cellulose was procured as a commercial product. The study reported that the morphology and covalent bonds between cellulose and lignin contributed significantly to the interaction mechanism. Furthermore, low molecular weight products (ketones, aldehydes, phenols, and syringols) were promoted due to the presence of both components. Literature has shown the importance of lignocellulosic contents and that their interactions play a significant role in the thermochemical conversion of biomass.

2.2.1. Lignin

Lignin is a complex aromatic heteropolymer that forms cross-connected units of phenylpropane bonded together through hydroxyl and methoxy functional groups. It provides structural support and binds hemicellulose and cellulose together, and enhances resistance against the activities of bacteria, spores, and enzymes, as it is located in the outer layer of the cell wall matrix (Wendisch et al., 2018). In comparison to cellulose and hemicellulose, lignin possesses a low oxygen content and high carbon content and is resistant to degradation, which creates a challenge for biomass conversion. This is due to its primary structural units (syringyl, hydroxyphenyl, and guaiacyl), which hinder access to cellulose and hemicellulose and prevent enzymatic hydrolysis (Rahimi et al., 2014). The reaction pathway of lignin during pyrolysis involves the intricate formation of various intermediates and products through complex reaction mechanisms (***Figure 2.2***). Initially, lignin undergoes depolymerization, and it is broken down into smaller aromatic compounds by breaking the long chains of phenolic units. This is done by cleaving the syringyl, hydroxyphenyl, and guaiacyl linkages. At higher temperatures (450–525°C), a series of reactions, including decarboxylation, demethylation, decarbonylation, and demethoxylation, produce light gases (CO, CO_2, CH_4), phenolic compounds (catechol and guaiacol), and char (Lu & Gu, 2022). These insightful findings shed light on the intricate pathways and transformations that lignin undergoes during the process of pyrolysis.

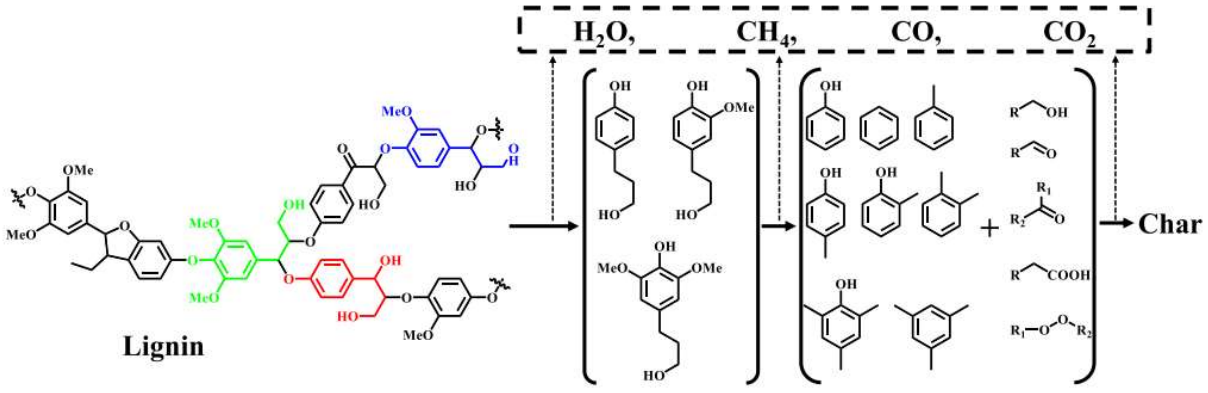

Figure 2.2. Composition and pyrolysis reaction pathway of lignin [adapted from: Lu & Gu (2022)].

2.2.2. Cellulose

Cellulose, the primary component of biomass cell walls, is an extremely abundant organic polymer in nature $(C_6H_{10}O_5)_n$ and exists in both crystalline and amorphous forms. It is composed of linear polymer glucose molecules, which are connected through β-1,4 glycosidic bonds, hydrogen bonds, and Van der Waals forces and surrounded by lignin, hemicellulose, heterogeneous polysaccharide (Jiang et al.,

2022). Due to its strong insolubility in water and resistance to depolymerization, cellulose plays a crucial role in maintaining the structural integrity of biomass. When comparing crystalline and amorphous cellulose, the former exhibits a higher resistance to degradation. This characteristic makes it a desirable component for biomass with a higher cellulose content, as it can produce significant amounts of bio-oil, starting depolymerization at ~350°C (Lu & Gu, 2022). The reaction mechanism of cellulose during pyrolysis involves cracking and dehydration of water molecules being released from the glucose units and the further conversion into cellulosic species (monosaccharides, levoglucone, and levoglucosan) [***Figure 2.3***]. At elevated temperatures, primary volatile compounds formed are anhydrosugars which undergo secondary reactions such as condensation, cyclization, and fragmentation to form light oxygenates (acids, furans, ketones, and aldehydes). Parallel secondary reactions such as graphitization, aromatization, and cross-linking result in a carbonaceous residue (char). Subsequent conversion of char, that is, decarboxylation and decarbonylation, forms light gaseous products (Lin et al., 2009).

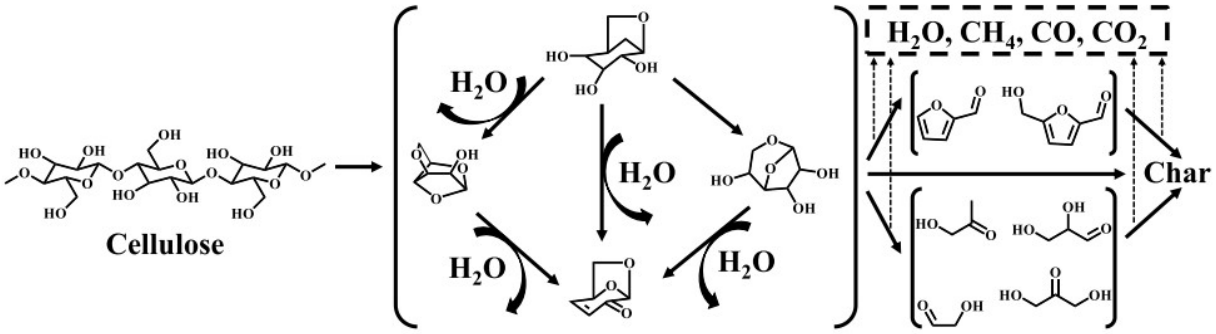

Figure 2.3. Composition and pyrolysis reaction pathway of cellulose [adapted from: Lu & Gu (2022)].

2.2.3. Hemicellulose

Hemicellulose, a crucial cell wall component, is an amorphous and heterogeneous branch of polysaccharide $(C_5H_8O_4)_n$. It possesses a lower molecular weight compared to cellulose and lacks the same level of strength. Comprised of various sugar units such as glucomannans, xylan, lactose, and fucose, hemicellulose forms a branched glucose or xylose polymer (Lu & Gu, 2022). Its degree of polymerization renders it amorphous, easily hydrolyzable, and a cementing material between cellulose fibers in the plant cell wall. Due to its shorter polymer chains and lower molecular weight, hemicellulose plays a significant role in supporting the pyrolysis process, generating volatile and gaseous materials (Reza et al., 2023). The reaction mechanism of hemicellulose during pyrolysis is shown in ***Figure 2.4***. In fact, it is one of the most effective elements in the catalytic pyrolysis process, enabling the production of larger quantities of aromatic hydrocarbons. Due to the complex structure of hemicellulose, xylan has been widely used as a representative polymer in the investigation of the hemicellulose pyrolysis mechanism (Wang et al., 2017). The early phase of hemicellulose pyrolysis involves the dehydration of hydroxyl groups, the opening of xylopyranose rings, and the cleavage of glycosidic bonds between the sugar units. Further decomposition of the model polymer involves reactions such as retro Diels–Alder, retro-aldol, and dehydration to facilitate the formation of aldehydes and CO (Lupi et al., 2023). Depolymerization of hemicellulose polymer chains produces primary volatile products (light gases) which undergo secondary reactions (condensation, cyclization,

and cracking) to yield lightweight oxygenates (ketones, aldehydes, furans, etc.) [Dai et al., 2021]. Char formation in hemicellulose is similar to that of cellulose. During the pyrolysis process, most olefins, which are important precursors for bio-oil, are derived from biomass with higher cellulose or hemicellulose content rather than from feedstock with higher lignin content. This highlights the significance of cellulose in the production of biofuels.

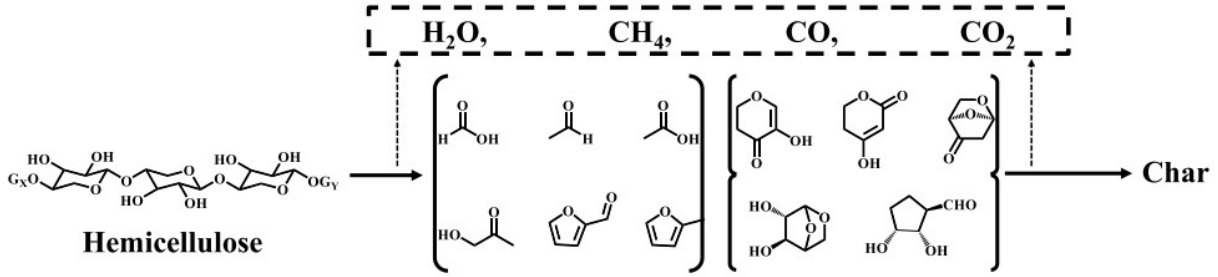

Figure 2.4. Composition and pyrolysis reaction pathway of hemicellulose [adapted from: Lu & Gu (2022)].

2.2.4. Major Sources of Biomass

Biomass is a versatile energy source that can be converted into liquid, gaseous, and solid fuels, suitable for various applications such as transport, heating, and power generation. Adequate usage of biomass as an energy resource increases its contribution to renewable energy sources. Biofuels are derived from their biological feedstocks, which are classified into four distinct categories: first, second, third, and fourth generation (Saladini et al., 2016):

1. First-generation biofuels: these are derived from food crops sown in arable land, such as sugarcane and maize. The crops are fermented to create bioethanol, an alcoholic fuel that can be blended with gasoline or can be used in fuel cells to produce power. Biodiesel, which is a first-generation biofuel, is derived from oils in crops, including rapeseed or beets, and is used in significant amounts in Europe.
2. Second-generation biofuels: also known as advanced biofuels, these are derived from non-food biomass sources, including perennial energy crops and crop residues or wastes. The feedstock for fuel production grows in arable land but is a byproduct of the main crop, or it is planted in marginal land. Industry, agriculture, forestry, and domestic wastes may also be used for second-generation biofuels through the processes of anaerobic digestion to produce biogas, gasification to produce syngas, or direct combustion. Cellulosic biomass, derived from non-food crops, including trees and grasses, is in the process of being developed as a feedstock to produce ethanol. Biodiesel can also be produced using leftover food products, including vegetable oils and animal fats.
3. Third-generation biofuels: these biofuels consist primarily of algae and cyanobacteria, which are organisms with high lipid content that grow very quickly. Algae can be cultivated in non-arable land and can be fed with wastewater, thus reducing the competition with water for food crops. The high oil content in algae makes it a promising feedstock for the production of biodiesel. However, issues such as the high cost of cultivation and processing have been limiting mass production.

4. Fourth-generation biofuels: Includes genetically engineered plants and microorganisms designed for enhanced biofuel production and carbon capture. These advanced technologies aim to maximize efficiency and minimize environmental impact. This group comprises the advanced biofuels produced by emerging technologies, including electrofuels, photobiological fuels (photosynthetic micro-organisms), and genetically modified organisms (bio-engineered cyanobacteria). Fourth-generation biofuels will work towards carbon neutrality by integrating carbon capture and storage (CCS) technologies in the production process, which will decrease the amount of CO_2 in the atmosphere. Although the technologies are at different stages of research and development, they have the promise of sustainable and effective biofuel production in the future.

This progression from first to fourth-generation biofuels reflects the industry's efforts to enhance sustainability, reduce competition with food resources, and improve the environmental footprint of biofuel production.

2.3. Thermochemical Conversion of Biomass

Biomass has the ability to be directly converted into high-value products (biofuel and bioenergy) in any form (liquid, gas, and solid) using thermochemical technology (Patel et al., 2016). This, in turn, indicates that thermochemical technologies rely on lignocellulosic feedstocks to form products that are competitive to conventional chemicals and fuels. In contrast, biochemical technologies rely on blending enzymes or microorganisms with biomass for energy production (Shahbaz et al., 2021). The benefits of using these technologies include a variety of fuel products, reduced catalyst costs, comprehensive feedstock usage, and low reaction time (Shahbaz et al., 2021). Biomass can be converted using one of several technologies: combustion, gasification, pyrolysis, liquefaction, and carbonization.

In combustion, the conversion of biomass occurs in the presence of air to produce heat and power. This is the simplest thermochemical conversion process and is a major source of thermal energy in industrial processes. Gasification, which is an extension of pyrolysis, thermally decomposes biomass at elevated temperatures [> 500°C] (Arpia et al., 2021). This process is optimized to enhance gaseous products (syngas) and is conducted in the presence of gaseous agents (oxygen, air, and steam). Pyrolysis is considered the starting point of all thermochemical conversion processes due to the occurrence of all thermochemical reaction mechanisms to form the main products (biochar, bio-oil, and gaseous fuels) (Patel et al., 2016). The pyrolytic decomposition of biomass occurs in an inert atmosphere, and manipulation of the process conditions changes the pyrolytic behavior of the process. Liquefaction converts biomass by hydrothermally decomposing it into liquid fuel fragments. In contrast to other thermochemical technologies, liquefaction does not require biomass to be dried. Analogous to gasification, carbonization is also an extension of pyrolysis, in that, the solid product is enhanced to produce a carbon-rich solid residue (Demirbaş, 2001). In this study, pyrolytic conversion of corn cob will be considered.

A hydrothermal liquefaction of lignin-bearing biomass study was conducted by Zhang et al. (2009). A liquid yield of 82.1% was achieved, and this was attributed to the appropriate selection of operating conditions (heating rate, liquefaction time, and liquefaction temperature). Strezov et al. (2007) subjected three biomass samples (bagasse, wood sawdust, and macadamia nutshell) to carbonization

in order to quantify the mass and energy characteristics. A three-stage decomposition mechanism was reported, that is, 1) an endothermic removal of moisture content and hydrated compounds during the early stages, 2) an exothermic decomposition (> 230°C) which produced hydrocarbons, bio-oil, and oxides of carbon, 3) and evolution of hydrogen commenced at temperatures above 600°C.

2.4. Pyrolysis Using Zeolite-based Catalysts

The complex chemical composition of biomass is the main reason for upgrading the properties of bio-oil. Furthermore, the selectivity towards the desired compounds in the bio-oil is often a challenge. This is caused by various biomass materials having varying compositions, which result in different distributions of compounds in the bio-oil. This has prompted the application of catalysts in pyrolysis to increase product selectivity, optimize product distribution, and reduce the optimum temperature required for pyrolysis (Anuar Sharuddin et al., 2016). The latter is rather critical since pyrolysis requires high temperature (highly endothermic), which limits its commercial application.

The catalysts used in pyrolysis are homogenous, that is, they have the same phase (solid) as the feedstock. Zeolites are the most commonly used catalysts in pyrolysis due to their abundance, easily accessible, and proven catalytic behaviour to convert biomass into hydrocarbons (Ahmed et al., 2020). The frequently used zeolite-based catalysts, which are based on their framework, are A, P, X, W, Y, ZSM-5, mordenite, and silicate. The basic feature of zeolite-based catalysts is their three-dimensional structure, which is composed of tetrahedral networks of $[SiO_4]^{4-}$ and $[AlO_4]^{5-}$ that are linked together through their oxygen atoms. The molecular formula for zeolites is generally expressed as $M_{a/b}[(AlO_2)_a(SiO_2)_y].cH_2O$, where (M) represents an alkaline earth metal or alkaline metal, (b) represents the valence of that cation, (c) is the number of molecules contained in intracrystalline channels per unit cell, (a) and (y) are the number of $[AlO_4]^{5-}$ and $[SiO_4]^{4-}$ tetrahedral cells per structural unit, respectively (Vigil de la Villa Mencía et al., 2020a). Zeolites fall under the aluminosilicate family composed of a microporous crystalline structure (Khaleque et al., 2020). The microporous structure of zeolites has reduced its effectiveness for deoxygenation of bio-oil. This is due to the diffusion limitation and steric hindrance of large hydrocarbon molecules when approaching the active acid sites of the catalyst (Nugraha et al., 2021). This has led to the development of advanced zeolites containing multilevel porosities (micropore, mesopore, and macropore). These zeolites are referred to as hierarchical zeolites and are synthesized through conventional desilication and dealumination methods. However, in the current study, the crystalline structure of an aluminosilicate percussor (blast furnace slag) will be experimentally controlled to form zeolites with various pore structures and sizes.

Liu et al. (2017) performed a newly developed two-step catalytic fast microwave-assisted pyrolysis study on a biomass sample (corn stover) using an HZSM-5 catalyst. The effects of pyrolysis temperature (450–650°C) at fixed catalyst loading and catalyst bed temperature were investigated. It was concluded that the catalyst bed temperature had a significant effect on the product's chemical profiles. Therefore, separating the catalyst bed from the feedstock will simplify the catalyst recovery and regeneration processes. Chaihad et al. (2021) studied the synthesis of a hierarchical HZSM-5 catalyst for the fast upgrading of bio-oil. The hierarchical HZSM-5 catalyst was synthesized from commercial HZSM-5 using the desilication method with the addition of NaOH solution and tetrapropylammonium hydroxide (TPAOH). It was concluded that a specific concentration of NaOH (0.2M) and TPAOH (0.25M) during desilication exhibited maximum catalytic performance. Over the past years, the research of hierarchical zeolite catalysts has gained massive interest. Scientists have

been working extremely hard to prepare hierarchical zeolites by developing new methods and using various synthetic methods to synthesize catalysts. This has led to an increase in yearly research publications (Feliczak-Guzik, 2018a). Two well-known major techniques, namely the top-down and bottom-up, are used for the preparation of hierarchical zeolite structures.

2.5. Bottom-up Zeolite Synthesis Approaches

The bottom-up approach makes use of three strategic methods during the preparation of hierarchical zeolite systems. These methods are known as hard templating, soft templating, and non-templating. The development of hierarchical zeolite systems always involves consecutive and constructive crystallization processes. When using this approach, it is important to create an extra layer of porosity during the development of the zeolite catalyst. To achieve this, an additional function is incorporated in the crystallization system by making use of a template that can perform different functions and must be different from the microporous structure directing agent (SDA), or by using a growth-altering additive, an intergrowing technique or a direct-orientated combination route of preformed zeolite nanocrystals (Chen, 2020).

2.5.1. Hard Templating

Hard-templating, also known as a solid-templating technique, generally refers to using hard templates during the preparation of hierarchical zeolites. This is due to the fact that hard templates make it easy to create mesopores by simply calcining the catalyst after the material synthesis (Chen et al., 2011; Cho & Ryoo, 2012; Jacobsen et al., 2000; Madsen & Jacobsen, 1999; Tao et al., 2003). This method uses two conditions: (i) making use of amorphous and small carbon particles, e.g., splitting carbon black particles with sizes of ~10 nm inside the synthetic gel of a zeolite. The carbon particles then blend with the formed crystals during the crystallization period of a zeolite, creating mesopores soon after calcination (Jacobsen et al., 2000). However, other types of zeolites limit the success of this method to MFI-type zeolites because they are not determined enough to accommodate any impurities (Cho & Ryoo, 2012; Madsen & Jacobsen, 1999; Tao et al., 2003). [ii] Controlling the growth of the zeolite crystals within the vacant spaces of the porous carbon (Chen et al., 2011). Carbon black, carbon aerogel, and carbon nanotubes, as well as other diverse well-ordered mesoporous carbon replicas, are mostly employed as hard templates (Cho & Ryoo, 2012; Christensen et al., 2005). Depending on the relationship and the way that the templates are organized during the synthesis method, carbon templates can create a wide range of mesoporous structures, from being significantly well-ordered and interactive to being inaccessible and not interconnected. When carbon black material is used in the synthesis, the single crystalline nature activates the hierarchical zeolite MFI (Madsen & Jacobsen, 1999). Chen et al. (2011) observed a related phenomenon during the fabrication of hierarchical zeolites such as BEA, FAU, LTA, and MFI within some limited spaces inside the three-dimensional well-organized mesoporous [2Dom] carbon. However, there is a compromise when the same method is used to synthesize hierarchical zeolite LTL, which is polycrystalline. Templates, when infused with a precise quantity of precursor equivalent to the template's pore volume, play a pivotal role in facilitating zeolite crystallization within constrained spaces (Farkaš et al., 2005). For hard templates to be effective in this process, they must meet specific criteria. These include: [i] the chemical properties of the reaction mixture must align with those of the template's surface properties, [ii] they must exhibit

stability under the conditions of synthesis temperatures, and [iii] upon the removal of the hard template, the residual zeolite material must maintain its stability (Gebbink, 2017).

2.5.2. Soft Templating

The soft-templating approach is used to generate mesopores or both micro- and mesopores by making use of surfactant molecules that are well organized within a supramolecular micelle. This approach is normally divided into primary and secondary soft templating, and the most commonly used preparation method is hydrothermal synthesis. In primary soft templating, considered surfactants are typically employed to combine the vital building units in such a way that will be able to create intra- or inter-crystalline mesopores Park et al. (2011). Compared to the hard templates, the surfactant micelle is very flexible under normal zeolite synthesis conditions. That is why the micelle is denoted as a "soft template". The geometric packaging factor and the molecular process of the functional groups are beneficial to the surfactant particle for controlling the structure. The packaging parameter is, in turn, controlled by secondary extracts known as swelling agents like trimethylbenzene, co-surfactants, and inorganic salts (Beck et al., 1992; Corma, 1997; Zhao et al., 1998). Surfactants fulfill two roles in the soft templating technique, where the hydrophilic part acts as a structure-directing agent for the development of a zeolite or anchors the surfactant into the zeolite, while the hydrophobic part acts as a mesoporogen (Choi et al., 2006; Choi et al., 2009; Inayat et al., 2012). In secondary soft templating, commercially available surfactants such as cetyltrimethylammonium bromide (CTAB) are used. When these surfactants are included in zeolite synthesis, they normally form mesoporous amorphous silica or a combined zeolite phase. To address this issue, researchers have employed a specific temperature of approximately 100ºC to age the synthesis gel for a designated period of time. Subsequently, the surfactant is introduced into the system (Zhu et al., 2011). Another synthesis method proposed by Huo et al. (1994) takes into account various interaction mixtures involving organic and inorganic species. Through this approach, researchers successfully developed new mesoporous materials with optimal combinations of organic and inorganic components. However, it should be noted that these mesoporous silicates exhibited inferior hydrothermal stability and acidity compared to the microporous zeolites synthesized by Zhao et al. (1998), Wan & Zhao (2007), and Xu et al. (2007).

2.5.3. Non-Templating

Non-templating is also known as a template-free technique that does not make use of any hard or soft templates for generating mesopores in the zeolite but only employs microporous SDAs. Some of the non-templating procedures employed for the fabrication of hierarchical zeolites include the synthesis directly by nano-crystal association with the interstitial arrangement as mesopores and the production of zeolite single crystal domains having mesopores that are intracrystalline. The non-templating technique involves serious control over zeolite crystallization, allowing the formation of the precursor nanoparticles and their growth into zeolite crystals. A conventional hydrothermal treatment or a dry gel conversion (DGC) is normally favoured by the nanocrystal assembly of hierarchical structures, and a synthetic route that favours nucleation over the crystal growth is needed (Farkaš & Barbarić-Mikoćević, 2005). During hydrothermal synthesis, the growth of crystals, and the modification of aggregation and nucleation help govern the self-assembly of nanocrystals during the development of hierarchical zeolites with an extra mesoporosity (Wang et al., 2015). Instead of using hydrothermal crystallization, the inter-growing crystallization method can be completed using the DGC process,

such as steam-assisted crystallization. Under mechanical or thermal stress, there is a high chance for it to lose the extra mesoporosity. Most of the time, the mesoporosity is not stable and is controlled by intergrowth. Extreme crystal pairing is one of the techniques that can be used to develop hierarchy by creating additional porosity through zeolite synthesis (Zhang et al., 2012). The 90º rotational intergrowths of a zeolite were employed by Zhang et al. (2012) to produce a network of an upright zeolite Mobil five [MFI] nanosheets having mesopores that are developed among nanosheets.

2.6. Top-down Zeolite Synthesis Approaches

The top-down approach makes use of post-synthetic techniques classified into different groups known as delamination and assembly, demetallation, which involves desilication and dealumination, and mixed methods known as dissolution/recrystallization. These techniques are used to develop an extra pore, such as a mesopore, in the zeolite crystalline structure. This is achieved by eliminating the entire zeolite crystalline structures that were already generated by using an extractive and destructive process (Gebbink, 2017). The desilication and dealumination approaches represent the top-down technique and are the most frequently investigated post-synthetic approaches. Microporous zeolites are normally used in these approaches and then later modified synthetically for generating hierarchical zeolite structures (Farkaš & Barbarić-Mikoćević, 2005).

2.6.1. Demetallation Approach (dealumination and desilication)

The demetallation approach involves utilizing desilication and dealumination as two distinct top-down methods to create additional porosity by removing Al and Si framework atoms from a pre-existing zeolite crystalline structure (Gebbink, 2017). Various processes such as hydrothermal treatment (steaming), physical exposure (radiation), and chemical treatments (alkali, acid, or H_2O) can be employed to induce framework atom bond-breaking. These strategies result in hierarchical zeolites with a broader pore size distribution and additional meso- or macropores (Gebbink, 2017). However, it is important to note that these techniques can compromise the zeolite structure during processing, leading to decreased overall yield and increased waste generation (Serrano et al., 2013).

Dealumination is a crucial process involving the removal of aluminium from the zeolite framework through the application of chemical agents or hydrothermal treatment. First documented by Barrer & Makki (1964), this method aims to create additional mesopores within pre-synthesized zeolite crystals. Dealumination can be achieved by subjecting the material to steam at temperatures ranging from 500 to 600ºC, or by employing even higher temperatures along with acid treatment. Throughout this process, the acidic properties and Si/Al ratio of the zeolite are altered as aluminium is extracted, leading to the formation of intracrystalline voids. However, it is important to note that dealumination often results in decreased pore connectivity and is typically applicable to aluminium-rich zeolites (Gebbink, 2017).

Desilication is the process of eliminating silicon from the zeolite framework. The method enables the generation of additional porosity without significantly altering the acidic properties by subjecting the material to post-synthetic treatment with an alkaline solution (Tzoulaki et al., 2012). Diluted alkaline solutions, whether organic, inorganic, or a combination of both, are employed for silicon extraction at elevated temperatures. Adjusting treatment parameters such as base concentration, treatment duration, solid-to-liquid ratio, and temperature facilitates the precise control of pore size/volume achieved through desilication. The challenge lies in removing Si-O bonds directly attached to Al, rendering the

desilication method particularly impactful on MFI-type zeolites with Si/Al ratios typically ranging from 20-50, as opposed to zeolites with higher Al content (Dessau et al., 1992; Gebbink, 2017; Su et al., 2003). A significant drawback of desilication is the alteration of acidic properties and material structure upon the introduction of additional pores. These modified properties influence the activity, selectivity, and longevity of zeolites when applied in catalysis (Koohsaryan & Anbia, 2016).

2.6.2. Dealumination and Assembly Approach

The chemistry of layered materials is commonly explored through two distinct research pathways, each with its own set of modifications. These pathways involve the concepts of pillaring and delamination, which contribute to the creation of a structure akin to a 'house of cards'. By employing these routes, materials with micropores and an additional pore system can be obtained. To achieve an increased porosity between zeolite layers, a two-step approach is necessary, involving the expansion of the interlayer space (swelling/intercalation) and subsequent reassembly/stabilization (pillaring) or complete separation (delamination). It is important to note that these methodologies are specific to layered zeolites. The delamination process may lead to a decrease in crystallinity and condensed porosity, often attributed to the high alkalinity involved. During the pillaring step, a liquid silica source, such as tetraethyl orthosilicate (TEOS), is commonly utilized as an organic material to occupy the space between surfactants within the interlayer region. Maintaining a consistent framework is crucial for the successful implementation of the pillaring process, ensuring that the enlarged structure of individual zeolite sheets remains intact (Gebbink, 2017).

During the process of building a "house of zeolitic cards," the creation of interlamellar mesoporosity is initiated by the complete destruction of the delaminated state of layered zeolites in order to form a structure similar to a house of cards. Intercalating surfactants between the individual layers leads to delamination, which can be further facilitated by increased alkalinity and/or an additional solvent. This results in the expansion of basal spacing and concludes with the achievement of complete delamination. The use of sonication treatment aids in achieving layer separation and the formation of a colloidal suspension, which is subsequently broken down again to establish the house of zeolitic cards (Corma et al., 1999; Roth et al., 2015).

2.6.3. Dissolution and Recrystallization

The dissolution/recrystallization methodology is a prevalent strategy for synthesizing mesoporous zeolites, employing a dual-phase technique that integrates an alkaline treatment (destructive 'top-down' approach) with a subsequent recrystallization process ('bottom-up' approach), thereby classifying it as a hybrid method. Initially, the process commences with demetallation, where zeolite crystals undergo partial dissolution under alkaline conditions, yielding smaller molecular entities. Key to this methodology is the controlled recrystallization from microporous to mesoporous structure, facilitated by the incorporation of cation surfactants like cetyltrimethylammonium bromide (CTABr) or chloride (CTACl), which serve to induce mesoporosity. This technique deliberately avoids complete dissolution of the zeolite crystals by exposing them to surfactants, thereby promoting the reconstruction of the zeolite framework around surfactant micelles. The disintegrated framework atoms of the original zeolite subsequently become nucleation sites for recrystallization, with the surfactant acting as a templating agent to introduce additional porosity (García-Martínez et al., 2012; Gebbink, 2017). Recrystallization is enhanced under hydrothermal conditions, typically between 100-

150ºC, utilizing CTAB as a structure-directing agent (Gebbink, 2017). Through this process, characterized by advanced analytical techniques such as XRD, TGA, and MAS NMR, Ivanova et al. (2014) revealed that the desilication in an alkaline milieu post-initial bond disruption facilitates the formation of enlarged inter- and intra-crystalline pores. The exchanged CTA cations, replacing Na^+, form micelles that assist in the diffusion of CTAB molecules into the created voids, thereby enhancing the zeolite's hierarchical structure (Ngoye et al., 2014). This dissolution/recrystallization mechanism has thus proven integral to the development of hierarchical zeolites in the referenced study.

2.7. Modern Approaches to Zeolite Synthesis

Recent publications have criticized the application of conventional top-down and bottom-up approaches to zeolite synthesis. Stating reasons such as the use of hazardous and expensive solvents, costly precursor materials, large quantities of alkaline/acidic solutions, and high energy requirements, and these requirements have led to environmental and economic issues (Maghfirah et al., 2020). In recent years, advancements towards zeolite production have been focused on introducing green synthesis methods. These would include incorporating sustainable starting materials, green templates that are affordable and less toxic, solvent-free methods that reduce secondary waste and crystallization pressure, and template-free methods that can increase product yield (Chen, 2020).

2.7.1. Solvent-free Method

The solvent-free synthesis method has shown the potential to reduce energy requirements, enhance zeolite production efficiency, and decrease the production of secondary waste. This method involves mixing all the starting materials in the absence of a solvent. Then, through gas-phase transport of the reactants, the mixture is crystallized in a sealed autoclave (Ren et al., 2012). However, the crystalline structure obtained is usually microporous with a stretched diffusion pathway for molecules. Luo et al. (2017) employed nanosized ZSM zeolite seeds during the crystallization process to reduce the length of the diffusion pathway. The starting materials for the solvent-free synthesis included fumed silica, tetrapropylammonium bromide (TPABr), $Na_2CO_3 \cdot 10H_2O$, and $NaAlO_2$ (as an alumina source). The zeolite ZSM-5 obtained consisted of a micro-/mesoporous structure with a high surface area and a nano-sized crystal structure (10-40 nm).

2.7.2. Green Starting Materials

The study of low-cost and renewable materials, similar to those reviewed in *section 2.9*, has sparked interest in the fabrication of zeolites within the context of green synthesis. These materials (rice husk, coal fly ash, diatomite, kaolin) are often undesirable products from industrial applications and contain crystalline mineral phases that are rich in alumina-silica composition (Maghfirah et al., 2020). The versatility of these low-cost materials for zeolite synthesis is vast, which would include conversion into inter- and intracrystalline mesopores, pre-treatment and subsequent zeolitization to form mesopores, and in some instances, they might possess original mesopores. Alaba et al. (2015) pre-treated kaolin for the synthesis of Hierarchical nanoporous HY zeolite. The pre-treatment stages involved thermal activation at 850°C for 2 h, followed by H_2SO_4 treatment at 90°C for 3 h. Post-treatment, the kaolin underwent hydrothermal synthesis to obtain HY zeolite. Hierarchy was achieved by manipulating the aging and crystallization time and monitoring the hierarchical factor.

2.7.3. Mesoporogen-free Method

The application of mesoporogen-free synthesis has seen growing attention due to its capability to reduce the energy required to remove the mesoporogen and eliminate the need for hazardous and expensive surfactants (Guo et al., 2019). Literature examples include the work done by Kadja et al. (2016), where they synthesized an intercrystalline mesoporous ZSM-5 zeolite at a temperature that was below 100°C. The synthesis reactor was a polypropylene vessel consisting of TPABr, silica, and alumina precursors and no presence of mesoporogen. Similar work was conducted by Valtchev et al. (2005), who synthesized a nanosized Zeolite A catalyst using an organic-template-free gel system at room temperature. A synthesis process that would take 3 weeks was significantly reduced to 3 days through the optimization of the synthesis conditions (molecular composition and synthesis time).

2.8. Zeolite Influences in Catalytic Application

Most reactions, during heterogeneous catalysis, occur on the superficial part of the catalyst particles. To obtain inherent perspectives into how a particular chemical or structural component affects the catalytic efficiency, it is necessary to develop innate correlations between clearly described chemical and framework properties of catalyst particles and their catalytic activity via the bridge of chemistry and framework of the surface of catalyst particles. By doing so, an intrinsic perception of how a particular chemical or morphological component affects catalytic activity can be attained. Owing to this knowledge, catalysts may be fabricated using a logical design approach rather than by trial and error, as is currently the case. In many circumstances, a catalyst's structure, size, and shape affect its catalytic efficiency. Particles of a catalyst with varied forms could have various crystallographic structures; the packing density and even the electrical form of atoms on several surfaces could all be extremely distinct (Cao et al., 2016).

Size and shape-reliant parameters are intimately linked to the superficial chemistry and catalyst morphology, which primarily controls the catalytic efficiency. This can be attributed to the occurrence of catalytic activity at a solid-gas or solid-liquid contact on a catalytic site of the catalyst surface as a result of essential fundamental processes known as surface adsorption occurring on the catalyst interface. Since each facet of a catalyst's particle has a unique binding arrangement and strength, each aspect of the catalyst's particle can create distinct surfaces with terraces, steps, and corners on the surface of the catalyst's particle. Consequently, the effects of the size and shape of a catalyst's particle on its catalytic efficiency are mostly represented by variations in the chemical and morphological variables of the catalyst's surfaces. Furthermore, the effects of the various promoters used on the chemical characteristics of the resultant catalyst, as well as the activity of the resulting catalyst in terms of increasing the preference for lower olefins, have been investigated. It has also been described how several parameters, including the acidity of the zeolite, the Si/Al ratio, and the working conditions, affect the process pathway (Cao et al., 2016).

2.8.1. Zeolite Structure (crystalline framework, size, and shape)

Zeolites are organized in a crystalline structure consisting of a tetrahedron of TO_4 (T is Si or Al in a native zeolite and can be other elements, including Ga, Ge, Fe, B, P, Ti in a synthesized material) joined by oxygen atoms (Zhang & Ostraat, 2016). Molecular access to the zeolite structure is provided through channels and cavities with diameters of roughly one nanometer (Serrano et al., 2013b), which are available for various molecules. The mixture of silicon and oxygen in tetrahedra produces a solid

that does not have any charge (SiO_2). When Al is introduced into a silica structure, the structure is negatively charged as a result of the Al. This occurs as a result of the Al^{3+} and Si^{4+} substitution and necessitates the use of compensatory cations to maintain the overall framework's neutrality. ZSM-5 (MFI zeolite) has a morphology comprising unit cells with 10 rings of 5 T-atoms, which are linked together by oxygen atoms to an identical chain, forming a channel (***Figure 2.5***). The channels of ZSM-5 zeolite work together to generate a three-dimensional framework. ZSM-5 also has a significant silicon-to-Aluminium ratio (Si/Al > 11), which is beneficial. Interestingly, this ratio has a significant impact on the ion exchange capacity, with the concentration of Al in the framework increasing in direct proportion to the amount of charge-compensating cation present (Wang et al., 2017). Zeolite materials have unique characteristics, including a wide surface area, good thermal stability, increased ion exchange capacity, the existence of acid sites, and shape specificity (Feliczak-Guzik, 2018). While the morphological micropores of zeolite are advantageous for the mass transfer of small molecules, they are detrimental to the mass transfer of large molecules, as evidenced by diffusion restrictions for reagents, intermediates, and products (Fang et al., 2008). Many investigations have been conducted recently in an attempt to produce zeolites with mesopores and reduce the diffusional constraints of these materials (Kustova et al., 2010).

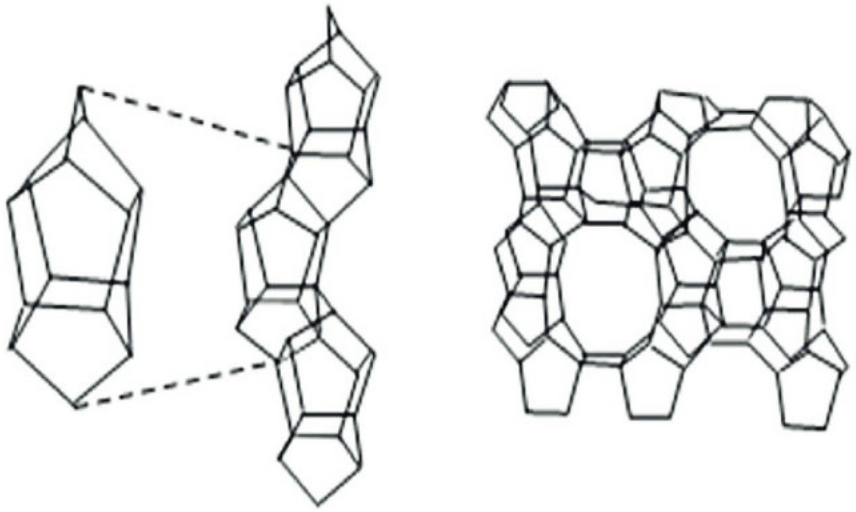

Figure 2.5. Tetrahedrons Structure of ZSM-5 zeolite [adapted from Lounis & Belarbi (2018)]. (Copyright 2023, with permission from Elsevier).

2.8.2. Effect of Crystalline Framework, Size and Shape on Catalytic Performance

Due to the varied geometric structures and electrical states of distinct crystallographic surfaces of a nanoparticle, they may have diverse activity and/or specificity for a similar catalytic process if they are formed from separate crystallographic surfaces (Narayanan & El-Sayed, 2005; Zhang et al., 2013) As a result, nanoparticle catalysts of varying sizes and shapes typically display distinctly varied catalytic activities (Chen et al., 2009). The asymmetry in the geometric morphology and electrical form of catalyst atoms connected with distinct crystallographic surfaces is essentially responsible for the reliance of catalytic efficiency on the shape of the catalyst's crystallographic surface. The band framework of a metal nanoparticle with a size of 1–2 nm could cause it to act more like a molecule than a metallic form. For example, it was noted by Cleveland et al. (2015) that an Au nanoparticle less than 1 nm displays a molecular rather than a metallic form when viewed from the perspective of its

electronic state. Contrary to a metal nanoparticle with a greater size, the molecule-like electrical form of a metal nanoparticle at 1–2 nm may demonstrate inherently variable catalytic activity than a nanoparticle with a smaller size (Cao et al., 2016).

By employing a conventional hydrothermal procedure without the addition of a secondary template, researchers were able to create a wool-ball-like ZSM-5 morphology. When likened to the typical ZSM-5 catalyst, it had a greater exterior surface area and a shorter diffusion length, respectively. Due to better diffusion of reactants, it demonstrated an increased conversion efficiency of *n*-octane. The transformation of isopropyl benzene cracking on wool-ball-like ZSM-5 was retained at 80% after 27 hours; however, the transformation over traditional ZSM-5 declined to 40% after 10 hours of response time (Zheng et al., 2016). By incorporating the micro-emulsion mechanism and the ZSM-5 crystal-seed crystallization techniques, Firmansyah et al. (2016) created a fibrous silica ZSM-5 with the characteristics of increased surface area (554 m^2g^{-1}), large pore diameter (2–20 nm), and an abundance of strong acid sites. It demonstrated great activity in the cracking of cumene, di-ispropylbenzene (DIPB), and tri-isopropylbenzene (TIPB), as well as strong availability and minimal diffusion restriction for molecules. Following a hundred pulses, the cumene transformation remained at 90%, but the conversion using the typical ZSM-5 dropped to 50% after a hundred pulses. Moreover, an electrospinning approach was used to create hierarchical ZSM-5 fibres with different pores [macro, meso, and micro] (Liu et al., 2014). During coaxial electrospinning, it is possible to manage the macroporous morphology by varying the pace at which inner fluid is injected. The cracking of iso-butane revealed that the fabricated hierarchical ZSM-5 hollow fibres had stronger light alkene specificity (41%) and appreciable coking-resistant efficiency. Even after 60 hours of reaction, the transformation rate remained at approximately 95%. As a result of the synergistic impact between the dehydrogenation performance of Ga_2O_3 and the cracking activity of ZSM-5, a Ga_2O_3/ZSM-5 bifunctional hollow fibre catalyst with improved catalytic performance and light alkene selectivity was developed using the hierarchical ZSM-5 hollow fibres. According to Han et al. (2016), the greatest output of light olefins and aromatics from *n*-butane cracking over Ga_2O_3/ZSM-5 was 88%, i.e., 56% greater than the yield from ZSM-5. According to Fu et al. (2016), two types of zeolites were synthesized, each with a distinct morphology (nano-sphere crystallite agglomeration versus nano-rod crystallite agglomeration) but similar acid characteristics. The catalytic performance of the nano-sphere crystallite cluster ZSM-5 was superior to that of the nano-rod crystallite cluster ZSM-5, owing to its increased diffusion efficacy and acid sites availability, which were due to the relatively wide outer surface area and mesopore volume compared to the latter.

A ZSM-5 zeolite with hierarchical porous structures was created to enhance reactant migration and acid site accessibility in micropores. This advancement was achieved by reducing the diffusion rate in micropores compared to standard ZSM-5 zeolites (Chen et al., 2012; Zhang & Ostraat, 2016). According to Garcia-Martinez et al. (2014), employed various techniques such as electron tomography, 3-dimensional rotation electron diffraction, and high-resolution gas adsorption to investigate intracrystalline mesopore networks and their connectivity. Intracrystalline mesopores, acting as pathways linking micropores, can promote molecular transformation, thus enhancing catalytic efficiency and preventing carbon accumulation on crystal surfaces. Studies have shown that hierarchical ZSM-5 zeolites display superior catalytic cracking performance compared to pristine ZSM-5 zeolites, attributed to enhanced diffusion rates and acid site availability (Yin et al., 2013; Zhang

et al., 2013). Different methods such as double templating with hard-template technique, double templating with soft-template technique, single template approach, and post-treatment approach can be utilized for the synthesis of hierarchical zeolites.

2.8.3. Active Acid Sites

Strong and weak acid sites can be found in ZSM-5 zeolite. Each has a unique function in the hydrocarbon cracking process. By modulating the activation energy of the process, the catalyst acid strength can dominate the reaction route during catalysis, for instance, the catalytic cracking of 1-pentene. 1-Pentene is preferred by the weak acid sites over propylene in terms of cracking. The strong acid sites favour splitting 1-pentene to ethylene over the other way around. Then, by varying the acid strength of ZSM-5 (Lin et al., 2015) it is possible to manage the P/E ratio (around 1.2 and 7.9). Furthermore, the acid strength of ZSM-5 zeolite can be altered by fabricating isomorphous ZSM-5, which are amorphous ZSM-5 zeolites with different crystal structures. These compounds are made by substituting an Al source with a Ga or Fe source in an Al-containing fabrication mixture. It was discovered that the acid strength of isomorphous ZSM-5 zeolites improved in the order listed: MFI-Al>MFI-Ga>MFI-Fe. A reduction in acidity strength makes cracking products simpler to desorb, which may inhibit the subsequent process between light alkenes generated from the original cracking process, leading to increased light alkene specificity and less carbon accumulation (Ji et al., 2017). Hodoshima et al. (2016) fabricated a zeolite that contained Fe, Ga, and Al simultaneously. In comparison to normal ZSM-5 zeolites, the acid strength of Fe-Ga-Al/ZSM-5 zeolites is relatively weak, which improves the specificity of propylene and reduces the production of carbon. According to Furumoto et al. (2011), the acid strength and activation energy of ZSM-5 zeolite comprising Fe were both insufficient to catalytically crack hydrocarbons efficiently.

The presence of acid sites in zeolites is important for catalytic processes; nonetheless, finding the locations of acid sites and managing their distribution in zeolites pose significant obstacles. The zeolite active acid sites are divided into two: Brønsted and Lewis acid sites. Zeolites comprising a variety of heteroatoms have demonstrated a range of catalytic activity (Liu et al., 2014; Lu et al., 2015; Peng et al., 2015). The formation of Brønsted acid sites in zeolite pores occurs when trivalent atoms, including Al, are substituted for Si in a structure, and charge adjustment is offered by protons. These acidities are formed, in general, by the identities and locations of heteroatoms. Current investigations have also demonstrated that extra-framework species (frequently formed due to post-synthesis hydrothermal processes) can also affect the performance of neighbouring Brønsted acid sites and, thus, the catalytic application. Research has revealed that the placement of Al atoms in a zeolite is influenced by the Si/Al and the fabrication process (Kim et al., 2013; Rahimi & Karimzadeh, 2011), which may result in varied catalytic activity for a similar kind of zeolite structure depending on the fabrication technique.

Consequently, when comparing the research data provided by several groups, caution should be exercised due to the fact that their zeolites were obtained from various resources that could conflict. Blasco et al. (2006) noted that the increase in Al dosage makes the Brønsted protons more likely to be detected at channel junctions. Lewis sites serve as the extra-framework species that interact with nearby Brønsted sites in a synergistic manner (Ghorbanpour et al., 2015). Various metal-interchanged zeolites have varying levels of stability, and as a result, they have various degrees of propensity to trigger the movement of framework metals to locations outside of the framework. In hydrothermal

treatments, the Ga- or Fe-replaced ZSM-5 exhibit lower stability than the Al-exchanged zeolites, allowing the structure of Ga and Fe to move to extra-framework regions more readily than Al-exchanged zeolites. A similar observation (low stability) was reported by Miyake et al. (2016) for ZSM-5 zeolites that have been altered with Ga, Zn, Al, Cu, and Fe. The extra-framework aluminium species are the most extensively researched of the various extra-framework species available.

2.8.4. Effect of Acid Sites on Catalytic Activity

The existence of an excessive quantity of acid sites on the external surface of ZSM-5 during the catalytic processes might result in significant carbon accumulation on the outer surface, which would cover the surface or completely plug the pore opening. Thus, the acid sites in the micropores are unable to catalyze the reactants efficiently, leading to rapid deactivation. Consequently, passivating the acid sites on the exterior surface can improve the catalytic activity. It was discovered that a post-synthetic HNO_3 treatment procedure may be used to preferentially eliminate the acid sites on the exterior surface. Consequently, the modified ZSM-5 retained increased catalytic performance (approximately 96%) with minimal carbon accumulation (50 $mg.g^{-1}$) after 455 minutes of process time, whereas the transformation of the unmodified ZSM-5 reduced to approximately 67% with significant carbon build-up [120 $mg.g^{-1}$] (Inagaki et al., 2015). Conversely, this approach is only viable when the treated zeolite has been synthesized without an organic structure-directing agent (OSDA). With the aid of the OSDA, the outer surface Al and the vast structure Al would be dissolved by HNO_3 pre-treatment for zeolites created with OSDA support (Ji et al., 2017). With the incorporation of a silicalite-1 shell to the outer surface of the ZSM-5 zeolite, (Ghorbanpour et al., 2015) fabricated a zeolite with passivated surface acidity. After the addition of the silicalite-1 shell, just a few acid sites can be found on the exterior surface of the ZSM-5 catalyst. Consequently, the carbon build-up on the exterior surface of the product can be reduced, leading to higher selectivity for the product.

The incorporation of MgO on the exterior surface of ZSM-5 was shown to deactivate the acid sites on the zeolite's surface (Zhang et al., 2015). Magnesium acetate was chosen as the precursor due to the fact that it polymerizes in an aqueous solution to form large-molecule coordination complexes that are unable to penetrate the micropores. Then, following calcination, MgO was deposited on the exterior surface, deactivating the acid sites on the external surface. The level of carbon accumulation was reduced following the MgO treatment. In addition, a mechanochemical technique includes the application of powder particles to deactivate the acid sites on the surface. The surface of a catalyst was subjected to shear force, which deactivated the acid sites on the exterior surface in a controlled manner. It was discovered that the ZSM-5 zeolite had limited performance on TIPB cracking after it was subjected to mechanochemical treatment (Inagaki et al., 2015). This indicated that there were just limited acid sites on the surface of the ZSM-5. The catalytic cracking of several forms of hydrocarbons over the adjusted HZSM-5 catalyst has been explored to increase the synthesis of light olefin by zeolites. The process proceeds at 550–650°C., which is approximately 200°C less than the temperature at which steam cracking occurs, and the production of ethylene and propylene is substantial compared to the yields of steam cracking products. Although the influence of feed source on the lower olefins ratio is not as significant as that of steam cracking, it should be noted that the ratios of P/E may be altered by modifying the acid type, strength, and distribution, i.e. Lewis/Brønsted (L/B) acid sites, and also the process parameters (Rahimi & Karimzadeh, 2011). Further study and effort are required to

develop the inherent techniques for catalyst development and fabrication in an attempt to exploit commercial viability.

2.8.5. Modification of Zeolite through Si/Al Ratio

Zeolite acidity is largely determined by their Si/Al molar ratios and the altering promoters used (Jung et al., 2004). Generalizations aside, the extremely high hydrothermal stability of ZSM-5 is linked to the high Si/Al ratio of the catalyst (Wan et al., 2008). Due to the reduced Al composition in the ZSM-5 structure, the degree of Al separation from the structure is limited, and the incidence of structure breakdown during steam treatment is reduced (Wan et al., 2008). As a result, the crystal lattice stability improves with increasing Si/Al ratio (Hagen, 2005), resulting in increased crystallinity. In response to dealumination, the number of acidic sites is reduced; however, the acidity centers increased until the efficiency of dealumination reached approximately 50%. The opposing impact of concentration and the strength of their acid centers are superimposed, resulting in the achievement of the highest reactivity at a specific SiO_2/Al_2O_3 ratio (Hagen, 2005). A variety of 8–12-MR (member rings) zeolitic catalysts were used to explore the cracking of naphtha range alkanes and naphthenes. The goal was to evaluate the association between zeolitic Si/Al ratio and naphtha cracking performance. At 650°C, the largest production of lower olefins was achieved over 10-MR zeolites, including ferrierite, with an 83% naphtha transformation and a 54 wt.% preference for ethylene and propylene. The relative performances and selectivity of the catalysts at 650°C revealed that beta (Si/Al = 66) and ZSM-22 (Si/Al = 62) showed the best performance among the catalysts tested (Xu et al., 2007). Light alkanes and coke are more selectively absorbed by 12-MR zeolites than ethylene and propylene, resulting in increased specificity for light alkanes and coke at the cost of ethylene and propylene (Xu et al., 2007).

The effect of Si/Al ratio on the production of light olefins is also studied in catalytic cracking. At temperatures ranging from 200 to 600°C, Jung et al. (2004) discovered that increasing the Si/Al ratio of ZSM-5 (25, 75, and 100) resulted in a substantial reduction in the transformation of *n*-octane. The specificity for olefin gradually increases as the reaction temperature is raised, irrespective of the Si/Al molar ratio in the fabrication mixture. The number of acid sites with increased acidity, in contrast, has a significant impact on the conversion but not on specificity (Jung et al., 2004). It was previously reported by Xu et al. (2007) that improving the Si/Al ratio (24 to 66) reduces the occurrence of hydride exchange and aromatization reactions. Moreover, it was discovered by Zhu et al. (2005) that a high Si/Al influenced the catalytic cracking of butene to propylene over ZSM-5 catalysts, and they suggested that the specificity and the total production of propylene and ethylene improved by increasing the Si/Al ratio (Zhu et al., 2005). Furthermore, increasing the Si/Al ratios significantly improves the stability of the catalysts. With a ZSM-5, Si/Al = 50, the transformation went from 97 to 68%, i.e., 29% lower after 10 hours of reaction, whereas with a Si/Al = 366, the transformation decreased from 85 to 81% (Zhu et al., 2005), i.e., just around 4% lower after 10 hours of running. In comparison to the previously stated findings, Kubo et al. (2018) discovered that when the Si/A1 declined (75 to 20), the production of propylene and ethylene improved from 29 to 38%.

2.8.6. Modification of Zeolite with Various Elements

The promotion of HZSM-5 with alkaline earth metals (AE) (i.e. Mg, Ca, Sr, and Ba) had an impact on the activity of the catalyst during the reaction, including the catalytic cracking of *n*-butane (Wakui et

al., 2002). The carbonate salt [AE(CO_3)] of each AE was added to the aqueous solution employed for the fabrication of the zeolites, which resulted in modifications to the final zeolites. When comparing the alkaline earth-adjusted ZSM-5 to the non-promoted HZSM-5 zeolites, it was discovered that the modified ZSM-5 produced a greater output of ethylene and propylene. Over Ba/ZSM-5, appreciable results (propylene and ethylene = 4.5%) were achieved (Wakui et al., 2002). However, the authors did not provide any information on the stability of the modified catalyst (Wakui et al., 2002).

ZSM-5 modification with rare earth metals has been investigated as well. Xiaoning et al. (2007) studied the impact of rare earth (RE) on the morphology, acidity, and catalytic activity of HZSM-5 to achieve lower olefin synthesis. Favourable propylene yields were achieved at 600°C for Nd, Ce, and La/HZSM-5 with 25.9%, 25.2%, and 25.2%, respectively, over three catalyst systems. Overall alkene production of 57 wt.% was obtained over Ce/HZSM-5 at 600°C while 60 wt.% was obtained over Nd/HZSM-5 at 650°C (Xiaoning et al., 2007). The ratio of P/E varies substantially depending on the process temperature and the kind of RE element involved in the process. As an outcome of the results, it was discovered that the RE-doped HZSM-5 improves the specificity to lower olefins, hence increasing the production of olefins while simultaneously decreasing the production of aromatics in the catalytic cracking of butane. However, the study conducted by Wakui et al. (1999) at 650 °C produced a total propylene and ethylene yield of 48 wt.% in the catalytic cracking of *n*-butane over La impregnated HZSM-5 (Si/Al = 200) catalysts (Wakui et al., 1999). The production of propylene and ethylene increased to 58% at 650°C when a dehydrogenation-cracking double-stage process was proposed, with Pt-Sn as the catalyst (Wakui et al., 2002). The suggested procedure involves first dehydrogenating *n*-butane to *n*-butene (1-and 2-butene) over a catalyst composed of Pt–Sn/Ca–ZnAl2O4 as a dehydrogenation catalyst, followed by consecutive conversions of *n*-butene to ethylene and propylene over a cracking catalyst (10 wt.% Pr/ZSM-5). Consequently, it can be established that adding RE metals into HZSM-5 can improve the efficacy of the catalyst during the cracking of butane. Moreover, after a thorough investigation, it was established that the synergic influence of La and P is significant in achieving favourable outcomes over P-La/ZSM-5 for lower olefin synthesis. Implementing the use of two different elements, such as RE metals and P, to alter zeolite may lead to the creation of RE–P–O oxides, which precipitate on the zeolite's external surface and cover some acid sites on the surface (Liu et al., 2014). Lanthanum also prevents the leaching of P species from the zeolite when it is exposed to elevated temperatures and steam. A reduction in surface acidity has been observed after zeolite has been modified with rare earth metals and phosphorus combined (Liu et al., 2014; Xue et al., 2010). This has been observed as a consequence of the interplay of the rare earth metal cation with the phosphate anion.

The fluorinated HZSM-5 has the potential to be an excellent catalyst for the cracking of naphtha to produce lower olefins in a variety of applications. To develop the F-Modified HZSM-5 samples, HZSM-5 (Si/Al = 46) was immersed in an aqueous solution of NH_4F for some time. Feng et al. (2010) discovered that the highest propylene and ethylene production attained 36% and 20%, respectively, at 600°C [using (0.1 wt.%) F/HZSM-5], which contained the highest Brønsted acid quantity, which was 7.3 and 4.3% greater than the highest yields obtained over the unmodified HZSM-5 respectively (Feng et al., 2010). In the FT-IR analysis of pyridine adsorption on F/HZSM-5, it was discovered that the addition of fluorine significantly increases the acid content of HZSM-5. The BET surface area and

pore volume of F/HZSM-5 both improved, mostly as a result of the expansion of the micropores. Besides regulating the pore properties of HZSM-5, fluorine adjustment also regulates the quantity of acid sites in the zeolites, particularly the density of Brønsted acidity, which may be advantageous for achieving increased conversions of naphtha as well as elevated specificity for light olefins (Feng et al., 2010). Van Mao et al. (1999) discovered that the surface acidity of F-ion-substituted ZSM-5 was improved due to the production of new Brønsted acid sites and the reinforcement of some acid sites in the original zeolite. According to the authors, this was caused by the proton attack of the zeolite surface by the chemisorbed H-F ion pair. However, under these fabrication circumstances, the zeolite structure is completely retained (Van Mao et al., 1999).

2.9. Industrial Waste Resources for Zeolite Production

Zeolites have found applicability as catalysts in a variety of industries, such as fine chemicals, petrochemistry, and refining. The factors affecting zeolite composition during synthesis include the compensating cations (Ca, K, Na, Ba, Sr, and Mg), templates, crystallization time and temperature, precursor material, and Si/Al ratio. However, zeolite production methods are reported to be relatively expensive for commercial application due to the nature of the starting materials (sources of silica and alumina and templates). In addition, solubilization of the sources of silica and alumina often requires high temperatures (> 100°C), thus making the process energy-intensive (Alves et al., 2014). Therefore, several studies have focused their attention on developing low-cost synthesis techniques with good reproducibility. One technique that has been studied in recent years is the use of low-cost industrial wastes in the synthesis of zeolites. Several studies have reported the use of raw wastes such as coal ashes (Bieseki et al., 2013), clay minerals (San Cristóbal et al., 2010), metallurgical residues (Sugano et al., 2005), and agricultural waste (M. M. Mohamed et al., 2008). Each of these low-cost wastes is reviewed in the subsequent sections; however, a summary of their typical compositions is shown in ***Table 2.1.*** Furthermore, these studies have shown the synthesis of various types of zeolites (Y, X, A, ZSM-5, mordenite, and sodalite) and how the chemical composition of the starting material significantly affects the synthesis outcome.

Table 2.1. A summary of compositions (wt.%) for low-cost industrial wastes for zeolite production [adapted from Sayehi et al. (2020)]. (Copyright 2022, with permission from Elsevier).

Industrial Waste	**CaO**	**MgO**	**SiO_2**	**Al_2O_3**	**Fe_2O_3**	**Minor traces**
Blast furnace slag	40-50	5-10	30-40	10-15	0-1	Mn, S
Zing non-ferrous slag	15-20	2-5	15-20	7-10	30-40	S, PbO, ZnO
Waste foundry slag	0-5	0-3	75-90	0-15	1-6	P, Ti, Mn
Coal fly ash	3-15	1-5	40-60	15-40	3-12	S, P, Ti, Mn
Municipal waste incineration bottom ash	15-50	1-3	10-30	1-15	0.5-7	Pb, Zn, Cr, Cd, Hg, Cu, Ti, SO_3
Wheat straw ash	8-12	0-4	50-55		0-2	
Rice husk ash	1	0.5	90-93	0.5	1	

2.9.1. Coal Ash Residues

Ash is an inorganic powdery residue generated by thermal transformation or fuel combustion processes. The composition of ash varies based on the different feedstocks used during thermal

transformation. However, it mainly consists of various minerals and silica-based compounds (Munawar et al., 2021). Coal is still the most widely used material for the production of electricity in some countries: India (69%), Poland (92%), South Africa (93%), and China (79%), and the global contribution of coal to electricity generation is expected to slightly increase to 44% in 2030 (Mehmood et al., 2012). Coal is burnt in power plants to supply energy, and fine particulates are released along with flue gas at the top of power plants. The fine material that leaves at the top is referred to as fly ash; however, it is collected and mixed with the residual coal ash (bottom ash). This mixture, which is made up of 20% bottom ash and 80% fly ash, is called coal fly ash (Bukhari et al., 2015). Therefore, coal combustion is the main process that produces coal fly ash (CFA), which is a powdery residue that is mainly composed of CaO, MgO, Fe_2O_3, SiO_2, Al_2O_3, and K_2O (***Table 2.2***). Minerals found in CFA include hematite, mullite, magnetite, α-quartz, and non-crystalline aluminosilicate (Chehreh Chelgani, 2019). This implies that the CFA's physicochemical properties depend on the type of coal (lignite, bituminous, anthracite, and subbituminous) used in power plants.

Table 2.2. Typical coal fly ash chemical composition [adapted from Zhang et al. (2022)]. (Copyright 2022, with permission from Elsevier).

Type and location of power plant	Fe_2O_3	Al_2O_3	SiO_2	CaO	MgO	K_2O	Na_2O	TiO_2
Thermoelectric, Brazil	4.88	20.54	67.53	1.53	0.87	1.83		0.76
Coal-fired, China	10.339	19.425	57.091	4.919				
Coal-fired, Britain	9.71	27.05	44.53	2.80	0.47	4.42	2.37	2.95
Thermoelectric, China	8.28	17.20	34.90	26.30	1.87	1.14	0.73	
Coal-fired, Iran	18.07	28.73	37.88	11.54	1.79	0.34	0.29	

Coal fly ash can be classified as Class F or C, and this is based on the proportions of the major compounds: iron, aluminium, silicon, and calcium. For instance, in class C, the composition of $Fe_2O_3 + Al_2O_3 + SiO_2$ lies between 50 to 70 wt.%, whilst CaO is greater than 20 wt.%. Meanwhile, in Class F, the composition of $Fe_2O_3 + Al_2O_3 + SiO_2$ is greater than 70 wt.%, whilst CaO is less than 10 wt.% (Zhang et al., 2022). Furthermore, Class F contains less CaO due to it being produced by high-ranked coals (bituminous and anthracite), whereas Class C contains more CaO due to the use of lower grades of coal [lignite and subbituminous] (Bukhari et al., 2015). Irrespective of the variability of CFA globally, several investigations have proved the successful use of CFA for zeolite synthesis.

Fly ash discarded from a thermoelectric power station was investigated for its reactivity to produce sodium-containing zeolites (Monzón et al., 2017). The fly ash sample was pre-treated using alkaline fusion, calcination, and ball milling to aid the hydrothermal synthesis. Guo et al. (2016) reported the inadequacy of using granularity refinement as a pre-treatment method in the extraction of alumina from coal gangue. It was recommended that a calcination step be added to improve alumina's dissolution. However, calcination is an energy intensive process and does not effectively remove other mineral impurities [lime, anhydrite, hematite] (Panitchakarn et al., 2014). Ojha et al. (2004) investigated the use of various types of acids (HNO_3, H_2SO_4, and HCl) for the removal of impurities from CFA. A highly pure zeolite molecular sieve was obtained with HCl. However, the use of acids for pre-treatment formed secondary pollution. The coal-based solid wastes discussed by these authors

contained impurities in the form of clay minerals (kaolinite) or alkali metal oxides (TiO_2, Fe_2O_3, CaO, and MgO), which attracted the need for pre-treatment.

2.9.2. Fly Ash from Municipal Solid Waste Incinerator (MSWI)

Incineration is an integral waste management strategy that has been used for the disposal of municipal solid waste (MSW) due to its ability to handle large volumes of MSW and produce heat in the form of steam or electricity. China is reported to treat 60% of its MSW through incineration, resulting in increased production of fly ash from MSWI (Pan et al., 2013). The particle size of MSWI fly ash ranges between 10-50 μm (Mangialardi, 2003), thus providing sufficient surface area for the diffusion of toxic heavy metals into water streams. The metals contained in MSWI fly ash include Cd, Zn, Ni, Cu, Hg, and Cr (Haiying et al., 2010), which is why it is considered hazardous waste. However, the waste also contains mineral compounds such as hematite, anhydrite, portlandite, quartz, and gehlenite (Rodella et al., 2017), which could be of possible use for secondary application in zeolite synthesis. Of course, MSWI fly ash requires pre-treatment procedures to stabilize it.

Elinwa & Ejeh (2004) performed various characterization techniques (XRF, XRD, and SEM) on a MSWI fly ash sample that was sourced from an Incineration Plant in France. The XRF analysis revealed the major oxide compounds: SiO2, CaO, and Al_2O_3, which were reported to be 27.23%, 16.42%, and 11.72%, respectively. The most abundant crystalline minerals, as identified by XRD, were halite (NaCl), Sylvite (KCl), and quartz (SiO_2). Bottom ash MSWI was converted to a zeolite-type material for the adsorption of heavy metals (Chiang et al., 2012). The bottom ash MSWI samples used were obtained from a moving-grate furnace and contained minimal impurities. The samples were hydrothermally treated using harsh alkaline conditions and converted into a mixture of tobermorite [$Ca_5Si_6(OH)_2 \cdot 4H_2O$] and sodium aluminum silicate hydrate ($Na_2O \cdot Al_2O_3 \cdot 1.68SiO_2 \cdot 1.73H_2O$). Deng et al. (2016) used hydrothermal and fusion treatment methods to synthesize zeolite-like materials from MSWI fly ash. Due to the low amounts of Si (0.3%) and Al (2.2%) in the fly ash sample, the authors had to adjust the Si/Al molar ratio using Al_2O_3 powder and waste glass powder (Si = 56.1%). The XRD, FTIR, and TGA results demonstrated that the synthesized material had zeolite-like characteristics.

2.9.3. Biomass Ash

Energy production from biomass has been identified as a favoured source of energy, and it has been reported that biomass contributes 10.3% to the global energy supply (Munawar et al., 2021). This is due to its ability to reduce up to 95% of CO_2 emissions. From a commercial perspective, power plants utilize different biomass feedstocks, including wheat straw, agricultural residue, wood residue, rice husk, and wood chips (Baetge & Kaltschmitt, 2018). A major challenge in the commercial combustion of biomass feedstocks is the production of biomass ash, of which, the global production of biomass ash is estimated at 480 million tonnes per annum and is comparable to that of coal fly ash (780 million tonnes per annum). Overall, ash from biomass-fired power plants consists of metal oxides (SiO_2, Al_2O_3, CaO, MgO, K_2O) and mineral matter with amorphous, semi-crystalline, and crystalline structures (Vassilev et al., 2013).

Common biomass ashes that have been explored for the synthesis of zeolites include rice husk and palm husk ashes due to their relatively high silica composition (Faizul et al., 2013). Rice husk ash (RHA) is considered a carbon-neutral material obtained from burning rice husk in boilers and is

composed of 10-40% carbon, 60% silica, and other mineral phases (Sayehi et al., 2020b). Mukherjee et al. (2018) solubilized silica from rice husk by initially soaking it in 1 M of HCl solution, followed by calcination at 700°C, and mixing it with 2 M of NaOH solution for 12 hours whilst heating. The resulting silica gel was mixed with sodium aluminate to form zeolite Na-A, which was used as an adsorbent for fluoride removal. Bohra et al. (2014), on the other hand, used RHA (as a silica source) and aluminium foil (as an alumina source) to synthesize zeolite powders (Na-P and Na-A). The low-cost organic-free wastes were treated through hydrothermal conditioning at the following conditions: 15-96 h and 100°C.

2.9.4. Iron and Steel Slags

Metallurgical slags are by-products generated from the refining and smelting of metals. These materials are made up of an amorphous or glass-like structure that might contain dissolved or entrained heavy metals (Matinde et al., 2018). Metallurgical slags can significantly improve the energy efficiency of the refining and smelting processes. However, they represent a large volume of by-products in metallurgical processes and are therefore disposed of in landfills, which creates long-term environmental problems (Manchisi et al., 2020). Slags are generated from pyrometallurgical activities such as manufacturing iron and steel and production from ferrous and non-ferrous ores. These materials contain significant amounts of alumina and silica, thus making them potential low-cost feedstocks to produce porous aluminosilicate systems (Sayehi et al., 2020b). The iron and steel industry is one of the main contributors to solid waste. The solid waste can either be steel slag or blast furnace (BF) slag, whereby steel slag is derived from the steel-making process and BF slag is derived from an iron-making process (Liu et al., 2018). To date, producing one tonne of molten iron is equivalent to generating 300–1000 kg of blast furnace slag. However, this depends on the furnace's operating conditions and the iron ore grade used (Sayehi et al., 2020b). Blast furnace slags are rich in CaO and MgO (Teir et al., 2007), and this is due to the fluxing agents used during the iron-making process. Blast furnace slags are made up of the ternary SiO_2-Al_2O_3-CaO system and may contain minor metal oxides such as K_2O, MgO, Na_2O, MnO, and Fe_2O_3. Due to the various forms of calcium (Ca-silicates, -oxides, and -carbonate), BFS is usually alkaline (Manchisi et al., 2020). Humad et al. (2019) characterized the chemical compositions of three different blast furnace slags. The major oxides were reported to be MgO, CaO, Al_2O_3, and SiO_2, with the following compositions: 7.8–16.1%, 30.3–38.5%, 11.6–14.3%, and 34–37.9%, respectively.

Steel slag is usually derived from electric arc and basic oxygen furnaces. The composition depends on the type of steel produced (stainless steel or carbon steel) and the feedstock grade used. This implies that steel slag can be classified into electric arc furnace (EAF) slag and basic oxygen furnace (BOF) slag (Manchisi et al., 2020). The feed material to an EAF is steel scrap, which is combined with limited amounts of reduced iron, pig iron, and iron scrap. The EAF uses high-powered graphite electrodes to power the process and smelt the feed material (Jiang et al., 2018). The composition of EAF slag fluctuates significantly and has been reported to be 3–14% (SiO_2), 6–34% (FeO), 3–13% (Al_2O_3), 10–40% (CaO), and 3–13% (MgO) (Manchisi et al., 2020). The mineral phases that have been identified include olivine, wustite, C_3S, C_2S, and merwinite (Jiang et al., 2018). The feed material to a BOF consists of molten iron, steel scraps, and fluxing agents. Pure oxygen is also fed, at supersonic speeds to promote oxidation reactions that smelt the feedstock at high temperatures (1600°C). The slag produced from the process has the following composition: 10–20% (SiO_2), 20–30% (FeO), 1–6%

(Al_2O_3), 40–60% (CaO), and 2–10% (MgO) (Jiang et al., 2018). A summary of compositions of the various types of iron and steel slags is shown in ***Table* 2.3**. Iron and steel slags contain trace elements, which necessitates the application of a pre-treatment process before secondary use for zeolite synthesis.

Table 2.3. Typical chemical compositions of EAF, BOF, and BF slags [adapted from Jiang et al. (2018) and Manchisi et al. (2020)]. (Copyright 2022, with permission from Elsevier).

Industrial Waste	CaO	MgO	SiO_2	Al_2O_3	Fe_2O_3/FeO/Fe	Location
Blast oxygen furnace slag	14.5	6.2	15	4.1	22.5	India
Electric arc furnace slag	30.8	12	23.3	6.1	24.1	India
Blast furnace slag	33.7	14.4	35.1	10.6	0.4	Sweden
Blast oxygen furnace slag	46.7	6.3	14.8	5.5	18.4	China
Electric arc furnace slag	38.8	21.4	29.0	5.9	1.2	India
Blast furnace slag	38.5	8.5	37.5	11.5	0.65	
Blast oxygen furnace slag	38.6	7.7	15.5	5.4	25.5	China
Electric arc furnace slag	16.9	1.86	26.4	4.84	43.4	Malaysia
Blast furnace slag	38.5	9.5	35.5	12.5	≤1	

The chemical compositions of slags derived from the iron and steel industry have shown that these are silica- and alumina-bearing materials that have possible secondary use in zeolite production. For instance, Sugano et al. (2005) used hydrothermal conditioning to convert synthetic blast furnace slag into zeolite A. It was concluded that the high presence of CaO (40%) resulted in the formation of hydrogarnet and tobermorite. However, optimization of the slag composition improved the hydrothermal process to form zeolite A. Kuwahara et al. (2008) experienced the same CaO issue when producing FAU zeolites from steel slag. The amount of CaO in the slag was obtained to be 38.96%, inhibiting zeolite's crystallization. The CaO and other metal oxides (MgO, TiO_2, and Fe_2O_3) were acid-leached using HCl under the following conditions: 5 mol/L and 4 h. Li et al. (2016) used an electric arc furnace slag to synthesize zeolite. The slag had high amounts of Ti (50.9%) and less CaO (5.4%). Instead of leaching out the Ti, the authors converted the silica and alumina into Na_2SiO_3 and $NaAlO_2$ through alkaline fusion under harsh conditions (700°C and 1 h). From there, Na_2SiO_3 and $NaAlO_2$ were water leached from the slag to form a precursor for zeolite production.

2.9.5. Non-ferrous Metallurgical Slags

Non-ferrous metal slags are usually produced as wastes during the extraction of zinc, copper, lithium, cobalt, and nickel from their respective natural ores. The extracted metals are considered non-ferrous and recovered through various mineral processing stages involving comminution, roasting, smelting, and purification processes [electrowinning, leaching] (Piatak et al., 2015). In the smelting step, limestone and iron-bearing materials (iron oxide, iron silicate, or ironstone) are added as fluxes, where fuel for the process is provided in the form of carbon (coal, coke, wood, or charcoal). During the

recovery of non-ferrous metals, secondary wastes are produced that contain insignificant amounts of metals but are rich in silica and alumina (Pribulová et al., 2016). On a global scale, these wastes (non-ferrous metal slag) are landfilled or applied in low-value functions. Therefore, these wastes can be used to produce aluminosilicate material due to their chemical arrangement.

The mineral arrangement and chemical composition of non-ferrous slags are based on the processing conditions and the type of ore involved (Cu-bearing, Ni-bearing, Zn-bearing, or Pb-bearing). However, the main constituents are often arranged in quaternary systems (CaO-SiO_2-Al_2O_3-FeO) or ternary systems (SiO_2-FeO-CaO). Murillo Alarcón et al. (2022) synthesized a model compound of non-ferrous metal slag consisting of both quaternary and ternary systems. The synthetic slags were rich in Fe (66.5%) and were used to formulate crystalline phases of porous inorganic polymers (zeolites). The synthesis process involved mixing surfactant, alkaline activator, and synthetic slag, casting the mixture, and hydrothermally curing it. Van De Sande et al. (2020) optimized the chemical composition of non-ferrous slags for the production of porous inorganic polymers. The optimization was conducted by developing a parallelogram inside a ternary phase diagram (SiO_2-CaO-FeO_x) with boundaries of constant molar ratios.

2.9.6. Waste Foundry Sand (WFS)

Foundry sand is a moulding material that is applied in the non-ferrous and ferrous metal casting industry. The material is reclaimed and recycled for further metal casting applications until it is unusable. At this point, the material contains hazardous compounds in the form of heavy metals and other pollutants, and it is regarded as WFS, which is landfilled after solidification and stabilization (Sayehi et al., 2020b). The USA and India are reported to produce 9.71 million tons of WFS per annum, which is rich in silica (85–95%) and minor traces of Al_2O_3, TiO_2, Cr_2O_3, and alkali earth oxides. Based on the chemical makeup, WFS can be applied as a competent starting material for zeolite synthesis and reduce its impact on the environment (Aslani et al., 2021). Various foundry sand wastes were investigated for the synthesis of analcime-type zeolite (Vigil de la Villa Mencía et al., 2020). The wastes were hydrothermally treated at the following conditions: 10 M (NaOH solution), 225°C for 2 h. The mineral composition of the wastes included quartz and feldspar.

2.9.7. Bauxite Residue

The Bayer process is the most widely used process for the production of aluminium oxide through the use of bauxite ore. The mineralogical makeup of the bauxite ore includes aluminium hydroxide phases such as gibbsite, diaspore, and boehmite with a high grade of crystalline alumina [30-60%] (Verma et al., 2017). During the processing of bauxite ores, large volumes of bauxite residue are subsequently released at a global rate of 150 million tonnes per annum (Ujaczki et al., 2018). Bauxite ore, also referred to as red mud, appears reddish in colour due to the high content of Fe_2O_3. Therefore, the removal of Fe_2O_3 is necessary so as to increase the silica-to-alumina ratio and improve aluminium oxide recovery (Liu yin Xia et al., 2010). This is usually achieved through the bauxite flotation process; however, this results in the formation of secondary waste [bauxite tailings] (Xia et al., 2009). The chemical and mineralogical content of bauxite residues (tailings) are dependent on the processing technique; however, the major compounds include Fe_2O_3, TiO_2, Al_2O_3, SiO_2 and Na_2O with minor trace elements such as Mn, Pb, Zn, Co, Cr, and As (Verma et al., 2017). Ma et al. (2014) used bauxite tailings from a flotation process for the synthesis of zeolite 4A. The synthesis stages involved wet -

chemistry and alkaline fusion to remove impurities and prepare the feed material. This was followed by crystallization to produce porous zeolite 4A. In comparison to commercially available zeolite, the synthesized zeolite 4A showed improved ion exchange capacity.

2.10. Microwave-assisted Pyrolysis

Microwave-assisted pyrolysis of biomass is a cutting-edge method in the field of renewable energy. This process utilizes microwave radiation to efficiently break down biomass into valuable products such as bio-oil, biochar, and syngas. By applying controlled levels of microwave energy, the pyrolysis reaction is accelerated, resulting in higher yields and shorter reaction times compared to conventional pyrolysis techniques (Morgan et al., 2017a). This innovative technique offers a sustainable solution for biomass waste management and presents opportunities to produce biofuels and other valuable chemicals. The ability to tailor the reaction conditions and optimize the process parameters makes microwave-assisted pyrolysis a promising avenue for future research and industrial applications.

Microwave-assisted pyrolysis of biomass serves as a pioneering technique within the realm of renewable energy studies. This advanced method capitalizes on the properties of microwave radiation, using it with finesse to deconstruct biomass efficiently into beneficial products, which include bio-oil, biochar, and syngas. Introducing calibrated levels of microwave energy effectively accelerates the pyrolysis reaction, thereby offering superior yields and minimizing reaction times when compared with conventional pyrolysis methodologies (Arpia et al., 2021). This novel modus operandi not only puts forward a sustainable strategy for managing biomass waste but also delineates potential avenues for generating biofuels and an array of valuable chemicals. This process's amenability to manipulating reaction conditions and fine-tuning operational parameters deems microwave-assisted pyrolysis a promising trajectory for future scientific research and industrial implementations.

2.10.1. Microwave Theory

The microwave technology that is currently being used by researchers is often laboratory scale, consisting of an electromagnetic radiation generator (magnetron) that emits frequencies between 0.3 and 30 GHz, corresponding to 1 to 0.01 nm, respectively. Microwave irradiation operates through two mechanisms: ionic conduction and dipole rotation (Zeng et al., 2021). For both mechanisms, an alternating electric/magnetic field is transmitted, and it penetrates the feed sample. For the latter mechanism, the dipole molecules in the feed sample will rotate in synchrony to align themselves with the electric field. Heat is generated during this rotation, and the temperature of the feed sample will rise. In the former mechanism, metal ions oscillate and collide against each other, thereby transferring heat through conduction (Morgan et al., 2017a). The ability of a feed sample to absorb microwave energy is a function of the material's loss tangent (dielectric heating) and is expressed at a given temperature and frequency. It is through this variable (loss tangent) that researchers have investigated microwave irradiation as a heating source for the hydrothermal synthesis method.

When compared to conventional heating, microwave irradiation has proven to be more efficient due to its heating mechanisms. In conventional heating, energy is transferred from the outer layers of the feed sample toward the interior ***Figure 2.6***. Meanwhile, microwave heating occurs in the opposite direction (inward to outward). As a result, heating is more uniform, resulting in uniformity of the catalyst crystalline structure, range of Si/Al ratios, and increased crystallization rates. Zeng et al. (2021) reviewed various microwave synthesis methods to produce zeolites. The morphology of the

zeolite was attributed to the microwave irradiation time (343–463K), and the size (0.01–10 μm) and structure (rod-like, spherical, pucklike, wormlike, etc.) of the crystals were attributed to the irradiation power. The current study varied the aforementioned parameters, in order to control the structural properties of the synthesized zeolite-based catalysts.

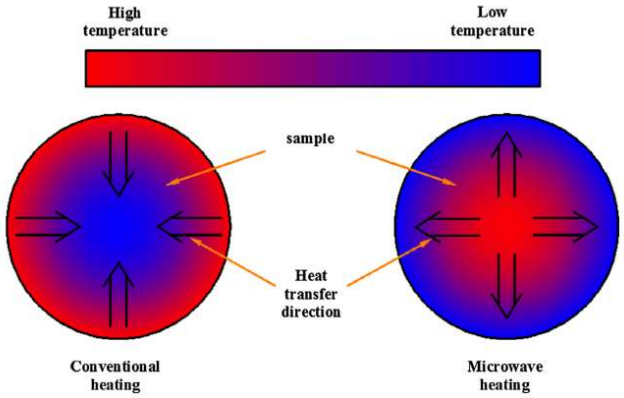

Figure 2.6. Comparison between conventional and microwave heating [adapted from Morgan et al. (2017)]. (Copyright 2022, with permission from Elsevier).

2.11. Conclusion

The research results discussed in this review highlight how catalytic pyrolysis stands out as a preferred approach for generating energy from biomass. Catalytic pyrolysis can efficiently convert waste materials into valuable fuels and bioenergy, utilizing catalysts to facilitate and enhance the transformation. The utilization of such a method not only contributes to the production of alternative energy sources but also plays a pivotal role in managing and reducing waste, thereby presenting a sustainable solution to energy production challenges. This approach, by virtue of its efficiency and environmental benefits, underscores the importance of ongoing research and development in the field of renewable energy technologies. The findings related to the chemical and mineralogical composition and generation of aluminosilicate-containing industrial wastes have shown promising and beneficial secondary use of these wastes for zeolite production. Literature surveys have demonstrated the significant environmental impact of these wastes and the need for sustainable recycling and waste management techniques. Therefore, researchers have systematically investigated the potential usage of industrial waste for zeolite production. Synthesizing zeolites from industrial waste will reduce landfill disposals and promote a closed-loop waste economy. The waste resources have shown the potential to develop porous materials (zeolites) that can be used as catalysts, adsorbents, and molecular sieves and are sustainable, efficient, robust, and environmentally friendly. In addition, advances in the zeolite synthesis approaches (top-down and bottom-up) have been reported. Recently, these approaches have been enhanced to meet the standards of a green economy. This has involved the use of low-cost waste resources, solvent-free synthesis methods, and green templates. Subsequently, this has enabled researchers to modify the physicochemical and structural properties of zeolites to fit process requirements. This can, in turn, increase the applicability of zeolites in sectors such as CO_2 capture, water purification, energy storage, and fuel cells. However, further evaluations of the economic impact of these methods are needed to justify commercialization and wide scientific acceptance.

References

Ahmed, M. H. M., Batalha, N., Mahmudul, H. M. D., Perkins, G., & Konarova, M. (2020). A review on advanced catalytic co-pyrolysis of biomass and hydrogen-rich feedstock: Insights into synergistic effect, catalyst development and reaction mechanism. *Bioresource Technology*, *310*, 123457. https://doi.org/10.1016/j.biortech.2020.123457

Alaba, P. A., Sani, Y. M., & Daud, W. M. A. W. (2015). Synthesis and characterization of hierarchical nanoporous HY zeolites from acid-activated kaolin. *Cuihua Xuebao/Chinese Journal of Catalysis*, *36*(11), 1846–1851. https://doi.org/10.1016/S1872-2067(15)60962-7

Alves, J. A. B. L., Dantas, E. R. S., Pergher, S. B. C., Melo, D. M. A., & Melo, M. A. F. (2014). Synthesis of high value-added zeolitic materials using glass powder residue as a silica source. *Materials Research*, *17*(1), 213–218. https://doi.org/10.1590/S1516-14392013005000191

Ameh, A. E., Eze, C. P., Antunes, E., Cornelius, M. L. U., Musyoka, N. M., & Petrik, L. F. (2020). Stability of fly ash-based BEA-zeolite in hot liquid phase. *Catalysis Today*, *357*, 416–424. https://doi.org/10.1016/J.CATTOD.2019.08.006

Anuar Sharuddin, S. D., Abnisa, F., Wan Daud, W. M. A., & Aroua, M. K. (2016). A review on pyrolysis of plastic wastes. *Energy Conversion and Management*, *115*, 308–326. https://doi.org/10.1016/j.enconman.2016.02.037

Arpia, A. A., Chen, W. H., Lam, S. S., Rousset, P., & de Luna, M. D. G. (2021). Sustainable biofuel and bioenergy production from biomass waste residues using microwave-assisted heating: A comprehensive review. *Chemical Engineering Journal*, *403*, 126–233. https://doi.org/10.1016/j.cej.2020.126233

Aslani, M., Akbardoost, J., & Delnavaz, M. (2021). Investigating the effect of the foundry sand and waste foundry sand on the fracture toughness of concrete. *Arabian Journal of Geosciences*, *14*(464), 1–10. https://doi.org/10.1007/s12517-021-06852-7

Ayeni, A. O., & Daramola, M. O. (2017). Lignocellulosic biomass waste beneficiation: Evaluation of oxidative and non-oxidative pretreatment methodologies of South African corn cob. *Journal of Environmental Chemical Engineering*, *5*(2), 1771–1779. https://doi.org/10.1016/j.jece.2017.03.019

Baetge, S., & Kaltschmitt, M. (2018). Rice straw and rice husks as energy sources—comparison of direct combustion and biogas production. *Biomass Conversion and Biorefinery*, *8*(3), 719–737. https://doi.org/10.1007/S13399-018-0321-Y/FIGURES/12

Barrer, R. M., & Makki, M. B. (1964). MOLECULAR SIEVE SORBENTS FROM CLINOPTILOLITE. *Canadian Journal of Chemistry*, *42*(6), 1481–1487. https://doi.org/10.1139/v64-223

Beck, J. S., Vartuli, J. C., Roth, W. J., Leonowicz, M. E., Kresge, C. T., Schmitt, K. D., Chu, C. T. W., Olson, D. H., Sheppard, E. W., McCullen, S. B., Higgins, J. B., & Schlenker, J. L. (1992). A New Family of Mesoporous Molecular Sieves Prepared with Liquid Crystal Templates.

Journal of the American Chemical Society, *114*(27), 10834–10843. https://doi.org/10.1021/JA00053A020/ASSET/JA00053A020.FP.PNG_V03

Belviso, C., Cavalcante, F., Niceforo, G., & Lettino, A. (2017). Sodalite, faujasite and A-type zeolite from 2:1dioctahedral and 2:1:1 trioctahedral clay minerals. A singular review of synthesis methods through laboratory trials at a low incubation temperature. *Powder Technology*, *320*, 483–497. https://doi.org/10.1016/J.POWTEC.2017.07.039

Bieseki, L., Penha, F. G., & Pergher, S. B. C. (2013). Zeolite a synthesis employing a brazilian coal ash as the silicon and aluminum source and its applications in adsorption and pigment formulation. *Materials Research*, *16*(1), 38–43. https://doi.org/10.1590/S1516-14392012005000144

Bohra, S., Kundu, D., & Naskar, M. K. (2014). One-pot synthesis of NaA and NaP zeolite powders using agro-waste material and other low cost organic-free precursors. *Ceramics International*, *40*, 1229–1234. https://doi.org/10.1016/j.ceramint.2013.06.001

Bouanga Boudiombo, J. S., Madden, D. G., Cusack, B., Cronin, P., & Ryan, A. (2023). State of the art and prospects of zeolites and metal organic frameworks (MOFs) for nitrogen and phosphorus removal in dairy wastewater. *Chemosphere*, *329*, 138531. https://doi.org/10.1016/J.CHEMOSPHERE.2023.138531

Bukhari, S. S., Behin, J., Kazemian, H., & Rohani, S. (2015). Conversion of coal fly ash to zeolite utilizing microwave and ultrasound energies: A review. *Fuel*, *140*, 250–266. https://doi.org/10.1016/j.fuel.2014.09.077

Cao, S., Tao, F., Tang, Y., Li, Y., & Yu, J. (2016). Size- and shape-dependent catalytic performances of oxidation and reduction reactions on nanocatalysts [10.1039/C6CS00094K. *Chemical Society Reviews*, *45*(17), 4747–4765. https://doi.org/10.1039/C6CS00094K

Chaihad, N., Situmorang, Y. A., Anniwaer, A., Kurnia, I., Karnjanakom, S., Kasai, Y., Abudula, A., Reubroycharoen, P., & Guan, G. (2021). Preparation of various hierarchical HZSM-5 based catalysts for in-situ fast upgrading of bio-oil. *Renewable Energy*, *169*, 283–292. https://doi.org/10.1016/j.renene.2021.01.013

Chehreh Chelgani, S. (2019). Exploring relationships of gross calorific value and valuable elements with conventional coal properties for North Korean coals. *International Journal of Mining Science and Technology*, *29*(6), 867–871. https://doi.org/10.1016/j.ijmst.2019.09.005

Chen, H., Wydra, J., Zhang, X., Lee, P. S., Wang, Z., Fan, W., & Tsapatsis, M. (2011). Hydrothermal synthesis of zeolites with three-dimensionally ordered mesoporous-imprinted structure. *Journal of the American Chemical Society*, *133*(32), 12390–12393. https://doi.org/10.1021/ja2046815

Chen, J., Lim, B., Lee, E. P., & Xia, Y. (2009). Shape-controlled synthesis of platinum nanocrystals for catalytic and electrocatalytic applications. *Nano Today*, *4*(1), 81–95. https://doi.org/10.1016/j.nantod.2008.09.002

Chen, L. H. (2020). Hierarchically porous materials and green carbon science-An interview with Ming-Yuan He. *National Science Review*, *7*(11), 1759–1761. https://doi.org/10.1093/nsr/nwaa131

Chen, L.-H., Li, X.-Y., Rooke, J. C., Zhang, Y.-H., Yang, X.-Y., Tang, Y., Xiao, F.-S., & Su, B.-L. (2012). Hierarchically structured zeolites: synthesis, mass transport properties and applications [10.1039/C2JM31957H. *Journal of Materials Chemistry*, *22*(34), 17381–17403. https://doi.org/10.1039/C2JM31957H

Chiang, Y. W., Ghyselbrecht, K., Santos, R. M., Meesschaert, B., & Martens, J. A. (2012). Synthesis of zeolitic-type adsorbent material from municipal solid waste incinerator bottom ash and its application in heavy metal adsorption. *Catalysis Today*, *190*(1), 23–30. https://doi.org/10.1016/j.cattod.2011.11.002

Cho, H. S., & Ryoo, R. (2012). Synthesis of ordered mesoporous MFI zeolite using CMK carbon templates. *Microporous and Mesoporous Materials*, *151*, 107–112. https://doi.org/10.1016/j.micromeso.2011.11.007

Choi, M., Cho, H. S., Srivastava, R., Venkatesan, C., Choi, D. H., & Ryoo, R. (2006). Amphiphilic organosilane-directed synthesis of crystalline zeolite with tunable mesoporosity. *Nature Materials*, *5*(9), 718–723. https://doi.org/10.1038/nmat1705

Choi, M., Na, K., Kim, J., Sakamoto, Y., Terasaki, O., & Ryoo, R. (2009). Stable single-unit-cell nanosheets of zeolite MFI as active and long-lived catalysts. *Nature*, *461*(7261), 246–249. https://doi.org/10.1038/nature08288

Christensen, C. H., Schmidt, I., Carlsson, A., Johannsen, K., & Herbst, K. (2005). Crystals in crystals-nanocrystals within mesoporous zeolite single crystals. *Journal of the American Chemical Society*, *127*(22), 8098–8102. https://doi.org/10.1021/ja050380u

Cleveland, C. L., Landman, U., Schaaff, T. G., Shafigullin, M. N., Stephens, P. W., & Whetten, R. L. (2015). Structural Evolution of Smaller Gold Nanocrystals: The Truncated Decahedral Motif. *Physical Review Letters*, *79*(10), 1873–1876. https://doi.org/10.1103/PhysRevLett.79.1873

Corma, A. (1997). From Microporous to Mesoporous Molecular Sieve Materials and Their Use in Catalysis. *Chemical Reviews*, *93*, 2373–2420. https://doi.org/https://doi.org/10.1021/cr960406n

Corma, A., Fornés, V., Fornés, F., Martínez-Triguero, J., & Pergher, S. B. (1999). Delaminated Zeolites: Combining the Benefits of Zeolites and Mesoporous Materials for Catalytic Uses. *Journal of Catalysis*, *186*, 57–63. http://www.idealibrary.comon

Cornelius, M.-L. U. (2019). Synthesis and characterisation of high silica zeolites with MOR and MFI framework type from South African coal fly ash. University of the Western Cape, Cape Town, South Africa, Available at: http://etd.uwc.ac.za/iihttp://etd.uwc.ac.za/ (Accessed: 21 November 2022).

Dai, G., Wang, G., Wang, K., Zhou, Z., & Wang, S. (2021). Mechanism study of hemicellulose pyrolysis by combining in-situ DRIFT, TGA-PIMS and theoretical calculation. *Proceedings of the Combustion Institute*, *38*(3), 4241–4249. https://doi.org/10.1016/j.proci.2020.06.196

Demirbaş, A. (2001). Biomass resource facilities and biomass conversion processing for fuels and chemicals. *Energy Conversion and Management*, *42*(11), 1357–1378. https://doi.org/10.1016/S0196-8904(00)00137-0

Deng, L., Xu, Q., & Wu, H. (2016). Synthesis of Zeolite-like Material by Hydrothermal and Fusion Methods Using Municipal Solid Waste Fly Ash. *Procedia Environmental Sciences*, *31*, 662–667. https://doi.org/10.1016/j.proenv.2016.02.122

Dessau, R. M., Valyocsik, E. W., & Goeke, N. H. (1992). Aluminum zoning in ZSM-5 as revealed by selective silica removal. *Zeolites*, *12*(7), 776–779. https://doi.org/10.1016/0144-2449(92)90049-U

Duan, W., Wu, Q., Li, P., & Cheng, P. (2022). Techno-economic analysis of a novel full-chain blast furnace slag utilization system. *Energy*, *242*, 123049. https://doi.org/10.1016/j.energy.2021.123049

Elinwa, A. U., & Ejeh, S. P. (2004). Effects of the Incorporation of Sawdust Waste Incineration Fly Ash in Cement Pastes and Mortars. *Journal of Asian Architecture and Building Engineering*, *3*(1), 1–7. https://doi.org/10.3130/jaabe.3.1

Faizul, C. P., Abdullah, C., & Fazlul, B. (2013). Review of extraction of silica from agricultural wastes using acid leaching treatment. *Advanced Materials Research*, *626*, 997–1000. https://doi.org/10.4028/WWW.SCIENTIFIC.NET/AMR.626.997

Fang, Y., Hu, H., & Chen, G. (2008). Zeolite with tunable intracrystal mesoporosity synthesized with carbon aerogel as a secondary template. *Microporous and Mesoporous Materials*, *113*(1), 481–489. https://doi.org/10.1016/j.micromeso.2007.12.006

Farkaš, A.,Rožić M.and Barbarić-Mikoćević, ž. (2005). Innovations in hierarchical zeolite synthesis. *Journal of Hazardous Materials*, *264*(B117), 25–33. https://doi.org/10.1016/j.cattod.2015.08.012

Fatih Demirbas, M., Balat, M., & Balat, H. (2011). Biowastes-to-biofuels. *Energy Conversion and Management*, *52*(4), 1815–1828. https://doi.org/10.1016/j.enconman.2010.10.041

Feliczak-Guzik, A. (2018). Hierarchical zeolites: Synthesis and catalytic properties. *Microporous and Mesoporous Materials*, *259*, 33–45. https://doi.org/10.1016/j.micromeso.2017.09.030

Feng, X., Jiang, G., Zhao, Z., Wang, L., Li, X., Duan, A., Liu, J., Xu, C., & Gao, J. (2010). Highly effective F-modified HZSM-5 catalysts for the cracking of naphtha to produce light olefins. *Energy & Fuels*, *24*(8), 4111–4115.

Firmansyah, M. L., Jalil, A. A., Triwahyono, S., Hamdan, H., Salleh, M. M., Ahmad, W. F. W., & Kadja, G. T. M. (2016). Synthesis and characterization of fibrous silica ZSM-5 for cumene hydrocracking [10.1039/C6CY00106H. *Catalysis Science & Technology*, *6*(13), 5178–5182. https://doi.org/10.1039/C6CY00106H

Fortune Business Insights. (2025). *Zeolite Market Size, Share & Growth | Global Report [2032]*. Metals & Minerals. https://www.fortunebusinessinsights.com/industry-reports/zeolite-market-101921 (Accessed: 02 March 2025).

Fu, T., Zhou, H., & Li, Z. (2016). Effect of Particle Morphology for ZSM-5 Zeolite on the Catalytic Conversion of Methanol to Gasoline-Range Hydrocarbons. *Catalysis Letters*, *146*(10), 1973–1983. https://doi.org/10.1007/s10562-016-1841-3

Furumoto, Y., Harada, Y., Tsunoji, N., Takahashi, A., Fujitani, T., Ide, Y., Sadakane, M., & Sano, T. (2011). Effect of acidity of ZSM-5 zeolite on conversion of ethanol to propylene. *Applied Catalysis A: General*, *399*(1–2), 262–267.

García-Martínez, J., Johnson, M., Valla, J., Li, K., & Ying, J. Y. (2012). Mesostructured zeolite y - High hydrothermal stability and superior FCC catalytic performance. *Catalysis Science and Technology*, *2*, 987–994. https://doi.org/10.1039/c2cy00309k

Garcia-Martinez, J., Xiao, C., Cychosz, K. A., Li, K., Wan, W., Zou, X., & Thommes, M. (2014). Evidence of Intracrystalline Mesostructured Porosity in Zeolites by Advanced Gas Sorption. *Electron Tomography and Rotation Electron Diffraction. ChemCatChem*, *6*(11), 3110–3115. https://doi.org/10.1002/cctc.201402499

Gebbink, B. K. (2017a). *Zeolites in Catalysis Series Editors :* https://doi.org/10.1039

Ghorbanpour, A., Gumidyala, A., Grabow, L. C., Crossley, S. P., & Rimer, J. D. (2015). Epitaxial growth of ZSM-5@ Silicalite-1: A core–shell zeolite designed with passivated surface acidity. *Acs Nano*, *9*(4), 4006–4016.

Guo, H., Ge, T., Lv, J., Du, C., Zhou, J., Liu, Z., & Hua, Z. (2019). Mesoporogen-Free Synthesis of High-Silica Hierarchically Structured ZSM-5 Zeolites and their Superior Performance for the Methanol-to-Propylene Reaction. *European Journal of Inorganic Chemistry*, 51–58. https://doi.org/10.1002/ejic.201800926

Guo, Y., Yan, K., Cui, L., & Cheng, F. (2016). Improved extraction of alumina from coal gangue by surface mechanically grinding modification. *Powder Technology*, *302*, 33–41. https://doi.org/10.1016/j.powtec.2016.08.034

Hagen, J. (2005). *Industrial Catalysis: A Practical Approach* (2nd ed.). WILEY-VCH Verlag GmbH & Co.

Haiying, Z., Youcai, Z., & Jingyu, Q. (2010). Characterization of heavy metals in fly ash from municipal solid waste incinerators in Shanghai. *Process Safety and Environmental Protection*, *88*(2), 114–124. https://doi.org/10.1016/j.psep.2010.01.001

Han, J., Jiang, G., Han, S., Liu, J., Zhang, Y., Liu, Y., Wang, R., Zhao, Z., Xu, C., Wang, Y., Duan, A., Liu, J., & Wei, Y. (2016). The Fabrication of Ga2O3/ZSM-5 Hollow Fibers for Efficient Catalytic Conversion of n-Butane into Light Olefins and Aromatics. *Catalysts*, *6*(1), 13. https://doi.org/https://www.mdpi.com/2073-4344/6/1/13

Hodoshima, S., Motomiya, A., Wakamatsu, S., Kanai, R., & Yagi, F. (2016). Catalytic conversion of light hydrocarbons to propylene over MFI-zeolite/metal-oxide composites. *Microporous and Mesoporous Materials*, *233*, 125–132.

Humad, A. M., Habermehl-Cwirzen, K., & Cwirzen, A. (2019). Effects of fineness and chemical composition of blast furnace slag on properties of Alkali-Activated Binder. *Materials*, *12*(20), 1–16. https://doi.org/10.3390/ma12203447

Huo, Q. S., Margolese, D. I., Ciesla, U., Feng, P. Y., Gier, T. E., Sieger, P., Leon, R., Petroff, P. M., & Schuth, F. (1994). Generalized synthesis of periodic surfactant/inorganic composite materials. *Nature*, *368*(6469), 317. https://www.proquest.com/docview/204472087/abstract/78FD95271E2F4454PQ/1?accountid=15083&sourcetype=Scholarly%20Journals

Inagaki, S., Sato, K., Hayashi, S., Tatami, J., Kubota, Y., & Wakihara, T. (2015). Mechanochemical approach for selective deactivation of external surface acidity of ZSM-5 zeolite catalyst. *ACS Applied Materials & Interfaces*, *7*(8), 4488–4493.

Inayat, A., Knoke, I., Spiecker, E., & Schwieger, W. (2012). Assemblies of mesoporous FAU-type zeolite nanosheets. *Angewandte Chemie - International Edition*, *51*(8), 1962–1965. https://doi.org/10.1002/anie.201105738

Ivanova, I. I., Kasyanov, I. A., Maerle, A. A., & Zaikovskii, V. I. (2014). Mechanistic study of zeolites recrystallization into micro-mesoporous materials. *Microporous and Mesoporous Materials*, *189*, 163–172. https://doi.org/10.1016/j.micromeso.2013.11.001

Jacobsen, C. J. H., Madsen, C., Houzvicka, J., Schmidt, I., & Carlsson, A. (2000). Mesoporous Zeolite Single Crystals. *Journal of the American Chemical Society*, *122*(29), 7116–7117. https://doi.org/10.1021/ja000744c

Jendrlin, M., Grand, J., Lakiss, L., Bazin, P., Mintova, S., & Zholobenko, V. (2023). Environmental Applications of Zeolites: Preparation and Screening of Cu-Modified Zeolites as Potential CO Sensors. *Chemistry*, *5*(1), 314–333. https://doi.org/10.3390/chemistry5010024

Jendrlin, M., Grand, J., Lakiss, L., Bazin, P., Mintova, S., & Zholobenko, V. (2023). Environmental Applications of Zeolites: Preparation and Screening of Cu-Modified Zeolites as Potential CO Sensors. *Chemistry*, *5*(1), 314–333. https://doi.org/10.3390/chemistry5010024

Ji, Y., Shi, B., Yang, H., & Yan, W. (2017a). Synthesis of isomorphous MFI nanosheet zeolites for supercritical catalytic cracking of n-dodecane. *Applied Catalysis A: General*, *533*, 90–98.

Ji, Y., Yang, H., & Yan, W. (2017b). Strategies to enhance the catalytic performance of ZSM-5 zeolite in hydrocarbon cracking: A review. *Catalysts*, *7*(12). https://doi.org/10.3390/CATAL7120367

Jiang, L., Luo, J., Xu, F., Qian, L., Wang, Y., Li, H., & Fang, Z. (2022). High yield production of levoglucosan via catalytic pyrolysis of cellulose at low temperature. *Fuel*, *323*. https://doi.org/10.1016/j.fuel.2022.124369

Jiang, Y., Ling, T. C., Shi, C., & Pan, S. Y. (2018). Characteristics of steel slags and their use in cement and concrete—A review. *Resources, Conservation and Recycling*, *136*, 187–197. https://doi.org/10.1016/j.resconrec.2018.04.023

Johnson, E. B. G., & Arshad, S. E. (2014). Hydrothermally synthesized zeolites based on kaolinite: A review. *Applied Clay Science*, *97–98*, 215–221. https://doi.org/10.1016/j.clay.2014.06.005

Jung, J. S., Kim, T. J., & Seo, G. (2004). Catalytic cracking of n-octane over zeolites with different pore structures and acidities. *Korean Journal of Chemical Engineering*, *21*(4), 777–781.

Kadja, G. T. M., Mukti, R. R., Liu, Z., Rilyanti, M., Ismunandar, Marsih, I. N., Ogura, M., Wakihara, T., & Okubo, T. (2016). Mesoporogen-free synthesis of hierarchically porous ZSM-5 below 100°C. *Microporous and Mesoporous Materials*, *226*, 344–352. https://doi.org/10.1016/j.micromeso.2016.02.007

Khaleque, A., Alam, M. M., Hoque, M., Mondal, S., Haider, J. Bin, Xu, B., Johir, M. A. H., Karmakar, A. K., Zhou, J. L., Ahmed, M. B., & Moni, M. A. (2020). Zeolite synthesis from low-cost materials and environmental applications: A review. *Environmental Advances*, *2*(August), 100019. https://doi.org/10.1016/j.envadv.2020.100019

Kim, J., Kim, W., Seo, Y., Kim, J.-C., & Ryoo, R. (2013). n-Heptane hydroisomerization over Pt/MFI zeolite nanosheets: Effects of zeolite crystal thickness and platinum location. *Journal of Catalysis*, *301*, 187–197.

Koohsaryan, E., & Anbia, M. (2016). Nanosized and hierarchical zeolites: A short review. *Chinese Journal of Catalysis*, *37*(4), 447–467. https://doi.org/10.1016/S1872-2067(15)61038-5

Kubo, K., Iida, H., Namba, S., & Igarashi, A. (2018). Selective Formation of Light Olefins by Catalytic Cracking of Naphtha Components over ZSM-5 Zeolite Catalysts. *Journal of the Japan Petroleum Institute*, *61*(1), 10–19. https://doi.org/10.1627/JPI.61.10

Kumar, R., Strezov, V., Weldekidan, H., He, J., Singh, S., Kan, T., & Dastjerdi, B. (2020). Lignocellulose biomass pyrolysis for bio-oil production: A review of biomass pre-treatment methods for production of drop-in fuels. *Renewable and Sustainable Energy Reviews*, *123*, 109763. https://doi.org/10.1016/j.rser.2020.109763

Kumba Iron Ore. (2011). *THE SOUTH AFRICAN IRON AND STEEL VALUE CHAIN*. *Anglo American,* 1–45.

Kustova, M., Egeblad, K., Christensen, C. H., Kustov, A. L., & Christensen, C. H. (2010). Hierarchical zeolites: progress on synthesis and characterization of mesoporous zeolite single crystal catalysts. In R. Xu, Z. Gao, J. Chen, & W. Yan (Eds.), *Studies in Surface Science and Catalysis* (Vol. 170, pp. 267–275). Elsevier. https://doi.org/10.1016/S0167-2991(07)80848-2

Kuwahara, Y., Ohmichi, T., Mori, K., Katayama, I., & Yamashita, H. (2008). Synthesis of zeolite from steel slag and its application as a support of nano-sized TiO2 photocatalyst. *Journal of Materials Science*, *43*(7), 2407–2410. https://doi.org/10.1007/s10853-007-2073-0

Le Van Mao, R., Le, T., Fairbairn, M., Muntasar, A., Xiao, S., & Denes, G. (1999). ZSM-5 zeolite with enhanced acidic properties. *Applied Catalysis A: General*, *185*(1), 41–52.

Li, C., Li, X., Yu, Y., Zhang, Q., Li, L., Zhong, H., & Wang, S. (2022). A novel conversion for blast furnace slag (BFS) to the synthesis of hydroxyapatite-zeolite material and its evaluation of adsorption properties. *Journal of Industrial and Engineering Chemistry*, *105*, 63–73. https://doi.org/10.1016/j.jiec.2021.08.017

Li, Y., Li, L., & Yu, J. (2017). Applications of Zeolites in Sustainable Chemistry. *Chem*, *3*, 928–949. https://doi.org/10.1016/j.chempr.2017.10.009

Li, Y., Peng, T., Man, W., Ju, L., Zheng, F., Zhang, M., & Guo, M. (2016). Hydrothermal synthesis of mixtures of NaA zeolite and sodalite from Ti-bearing electric arc furnace slag. *RSC Advances*, *6*(10), 8358–8366. https://doi.org/10.1039/c5ra26881h

Lin, L. F., Zhao, S. F., Zhang, D. W., Fan, H., Liu, Y. M., & He, M. Y. (2015). Acid strength controlled reaction pathways for the catalytic cracking of 1-pentene to propene over ZSM-5. *ACS Catalysis*, *5*(7), 4048–4059.

Lin, Y. C., Cho, J., Tompsett, G. A., Westmoreland, P. R., & Huber, G. W. (2009). Kinetics and mechanism of cellulose pyrolysis. *Journal of Physical Chemistry C*, *113*(46), 20097–20107. https://doi.org/10.1021/jp906702p

Liu, J., Jiang, G., Liu, Y., Di, J., Wang, Y., Zhao, Z., Sun, Q., Xu, C., Gao, J., Duan, A., Liu, J., Wei, Y., Zhao, Y., & Jiang, L. (2014). Hierarchical Macro-meso-microporous ZSM-5 Zeolite Hollow Fibers With Highly Efficient Catalytic Cracking Capability. *Scientific Reports*, *4*(1), 7276. https://doi.org/10.1038/srep07276

Liu, Q., Liu, W., Hu, J., Wang, L., Gao, J., Liang, B., Yue, H., Zhang, G., Luo, D., & Li, C. (2018). Energy-efficient mineral carbonation of blast furnace slag with high value-added products. *Journal of Cleaner Production*, *197*, 242–252. https://doi.org/10.1016/j.jclepro.2018.06.150

Liu, S., Zhang, Y., Fan, L., Zhou, N., Tian, G., Zhu, X., Cheng, Y., Wang, Y., Liu, Y., Chen, P., & Ruan, R. (2017). Bio-oil production from sequential two-step catalytic fast microwave-assisted biomass pyrolysis. *Fuel*, *196*, 261–268. https://doi.org/10.1016/j.fuel.2017.01.116

Lounis, Z., & Belarbi, H. (2018). *The Nanostructure Zeolites MFI-Type ZSM5*. In. https://doi.org/10.5772/intechopen.77020

Lu, X., & Gu, X. (2022). A review on lignin pyrolysis: pyrolytic behavior, mechanism, and relevant upgrading for improving process efficiency. In *Biotechnology for Biofuels and Bioproducts* (Vol. 15, Issue 1). BioMed Central Ltd. https://doi.org/10.1186/s13068-022-02203-0

Lu, X., Peng, Y., Wang, Z., & Yan, Y. (2015). Rapid fabrication of highly b-oriented zeolite MFI thin films using ammonium salts as crystallization-mediating agents. *Chemical Communications*, *51*(55), 11076–11079.

Luo, W., Yang, X., Wang, Z., Huang, W., Chen, J., Jiang, W., Wang, L., Cheng, X., Deng, Y., & Zhao, D. (2017). Synthesis of ZSM-5 aggregates made of zeolite nanocrystals through a simple solvent-free method. *Microporous and Mesoporous Materials*, *243*, 112–118. https://doi.org/10.1016/j.micromeso.2017.01.040

Lupi, J., Kelly, M., O'Shea, A., Ghaani, M. R., & Dooley, S. (2023). *Quantum Chemical Modelling of Hemicellulose Fast Pyrolysis: β-D-xylopyranose as a Structural Motif*. https://doi.org/10.26434/CHEMRXIV-2023-X92BW

Ma, D., Wang, Z., Guo, M., Zhang, M., & Liu, J. (2014). Feasible conversion of solid waste bauxite tailings into highly crystalline 4A zeolite with valuable application. *Waste Management*, *34*(11), 2365–2372. https://doi.org/10.1016/j.wasman.2014.07.012

Maatoug, N., Delahay, G., & Tounsi, H. (2018). Valorization of vitreous China waste to EMT/FAU, FAU and Na-P zeotype materials. *Waste Management*, *74*, 267–278. https://doi.org/10.1016/J.WASMAN.2017.12.014

Madsen, C., & Jacobsen, C. J. H. (1999). Nanosized zeolite crystals-convenient control of crystal size distribution by confined space synthesis. *Chemical Communications*, 673–674.

Maghfirah, A., Ilmi, M. M., Fajar, A. T. N., & Kadja, G. T. M. (2020). A review on the green synthesis of hierarchically porous zeolite. *Materials Today Chemistry*, *17*, 100348. https://doi.org/10.1016/j.mtchem.2020.100348

Manchisi, J., Matinde, E., Rowson, N. A., Simmons, M. J. H., Simate, G. S., Ndlovu, S., & Mwewa, B. (2020). Ironmaking and Steelmaking Slags As Sustainable Adsorbents For Industrial Effluents And Wastewater Treatment: A critical review of properties, performance, challenges and opportunities. *Sustainability (Switzerland)*, *12*(5), 1–47. https://doi.org/10.3390/su12052118

Mangialardi, T. (2003). Disposal of MSWI fly ash through a combined washing-immobilisation process. *Journal of Hazardous Materials*, *98*(1–3), 225–240. https://doi.org/10.1016/S0304-3894(02)00359-X

MarketsandMarkets. (2018). Synthetic Zeolites Market by Type & Application - Global Forecast 2023 | MarketsandMarkets. *Synthetic Zeolite Market*. Available at: https://www.marketsandmarkets.com/Market-Reports/synthetic-zeolite-market-74181103.html (Accessed: 15 April 2023).

Matinde, E., Simate, G. S., & Ndlovu, S. (2018). Mining and metallurgical wastes: A review of recycling and re-use practices. *Journal of the Southern African Institute of Mining and Metallurgy*, *118*(8), 825–844. https://doi.org/10.17159/2411-9717/2018/v118n8a5

Mehmood, S., Reddy, B. V., & Rosen, M. A. (2012). Energy analysis of a biomass co-firing based pulverized coal power generation system. *Sustainability*, *4*(4), 462–490. https://doi.org/10.3390/su4040462

Miyake, K., Hirota, Y., Uchida, Y., & Nishiyama, N. (2016). Synthesis of mesoporous MFI zeolite using PVA as a secondary template. *Journal of Porous Materials*, *23*(5), 1395–1399.

Mohamed, M. M., Zidan, F. I., & Thabet, M. (2008). Synthesis of ZSM-5 zeolite from rice husk ash: Characterization and implications for photocatalytic degradation catalysts. *Microporous and Mesoporous Materials*, *108*(1–3), 193–203. https://doi.org/10.1016/j.micromeso.2007.03.043

Monzón, J. D., Pereyra, A. M., Conconi, M. S., & Basaldella, E. I. (2017). Phase transformations during the zeolitization of fly ashes. *Journal of Environmental Chemical Engineering*, *5*(2), 1548–1553. https://doi.org/10.1016/j.jece.2017.02.022

Morgan, H. M., Bu, Q., Liang, J., Liu, Y., Mao, H., Shi, A., Lei, H., & Ruan, R. (2017). A review of catalytic microwave pyrolysis of lignocellulosic biomass for value-added fuel and chemicals. *Bioresource Technology*, *230*, 112–121. https://doi.org/10.1016/j.biortech.2017.01.059

Morgan, H. M., Liang, J., Chen, K., Yan, L., Wang, K., Mao, H., & Bu, Q. (2018). Bio-oil production via catalytic microwave co-pyrolysis of lignin and low density polyethylene using zinc modified lignin-based char as a catalyst. *Journal of Analytical and Applied Pyrolysis*, *133*, 107–116. https://doi.org/10.1016/j.jaap.2018.04.014

Mukherjee, S., Barman, S., & Halder, G. (2018). Fluoride uptake by zeolite NaA synthesized from rice husk: Isotherm, kinetics, thermodynamics and cost estimation. *Groundwater for Sustainable Development*, *7*, 39–47. https://doi.org/10.1016/j.gsd.2018.03.003

Munawar, M. A., Khoja, A. H., Naqvi, S. R., Mehran, M. T., Hassan, M., Liaquat, R., & Dawood, U. F. (2021). Challenges and opportunities in biomass ash management and its utilization in novel applications. *Renewable and Sustainable Energy Reviews*, *150*, 111451. https://doi.org/10.1016/j.rser.2021.111451

Murillo Alarcón, R., Hertel, T., François, E., Rahier, H., & Pontikes, Y. (2022). Forming zeolites and calcium silicate hydrates in Fe-rich, slag-based, porous inorganic polymers. *Cement and Concrete Research*, *153*, 106655. https://doi.org/10.1016/j.cemconres.2021.106655

Narayanan, R., & El-Sayed, M. A. (2005). Catalysis with Transition Metal Nanoparticles in Colloidal Solution:? Nanoparticle Shape Dependence and Stability. *The Journal of Physical Chemistry B*, *109*(26), 12663–12676. https://doi.org/10.1021/jp051066p

Ngoye, F., Lakiss, L., Qin, Z., Laforge, S., Canaff, C., Tarighi, M., Valtchev, V., Thomas, K., Vicente, A., Gilson, J. P., Pouilloux, Y., Fernandez, C., & Pinard, L. (2014). Mitigating coking during methylcyclohexane transformation on HZSM-5 zeolites with additional porosity. *Journal of Catalysis*, *320*(1), 118–126. https://doi.org/10.1016/j.jcat.2014.10.001

Nugraha, R. E., Prasetyoko, D., Asikin-Mijan, N., Bahruji, H., Suprapto, S., Taufiq-Yap, Y. H., & Jalil, A. A. (2021). The effect of structure directing agents on micro/mesopore structures of aluminosilicates from Indonesian kaolin as deoxygenation catalysts. *Microporous and Mesoporous Materials*, *315*, 110917. https://doi.org/10.1016/j.micromeso.2021.110917

Ojha, K., Pradhan, N. C., & Samanta, A. N. (2004). Zeolite from fly ash: Synthesis and characterization. *Bulletin of Materials Science*, *27*(6), 555–564. https://doi.org/10.1007/BF02707285

Pal, P., Das, J. K., Das, N., & Bandyopadhyay, S. (2013). Synthesis of NaP zeolite at room temperature and short crystallization time by sonochemical method. *Ultrasonics Sonochemistry*, *20*(1), 314–321. https://doi.org/10.1016/J.ULTSONCH.2012.07.012

Pan, Y., Wu, Z., Zhou, J., Zhao, J., Ruan, X., Liu, J., & Qian, G. (2013). Chemical characteristics and risk assessment of typical municipal solid waste incineration (MSWI) fly ash in China. *Journal of Hazardous Materials*, *261*, 269–276. https://doi.org/10.1016/j.jhazmat.2013.07.038

Panwar, N. L., Kothari, R., & Tyagi, V. V. (2012). Thermo chemical conversion of biomass - Eco friendly energy routes. *Renewable and Sustainable Energy Reviews*, *16*, 1801–1816. https://doi.org/10.1016/j.rser.2012.01.024

Panitchakarn, P., Laosiripojana, N., Viriya-umpikul, N., & Pavasant, P. (2014). Synthesis of high-purity Na-A and Na-X zeolite from coal fly ash. *Journal of the Air and Waste Management Association*, *64*(5), 586–596. https://doi.org/10.1080/10962247.2013.859184

Park, W., Yu, D., Na, K., Jelfs, K. E., Slater, B., Sakamoto, Y., & Ryoo, R. (2011). Hierarchically structure-directing effect of multi-ammonium surfactants for the generation of MFI zeolite nanosheets. *Chemistry of Materials*, *23*(23), 5131–5137. https://doi.org/10.1021/cm201709q

Patel, M., Zhang, X., & Kumar, A. (2016). Techno-economic and life cycle assessment on lignocellulosic biomass thermochemical conversion technologies: A review. *Renewable and Sustainable Energy Reviews*, *53*, 1486–1499. https://doi.org/10.1016/j.rser.2015.09.070

Peng, Y., Lu, X., Wang, Z., & Yan, Y. (2015). Fabrication of b?Oriented MFI Zeolite Films under Neutral Conditions without the Use of Hydrogen Fluoride. *Angewandte Chemie International Edition*, *54*(19), 5709–5712.

Petrie, B., & Macqueen, D. (2013, August). South African biomass energy little heeded but much needed. *International Institute for Environmental and Development*. http://pubs.iied.org/17165IIED

Piatak, N. M., Parsons, M. B., & Seal, R. R. (2015). Characteristics and environmental aspects of slag: A review. In *Applied Geochemistry* (Vol. 57). Elsevier Ltd. https://doi.org/10.1016/j.apgeochem.2014.04.009

Pribulová, A., Futáš, P., & Baricová, D. (2016). Processing and utilization of metallurgical slag. *Production Engineering Archives*, *11*, 2–5. https://doi.org/10.30657/pea.2016.11.01

Rahimi, A., Ulbrich, A., Coon, J. J., & Stahl, S. S. (2014). Formic-acid-induced depolymerization of oxidized lignin to aromatics. *Nature*, *515*(7526), 249–252. https://doi.org/10.1038/nature13867

Rahimi, N., & Karimzadeh, R. (2011). Catalytic cracking of hydrocarbons over modified ZSM-5 zeolites to produce light olefins: A review. *Applied Catalysis A: General*, *398*(1–2), 1–17.

Ren, L., Wu, Q., Yang, C., Zhu, L., Li, C., Zhang, P., Zhang, H., Meng, X., & Xiao, F. S. (2012). Solvent-free synthesis of zeolites from solid raw materials. *Journal of the American Chemical Society*, *134*(37), 15173–15176. https://doi.org/10.1021/ja3044954

Reza, M. S., Zhanar Baktybaevna, I., Afroze, S., Kuterbekov, K., Kabyshev, A., Bekmyrza, K. Z., Kubenova, M. M., Bakar, M. S. A., Azad, A. K., Roy, H., & Islam, M. S. (2023). Influence of Catalyst on the Yield and Quality of Bio-Oil for the Catalytic Pyrolysis of Biomass: A Comprehensive Review. In *Energies* (Vol. 16, Issue 14). Multidisciplinary Digital Publishing Institute (MDPI). https://doi.org/10.3390/en16145547

Rodella, N., Bosio, A., Dalipi, R., Zacco, A., Borgese, L., Depero, L. E., & Bontempi, E. (2017). Waste silica sources as heavy metal stabilizers for municipal solid waste incineration fly ash. *Arabian Journal of Chemistry*, *10*, S3676–S3681. https://doi.org/10.1016/j.arabjc.2014.04.006

Roth, W. J., Čejka, J., Millini, R., Montanari, E., Gil, B., & Kubu, M. (2015). Swelling and Interlayer Chemistry of Layered MWW Zeolites MCM-22 and MCM-56 with High Al Content. *Chemistry of Materials*, *27*(13), 4620–4629. https://doi.org/10.1021/acs.chemmater.5b01030

Saladini, F., Patrizi, N., Pulselli, F. M., Marchettini, N., & Bastianoni, S. (2016). Guidelines for emergy evaluation of first, second and third generation biofuels. *Renewable and Sustainable Energy Reviews*, *66*, 221–227. https://doi.org/10.1016/j.rser.2016.07.073

San Cristóbal, A. G., Castelló, R., Martín Luengo, M. A., & Vizcayno, C. (2010). Zeolites prepared from calcined and mechanically modified kaolins. A comparative study. *Applied Clay Science*, *49*(3), 239–246. https://doi.org/10.1016/j.clay.2010.05.012

Sayehi, M., Delahay, G., & Tounsi, H. (2022a). Synthesis and characterization of ecofriendly materials zeolite from waste glass and aluminum scraps using the hydrothermal technique. *Journal of Environmental Chemical Engineering*, *10*(6), 108561. https://doi.org/10.1016/J.JECE.2022.108561

Sayehi, M., Tounsi, H., Garbarino, G., Riani, P., & Busca, G. (2020b). Reutilization of silicon- and aluminum- containing wastes in the perspective of the preparation of SiO2-Al2O3 based porous materials for adsorbents and catalysts. *Waste Management*, *103*, 146–158. https://doi.org/10.1016/j.wasman.2019.12.013

Serrano, D. P., Escola, J. M., & Pizarro, P. (2013). Synthesis strategies in the search for hierarchical zeolites. *Chemical Society Reviews*, *42*(9), 4004–4035. https://doi.org/10.1039/c2cs35330j

Shahbaz, M., AlNouss, A., Ghiat, I., Mckay, G., Mackey, H., Elkhalifa, S., & Al-Ansari, T. (2021). A comprehensive review of biomass based thermochemical conversion technologies integrated with CO2 capture and utilisation within BECCS networks. *Resources, Conservation and Recycling*, *173*, 105734. https://doi.org/10.1016/j.resconrec.2021.105734

Statistics, S. (2020). Fact sheets Sheets 1 to 10 : South Africa and provinces Sheets 11 to 13 : Commodity groups. In *CENSUS of Commercial Agriculture 2017 (CoCA)* (Vol. 2).

Strezov, V., Patterson, M., Zymla, V., Fisher, K., Evans, T. J., & Nelson, P. F. (2007). Fundamental aspects of biomass carbonisation. *Journal of Analytical and Applied Pyrolysis*, *79*(1-2 SPEC. ISS.), 91–100. https://doi.org/10.1016/j.jaap.2006.10.014

Su, L., Liu, L., Zhuang, J., Wang, H., Li, Y., Shen, W., Xu Ã, Y., & Bao ÃÃ, X. (2003). Creating mesopores in ZSM-5 zeolite by alkali treatment: a new way to enhance the catalytic performance of methane dehydroaromatization on Mo/HZSM-5 catalysts. *Catalysis Letters*, *91*(3–4).

Sugano, Y., Sahara, R., Murakami, T., Narushima, T., Iguchi, Y., & Ouchi, C. (2005). Hydrothermal synthesis of zeolite a using blast furnace slag. *ISIJ International*, *45*(6), 937–945. https://doi.org/10.2355/isijinternational.45.937

Tao, Y., Kanoh, H., & Kaneko, K. (2003). ZSM-5 monolith of uniform mesoporous channels. *Journal of the American Chemical Society*, *125*(20), 6044–6045. https://doi.org/10.1021/ja0299405

Tauanov, Z., Shah, D., Inglezakis, V., & Jamwal, P. K. (2018). Hydrothermal synthesis of zeolite production from coal fly ash: A heuristic approach and its optimization for system identification

of conversion. *Journal of Cleaner Production*, *182*, 616–623. https://doi.org/10.1016/J.JCLEPRO.2018.02.047

Teir, S., Eloneva, S., Fogelholm, C. J., & Zevenhoven, R. (2007). Dissolution of steelmaking slags in acetic acid for precipitated calcium carbonate production. *Energy*, *32*(4), 528–539. https://doi.org/10.1016/j.energy.2006.06.023

Tung, D., Phuong, N., Van Tri, T., Sura, N., Trung, N., Xuan, D., & Thu, H. (2012). Effect of feedstock properties on the performance of ZSM-5 additive in catalytic cracking reaction. *Petrovietnam*, *10*, 59–64.

Tzoulaki, D., Jentys, A., Pérez-Ramírez, J., Egeblad, K., & Lercher, J. A. (2012). On the location, strength and accessibility of Bronsted acid sites in hierarchical ZSM-5 particles. *Catalysis Today*, *198*(1), 3–11. https://doi.org/10.1016/j.cattod.2012.03.078

Ujaczki, É., Feigl, V., Molnár, M., Cusack, P., Curtin, T., Courtney, R., O'Donoghue, L., Davris, P., Hugi, C., Evangelou, M. W. H., Balomenos, E., & Lenz, M. (2018). Re-using bauxite residues: benefits beyond (critical raw) material recovery. *Journal of Chemical Technology and Biotechnology*, *93*(9), 2498–2510. https://doi.org/10.1002/jctb.5687

Usino, D. O., Ylitervo, P., Moreno, A., Sipponen, M. H., & Richards, T. (2021). Primary interactions of biomass components during fast pyrolysis. *Journal of Analytical and Applied Pyrolysis*, *159*, 1–10. https://doi.org/10.1016/j.jaap.2021.105297

Valtchev, V. P., Tosheva, L., & Bozhilov, K. N. (2005). Synthesis of zeolite nanocrystals at room temperature. *Langmuir*, *21*(23), 10724–10729. https://doi.org/10.1021/la050323e

Van De Sande, J., Peys, A., Hertel, T., Rahier, H., & Pontikes, Y. (2020). Upcycling of non-ferrous metallurgy slags: Identifying the most reactive slag for inorganic polymer construction materials. *Resources, Conservation and Recycling*, *154*, 104627. https://doi.org/10.1016/j.resconrec.2019.104627

Van Meerbeek, K., Appels, L., Dewil, R., Calmeyn, A., Lemmens, P., Muys, B., & Hermy, M. (2015). Biomass of invasive plant species as a potential feedstock for bioenergy production. *Biofuels, Bioproducts and Biorefining*, *9*(3), 273–282. https://doi.org/10.1002/bbb.1539

Vassilev, S. V., Baxter, D., Andersen, L. K., & Vassileva, C. G. (2013). An overview of the composition and application of biomass ash.: Part 2. Potential utilisation, technological and ecological advantages and challenges. *Fuel*, *105*, 19–39. https://doi.org/10.1016/j.fuel.2012.10.001

Verma, A. S., Suri, N. M., & Kant, S. (2017). Applications of bauxite residue: A mini-review. *Waste Management and Research*, *35*(10), 999–1012. https://doi.org/10.1177/0734242X17720290

Vigil de la Villa Mencía, R., Goiti, E., Ocejo, M., & Giménez, R. G. (2020). Synthesis of zeolite type analcime from industrial wastes. *Microporous and Mesoporous Materials*, *293*, 1–9. https://doi.org/10.1016/j.micromeso.2019.109817

Vigil de la Villa Mencía, R., Goiti, E., Ocejo, M., & Giménez, R. G. (2020b). Synthesis of zeolite type analcime from industrial wastes. *Microporous and Mesoporous Materials*, *293*, 1–9. https://doi.org/10.1016/j.micromeso.2019.109817

Wakui, K., Satoh, K. -i, Sawada, G., Shiozawa, K., Matano, K. -i, Suzuki, K., Hayakawa, T., Murata, K., Yoshimura, Y., & Mizukami, F. (1999). Catalytic cracking of n-butane over rare earth-loaded HZSM-5 catalysts. *Journal of The Japan Petroleum Institute*, *42*(5), 307–314.

Wakui, K., Satoh, K., Sawada, G., Shiozawa, K., Matano, K., Suzuki, K., Hayakawa, T., Yoshimura, Y., Murata, K., & Mizukami, F. (2002a). Dehydrogenative cracking of n-butane over modified HZSM-5 catalysts. *Catalysis Letters*, *81*(1), 83–88.

Wan, J., Wei, Y., Liu, Z., Li, B., Qi, Y., Li, M., Xie, P., Meng, S., He, Y., & Chang, F. (2008). A ZSM-5-based catalyst for efficient production of light olefins and aromatics from fluidized-bed naphtha catalytic cracking. *Catalysis Letters*, *124*(1), 150–156.

Wan, Y., & Zhao, D. (2007). On the controllable soft-templating approach to mesoporous silicates. In *Chemical Reviews* (Vol. 107, Issue 7, pp. 2821–2860). https://doi.org/10.1021/cr068020s

Wang, B., Guo, Y., Zhu, J., Ma, J., & Qin, Q. (2023). A review on titanosilicate-1 (TS-1) catalysts: Research progress of regulating titanium species. *Coordination Chemistry Reviews*, *476*, 214931. https://doi.org/10.1016/J.CCR.2022.214931

Wang, S., He, B., Tian, R., Sun, C., Dai, R., Li, X., Wu, X., An, X., & Xie, X. (2018). Ni-hierarchical Beta zeolite catalysts were applied to ethanol steam reforming: Effect of sol gel method on loading Ni and the role of hierarchical structure. *Molecular Catalysis*, *453*, 64–73. https://doi.org/10.1016/J.MCAT.2018.04.034

Wang, S., Dai, G., Yang, H., & Luo, Z. (2017). Lignocellulosic biomass pyrolysis mechanism: A state-of-the-art review. In *Progress in Energy and Combustion Science* (Vol. 62, pp. 33–86). Elsevier Ltd. https://doi.org/10.1016/j.pecs.2017.05.004

Wang, Z., Li, C., Cho, H. J., Kung, S. C., Snyder, M. A., & Fan, W. (2015). Direct, single-step synthesis of hierarchical zeolites without secondary templating. *Journal of Materials Chemistry A*, *3*(3), 1298–1305. https://doi.org/10.1039/c4ta05031b

Wen, J., Dong, H., & Zeng, G. (2018). Application of zeolite in removing salinity/sodicity from wastewater: A review of mechanisms, challenges and opportunities. *Journal of Cleaner Production*, *197*, 1435–1446. https://doi.org/10.1016/j.jclepro.2018.06.270

Wendisch, V. F., Kim, Y., & Lee, J. H. (2018). Chemicals from lignin: Recent depolymerization techniques and upgrading extended pathways. In *Current Opinion in Green and Sustainable Chemistry* (Vol. 14, pp. 33–39). Elsevier B.V. https://doi.org/10.1016/j.cogsc.2018.05.006

Wu, S., Shen, D., Hu, J., Zhang, H., & Xiao, R. (2016). Cellulose-lignin interactions during fast pyrolysis with different temperatures and mixing methods. *Biomass and Bioenergy*, *90*, 209–217. https://doi.org/10.1016/j.biombioe.2016.04.012

Xia, L. yin, Zhong, H., & Liu, G. yi. (2010). Flotation techniques for separation of diaspore from bauxite using Gemini collector and starch depressant. *Transactions of Nonferrous Metals*

Society of China (English Edition), *20*(3), 495–501. https://doi.org/10.1016/S1003-6326(09)60168-0

Xia, L., Zhong, H., Liu, G., Huang, Z., & Chang, Q. (2009). Flotation separation of the aluminosilicates from diaspore by a Gemini cationic collector. *International Journal of Mineral Processing*, *92*(1–2), 74–83. https://doi.org/10.1016/j.minpro.2009.02.012

Xiaoning, W., Zhen, Z., Chunming, X., Aijun, D., Li, Z., & Guiyuan, J. (2007). Effects of light rare earth on acidity and catalytic performance of HZSM-5 zeolite for catalytic cracking of butane to light olefins. *Journal of Rare Earths*, *25*(3), 321–328.

Xu, R., Chen, J., Gao, Z., & Yan, W. (2007). From zeolites to porous MOF materials-the 40th Anniversary of International Zeolite Conference. Part A. *Proceedings of the 15th International Zeolite Conference*.

Xue, N., Liu, N., Nie, L., Yu, Y., Gu, M., Peng, L., Guo, X., & Ding, W. (2010). 1-Butene cracking to propene over P/HZSM-5: Effect of lanthanum. *Journal of Molecular Catalysis A: Chemical*, *327*(1–2), 12–19.

Yoldi, M., Fuentes-Ordoñez, E. G., Korili, S. A., & Gil, A. (2019). Zeolite synthesis from industrial wastes. *Microporous and Mesoporous Materials*, *287*, 183–191. https://doi.org/10.1016/j.micromeso.2019.06.009

Yin, C., Wei, Y., Wang, F., & Chen, Y. (2013). Introduction of mesopority in zeolite ZSM-5 using resin as templates. *Materials Letters*, *98*, 194–196. https://doi.org/10.1016/j.matlet.2013.02.017

Zeng, X., Hu, X., Song, H., Xia, G., Shen, Z. Y., Yu, R., & Moskovits, M. (2021). Microwave synthesis of zeolites and their related applications. *Microporous and Mesoporous Materials*, *323*, 111262. https://doi.org/10.1016/j.micromeso.2021.111262

Zhang, B., von Keitz, M., & Valentas, K. (2009). Thermochemical liquefaction of high-diversity grassland perennials. *Journal of Analytical and Applied Pyrolysis*, *84*(1), 18–24. ttps://doi.org/10.1016/j.jaap.2008.09.005

Zhang, B., Zhong, Z., Xie, Q., Chen, P., & Ruan, R. (2015). Reducing coke formation in the catalytic fast pyrolysis of bio-derived furan with surface modified HZSM-5 catalysts. *RSC Advances*, *5*(69), 56286–56292.

Zhang, H., Jin, M., Xiong, Y., Lim, B., & Xia, Y. (2013). Shape-Controlled Synthesis of Pd Nanocrystals and Their Catalytic Applications. *Accounts of Chemical Research*, *46*(8), 1783–1794. https://doi.org/10.1021/ar300209w

Zhang, K., & Ostraat, M. L. (2016). Innovations in hierarchical zeolite synthesis. *Catalysis Today*, *264*, 3–15.

Zhang, L., Qu, S., Wang, L., Zhang, X., & Liu, G. (2013). Preparation and performance of hierarchical HZSM-5 coatings on stainless-steeled microchannels for catalytic cracking of hydrocarbons. *Catalysis Today*, *216*, 64–70.

Zhang, X., Li, C., Zheng, S., Di, Y., & Sun, Z. (2022). A review of the synthesis and application of zeolites from coal-based solid wastes. *International Journal of Minerals, Metallurgy and Materials*, *29*, 1–21. https://doi.org/10.1007/s12613-021-2256-8

Zhang, X., Liu, D., Xu, D., Asahina, S., Cychosz, K. A., Kumar Varoon, A., Osamu, T., Yasser Al, W., Saleh Al, H., Bhan, A., Matthias, T., & Michael, T. (2012). Synthesis of Self-Pillared Zeolite Nanosheets by Repetitive Branching. *Science*, *336*(6089), 1684–1687. www.sdencennag.org

Zhao, D., Huo, Q., Feng, J., Melosh, N., Fredickson, G. H., Chmelka, B. F., & Stucky, G. D. (1998). Triblock copolymer syntheses of mesoporous silica with periodic 50 to 300 angstrom pores. *Science*, *278*(5350), 548–552.

Zheng, J., Zhang, H., Liu, Y., Wang, G., Kong, Q., Pan, M., Tian, H., & Li, R. (2016). Synthesis of wool-ball-like ZSM-5 with enlarged external surfaces and improved diffusion: a potential highly-efficient FCC catalyst component for elevating pre-cracking of large molecules and catalytic longevity. *Catalysis Letters*, *146*(8), 1457–1469.

Zhu, X., Liu, S., Song, Y., & Xu, L. (2005). Catalytic cracking of C4 alkenes to propene and ethene: Influences of zeolites pore structures and Si/Al2 ratios. *Applied Catalysis A: General*, *288*(1–2), 134–142.

Zhu, Y., Hua, Z., Zhou, J., Wang, L., Zhao, J., Gong, Y., Wu, W., Ruan, M., & Shi, J. (2011). Hierarchical mesoporous zeolites: Direct self-assembly synthesis in a conventional surfactant solution by kinetic control over the zeolite seed formation. *Chemistry - A European Journal*, *17*(51), 14618–14627. https://doi.org/10.1002/chem.201101401

CHAPTER 3

3. ACID LEACHING OF BLAST FURNACE SLAG FOR ENHANCED ZEOLITE SYNTHESIS

Research paper under review.

Abstract

The iron- and steelmaking industry generates a substantial amount of waste in the form of blast furnace slag (BFS). Previous studies have highlighted the potential of utilizing BFS, which is composed of SiO_2 and Al_2O_3, for the synthesis of zeolitic materials. However, the presence of impurities such as Ca and Mg has been found to hinder the hydrothermal synthesis process by inhibiting zeolite crystallization. To address this, acid leaching of BFS has been proposed as a viable pretreatment method. This study aims to evaluate the effectiveness of leaching conditions in reducing Ca and Mg from BFS, thereby improving zeolite synthesis from BFS. The BFS under investigation contained significant amounts of SiO_2 (35.1 wt.%), Al_2O_3 (16.1 wt.%), CaO (30.6 wt.%) and MgO (10.5 wt.%). X-ray diffraction analysis revealed the mineral phase in the BFS as akermanite, while the products derived from both the raw slag and leached slag consisted of augite and zeolite ZSM-5, respectively. The acid leaching tests successfully solubilized Ca and Mg from the BFS, with a maximum leaching efficiency of Ca at 80.4% and Mg at 71.1%. The optimal leaching conditions were determined to be a solids concentration of 8 wt.%, an HCl concentration of 3 mol/L, and a leaching time of 90 min. It was observed that acid leaching of BFS resulted in a transformation of the mineral phase of akermanite to augite. The initial concentration of CaO and MgO in the starting material significantly influenced the formation of zeolite ZSM-5 during the hydrothermal treatment. The leached slag, with reduced impurities, demonstrated successful conversion into zeolite ZSM-5. However, the resultant crystals exhibited a distinctive ball-shaped morphology.

3.1. Introduction

South Africa's iron and steel manufacturing is an energy-intensive industry within the manufacturing sector that contributes significantly to the country's economy. Recent economic indicators have shown a decline in the sustainability of the industry. This decline has been attributed to critical factors such as a lack of electrical energy supply, increasing steel imports, increasing input costs, and inadequate interventions regarding environmental emissions (Raaleka, 2017). Various mitigating strategies have been reported; however, the development of sustainable downstream beneficiation processes has been deemed a promising solution to curb the industry's environmental impact. Blast furnace slag (BFS) is one of the significant by-products of the iron and steel industry; it is produced by burning iron ore to molten iron in a blast furnace. This would imply that the composition of BFS is controlled by the raw materials charged, whereas the quantity produced depends on the production rate of the molten iron. The global output of BFS has been estimated to be 325-390 megatons, of which China contributes 64% (Duan et al., 2022b).

Blast furnace slag is an inorganic granulated material consisting primarily of Al_2O_3, SiO_2, MgO, and CaO, amongst other trace metals (Mn, Ti, Cr, Ni, P, K, and Na). Due to its beneficial properties, it has found secondary use as a cement replacement material (Ojha et al., 2023), an alternative subbase material in road construction (Hunter & Kang, 2022), and used as fertilizer for soil amendment (Chen et al., 2022). However, these secondary measures must adequately utilize the slag's full potential. In recent years, researchers have investigated the recovery of value-added minerals from BFS to develop new recycling processes. One of these is the application of BFS in the synthesis of zeolitic materials. Zeolites are microporous inorganic materials comprising a three-dimensional tetrahedral aluminosilicate framework. Zeolites have numerous applications due to their hydrothermal stability, ion exchange capability, and large surface area. The three-dimensional crystalline structure comprises Si and Al metal ions connected through oxygen atoms. The Si and Al composition is primarily used to control the physiochemical properties of zeolites (Vigil de la Villa Mencía et al., 2020). Furthermore, the synthesis conditions are manipulated to obtain a particular pore structure (shape and size). Studies have shown the successful conversion of slag waste (from the iron and steel industry) into zeolitic materials. However, impurities in the slag waste negatively affect the conversion process. This has necessitated the need for a pretreatment stage.

The major components (Al_2O_3 and SiO_2) in BFS make it a suitable industrial waste resource for zeolite synthesis. Owing to its large production, BFS slag as a precursor for the synthesis of zeolite has been reported to present multifarious benefits such as waste valorization, waste management, and mitigation of environmental pollution. Sugano et al. (2005) used the conventional hydrothermal synthesis technique to convert BFS into zeolite LTA. Three slag samples with varying CaO compositions (40, 20, and 15 wt.%) were investigated. It was reported that zeolite LTA was successfully synthesized at a low CaO composition (15 wt.%), whereas the high CaO composition (40 wt.%) resulted in inorganic minerals (hydrogarnet and tobermorite). Kuwahara et al. (2008) employed steel slag to synthesize zeolites type X and Y using the hydrothermal synthesis method. The concentration of CaO and MgO were reported to be 38.96 and 11.27 wt.%, respectively. The slag had to be acid-treated to a composition of 1.44 wt.% (CaO) and 0.33 wt.% (MgO) to synthesize the zeolitic materials successfully. It was concluded that the presence of CaO and MgO affects the synthesis process by inhibiting zeolite crystallization. That is, during the early stages of zeolite crystallization, silica and

alumina from the slag are solubilized into the Na^+ and OH^- rich solution. Then, the primary building units, consisting of aluminosilicate species, are assembled to form small crystalline nuclei. Additional building units from the surrounding solution continue to attach to the nuclei, causing the crystals to grow. The solubilized Ca and Mg ions interact with the crystal surface, altering the reactivity and surface energy of the crystal (Kuwahara et al., 2009). Li et al. (2022) published the reaction mechanism of Ca^{2+} species forming complex aluminosilicate compounds [$(Na,Ca)_2(Si,Al)_5O_{10}$], which affects crystal growth. Kuwahara et al. (2009) resolved the Ca and Mg problem by adding phosphate, in the form of H_3PO_4, during the aging process to precipitate Mg and formed a hydroxyapatite-zeolite composite material, which is dependent on the composition of Ca/P = 1.67. The waste material was steel slag, and the novel technique did not require pretreatment.

Literature has shown the successful transformation of aluminosilicate-containing wastes into zeolites by reaction with alkalis. However, the common challenge with using slag from the iron and steel industry for zeolite synthesis is the high presence of impurities (CaO and MgO). This has propelled the scientific community to implement pretreatment methods such as alkaline leaching or fusion to solubilize Al_2O_3 and SiO_2 and acid leaching to remove most metal oxide impurities. The introduction of acid leaching as a pretreatment method has shown to be a less demanding option owing to its lower energy requirements and the affinity of the impurities to react with the acid (Murakami et al., 2011). However, there needs to be more understanding of how the leaching conditions affect the leachability of the impurities. Therefore, this study aims to investigate the impact of acid-leaching conditions on the pretreatment of BFS to enhance the zeolite synthesis method. The study further explored the relationship between the pretreatment conditions and the resulting zeolite product. Therefore, optimizing the acid-leaching process to achieve maximum removal of impurities at low acid consumption is beneficial.

3.2. Materials and Methods

3.2.1. Chemicals and Materials

The blast furnace slag used in this study is a by-product of an iron- and steelmaking industry in South Africa. The sample was received as granulated slag (2 kg) with a particle size of ~6 cm. The slag was crushed using a jaw crusher and milled in a rod mill to achieve a particle size range of 600 – 200 µm. The milled sample was blended using a Jones Riffler Splitter and then homogenized. The prepared sample was oven-dried at 120°C for 24 h, and the resulting material was considered ready for the pretreatment experiments. Hydrochloric acid (32%, AR) was used as the acid of choice for the leaching experiments and was obtained from a local chemical supplier in South Africa. Sodium Hydroxide (98%, AR) was used as feed for the hydrothermal synthesis method and was obtained from a local supplier. Deionized water was used to prepare all the solutions and was obtained from a Milli-Q® water purification system.

3.2.2. Acid Leaching Process

The acid-leaching experiments were performed using the experimental setup shown in ***Figure 3.1***. In a typical experiment, a predetermined mass of the prepared raw slag was mixed with 150 mL of HCl solution inside a 500 mL flat-bottomed flask. The slurry was simultaneously agitated (225 rpm) and heated at 60°C using a heating-magnetic stirring plate. The leaching process was allowed to proceed for a predetermined time interval, ensuring sufficient interaction between the BFS and acid. The

resulting mixture was gravity-filtered to obtain the leachate. The leachate was collected and stored for chemical analysis to determine the leaching efficiency (%) [Eq. 3.1]. The solids with the highest and lowest leaching efficiencies were washed with deionized water, filtered, air-dried, and ground to be prepared as pretreated slag (PTS). The purpose of only considering the extremes of the leaching process was to prioritize a targeted approach that allowed capturing the most significant differences in slag composition resulting from leaching. This approach provided valuable insights into the boundaries of the leaching process's impact on zeolite synthesis.

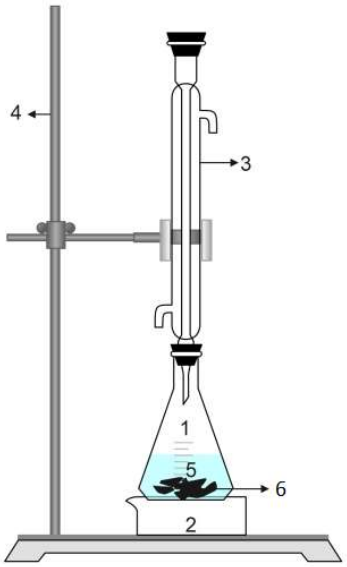

Figure 3.1. Leaching experimental setup. 1) Flat-bottomed flask, 2) heating-magnetic stirring plate, 3) Allihn glass condenser, 4) Clamp stand, 5) HCl solution and 6) Raw slag.

$$\%\ \text{Leaching efficiency} = \left(\frac{C_f}{C_0}\right) \times 100\% \tag{3.1}$$

where C_0 and C_f are the initial and final concentrations (ppm) of the species (Ca and Mg) in solution, respectively. The initial concentrations of Ca and Mg were determined by solubilizing all the metal oxides found in the prepared raw slag and determining their respective concentrations. Furthermore, the initial concentration was measured for each of the solids concentration.

3.2.3. Experimental Design

A multivariable response surface design was used to investigate and optimize the acid-leaching conditions statistically. The leaching conditions that were identified to affect the efficiency significantly were solids concentration (w/w), leaching time (min), and acid concentration (M) [***Table 3.1***]. These conditions were selected based on a thorough literature survey and preliminary leaching tests. The statistical modeling of the acid leaching process was conducted using Design Expert® Software of Stat-Ease Inc. (version 12.0).

A 3-level Box Behnken (BB) surface design was applied to investigate the effect of leaching conditions on the removal of CaO and MgO. The experimental design offers a robust statistical approach to optimizing the leaching conditions while reducing the required experimental runs. ***Table 3.1*** shows the BB design's experimental matrix, the varied dependent parameters (solids concentration,

leaching time and acid concentration), and their respective levels. The BB design uses the high (+1) and low (-1) values from the experimental matrix to statistically investigate the linear and interaction effects of the parameters. It further investigates the quadratic effects by including central points (0) in the experimental domain, thus allowing for the determination of variance in the data set. A total of 17 leaching experiments were conducted as per Eq. 3.2. While the leaching conditions were varied systematically, a full multivariate optimization study was not conducted. Instead, conditions were selected based on their effectiveness in minimizing Ca and Mg content while preserving Si and Al.

Table 3.1. Leaching experimental matrix.

Variables	Coding	Levels		
		-1	**0**	**1**
Raw slag conc. (wt.%)	x_1	2	5	8
Acid conc. (mol/L)	x_2	1	2	3
Leaching time (min)	x_3	30	90	150

$$N = 2k(k-1) + c_p \tag{3.2}$$

where N is the number of experimental runs, k is the number of factors, and c_p is the number of central points. The standard recommendation for central points is often 5.

3.2.4. Zeolite Synthesis

Both slags (BFS and PTS) were transformed into zeolitic materials using the hydrothermal synthesis method. This was done by mixing the slag (1.0226 g), 3M NaOH solution (1.5868 g), Tetrapropylammonium bromide [TPABr] (0.1109 g), and deionized water (21.2253 g) to create a synthesis gel. The gel was allowed to cure for 24 h, after which it was hydrothermally treated at 200°C for 13 h in a Teflon-sealed vessel. The resulting mixture was filtered, washed with deionized water, and oven-dried for 24 h. The washed solids were calcined for 5 h at 550°C to obtain a zeolite-based material.

3.2.5. Analytical Methods

The concentration of metals (Ca and Mg) in the solution was measured using an atomic absorption spectrometry (AAS). The measurements were done using an AA-7000F Shimadzu instrument fitted with a double-beam optical system and a flame automizer for enhanced flame analysis. The elemental composition of the raw and pretreated slag was determined using X-ray fluorescence (XRF) spectrometer. The primary elements were determined using the Norrish Fusion method and the Panalytical Axios spectrometer instrument. The synthesized porous materials were characterized using X-ray Diffraction (XRD) to evaluate the crystalline structure and identify the mineral phases. The instrument employed was the Bruker D2 Phaser powder X-ray analyzer, which consisted of sealed copper X-ray tubes (CuK_α) that emit radiation at a wavelength (λ) of 1.5418 Å.

3.3. Results and Discussion

3.3.1. Leaching Efficiency

The acid leaching experiments were conducted under varying conditions, such as leaching time (min), acid concentration (mol/L), and BFS concentration (wt.%). A total of 17 experiments were conducted as per the guidance of the Box Behnken (BB) surface design. All leaching experiments were conducted at a temperature of 60°C and an agitation of 225 rpm. ***Table 3.2*** shows the leaching efficiencies for each experimental run. The final concentrations of Ca and Mg in the solution were measured for each experimental run and compared to their respective initial concentrations to compute the leaching efficiency (***Table 3.2***). The actual concentration obtained for each experimental run is shown in *7.1* Appendix A (Acid Leaching Experiments). Run 2 obtained the lowest leaching efficiency (Ca = 5.4% and Mg = 5.8%), and this was due to the low solids concentration (2 wt.%) and acid concentration (1 mol/L) used. While the low solid concentrations reduce the absolute amount of Ca and Mg available, the higher Cl^-/Ca and Cl^-/Mg ratios could enhance % extraction. However, in this study, the extraction efficiency trend obtained was contrary, which could be attributed to secondary dissolution, re-adsorption, or precipitation of the dissolved species [Ca^{2+} and Mg^{+2}] (Wang et al., 2021). Run 6 achieved the highest leaching efficiency for Ca (81.5%), whereas Run 10 achieved the highest leaching efficiency for Mg (71.1%).

When comparing the Ca leaching efficiencies of Runs 6 and 10, it was resolved that Run 10 obtained the highest leaching efficiency for both elements. Therefore, the most favorable leaching conditions were a solids concentration of 8 wt.%, an HCl concentration of 3 mol/L, and a leaching time of 90 min. Overall, the concentration of Ca in the solution was 11 times greater than that of Mg due to the high content of CaO in the BFS and the high reactivity of Ca with the acid (Duan et al., 2022a). Lee et al. (2021) studied the selective leaching of Ca from steel slag, along with impurities (Mg, Si, and Al). Various extractants (HCl, NaOH, NH_4Cl, and NH_4OH) were used at different concentrations. Hydrochloric acid (2 mol/L) was reported to achieve the highest extraction efficiency (Ca = 97% and Mg = 46%). Interestingly, a significant amount of Al was leached with an efficiency of 35%. A similar trend was found in the current study, where Al was significantly reduced in the PTS; this is shown by the chemical composition reported in ***Table 3.3***.

Table 3.2. Acid leaching efficiency.

Run	BFS conc. (wt%)	HCl conc. (mol/L)	Leaching time (min)	Ca extraction (%)	Mg extraction (%)
1	5	2	90	45.7	28.7
2	**2**	**1**	**90**	**5.4**	**5.8**
3	8	1	90	49.8	22.2
4	2	3	90	18.5	11.7
5	2	2	150	21.1	11.2
6	8	2	150	81.5	61.3
7	5	2	90	47.2	23.1
8	5	2	90	39.3	23.0
9	5	3	150	61.5	43.7
10	**8**	**3**	**90**	**80.4**	**71.1**
11	5	2	90	43.3	27.0
12	8	2	30	68.0	56.8
13	5	1	150	39.2	18.5
14	5	3	30	44.4	23.7
15	2	2	30	13.6	12.1
16	5	1	30	28.3	7.3
17	5	2	90	42.6	29.5

Duan et al. (2022a) studied the reaction mechanism between HCl and BFS during leaching. It was reported that CaO, MgO, and Al_2O_3 were dissolved into the leachate to form aqueous mineral salts of $CaCl_2$, $MgCl_2$, and $AlCl_3$, respectively. Furthermore, the leaching reactions were reported to follow a three-stage rate mechanism: *(1)* the ions (Cl^- and H^+) from the hydrochloric acid are transferred from the bulk solution to the surface of the particle and further diffuse inside the particle to the reaction zone; *(2)* the reactivity of the species (Ca^{2+}, Mg^{2+} and Al^{3+}) inside the particle to form mineral salts (reactions 3.1 to 3.3) and the diffusion through solid-acid mixture to the surface of the particle and *(3)* the migration of the mineral salts from the surface of the particle to the bulk acid solution. The second-rate stage was reported to be the highest energy-consuming and the rate-controlling stage.

$$CaO + 2HCl = CaCl_2 + H_2O \quad \text{(R3.1)}$$

$$MgO + 2HCl = MgCl_2 + H_2O \quad \text{(R3.2)}$$

$$Al_2O_3 + 6HCl = 2AlCl_3 + 3H_2O \quad \text{(R3.3)}$$

3.3.2. Effect of Leaching Conditions

Understanding the impact of leaching conditions on the dissolution of CaO and MgO is essential for resource management and utilization of the slag. The batch leaching experiments were conducted at a constant temperature (60°C) and agitation (225 rpm). The results were processed to compare the leachability of CaO and MgO from BFS generated by the iron and steel industry. A statistical analysis was conducted on the leaching results to develop polynomial model equations that describe the leaching of Mg and Ca. The models and their statistical significance are presented in *7.1* Appendix A (Acid Leaching Experiments). ***Figure 3.2*** shows the effect of leaching conditions on the dissolution behavior of Ca (***Figure 3.2a and c***) and Mg (***Figure 3.2b and d***). Overall, it was seen that each variable had a linear effect on the dissolution of Ca and Mg. However, the slope of the linear curve was significantly steep for the solids concentration (wt.%) and shallow for the leaching time and acid concentration (mol/L). This implies that the solids concentration significantly influenced the leaching efficiency compared to the other variables. The pH level of the solution before and after leaching was found to be highly acidic (below 1). Therefore, it was not investigated further. Zhang et al. (2012) investigated the dissolution mechanism of various elements (Mg, Ca, Si, P, and Fe) from two steel slags ($CaO/SiO_2 < 1.0$ and $CaO/SiO_2 > 1.0$). It was concluded that the CaO/SiO_2 ratio plays a crucial role in the dissolution of the elements. As such, it was shown that the dissolution behavior of Mg and Ca followed a clear linear trend when $CaO/SiO_2 < 1.0$. The same phenomenon was seen in the current study due to the CaO/SiO_2 ratio being below 1.0.

Figure 3.2a and b show the dual effect of acid and solids concentration on the leaching efficiency of Ca and Mg. An increase in acid concentration from 1 mol/L to 3 mol/L resulted in an increase in leaching efficiency from 10.5% to 31% (Ca) and 7% to 23.3% (Mg). An increase in acid concentration resulted in the rapid leaching of Ca and Mg due to the increased presence of H^+ ions (Liu et al., 2014). The solids concentration varied from 2 to 8 wt.% and had a significant impact on the leaching efficiency. It was observed that an increase in solids concentration resulted in leaching efficiencies of 65% (Ca) and 41% (Mg). However, the 3D surface plots showed that a combination of acid (3 mol/L) and solids (8 wt.%) concentrations gave maximum leaching of 85% (Ca) and 65.5% (Mg). The effect of leaching time is illustrated in ***Figure 3.2c and 3.2d,*** where the time was varied from 30 to 150 min—the leaching time had minimal impact on the leaching efficiency for both elements. This is shown by the shallow increase in the leaching efficiency with an increase in the leaching time. This same trend was observed by Liu et al. (2014) and Meng et al. (2015). However, a dual effect of leaching time (150 min) and solids concentration (8 wt.%) results in maximum leaching efficiency (Ca = 85% and Mg = 65.5%).

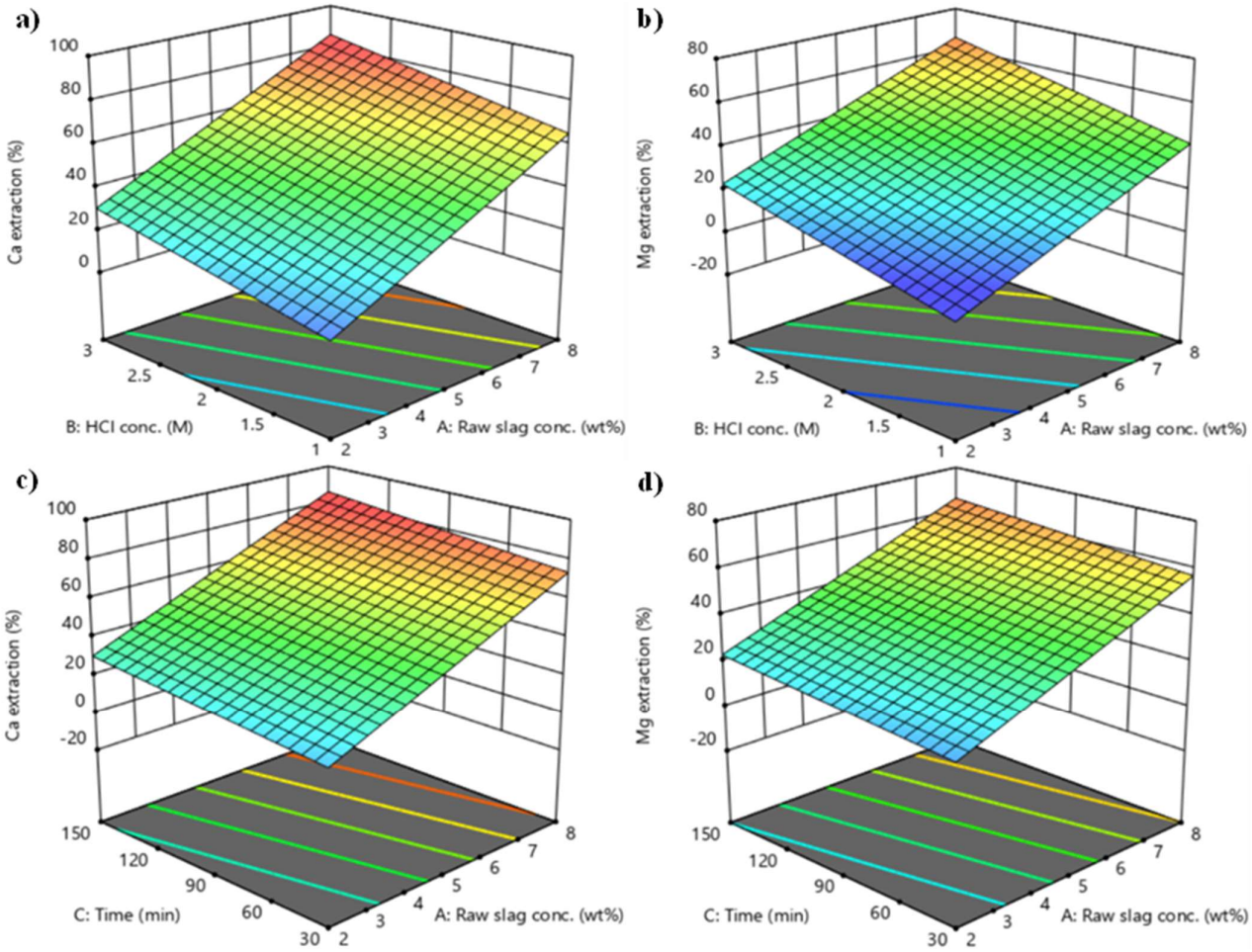

Figure 3.2. Effect of various parameters on the leaching process based on Run 10.

3.3.3. Chemical Composition of Powdered Samples

Table 3.3 displays the concentration of metal oxides in both blast furnace slag (BFS) and pretreated slag (PTS). The solid samples obtained from the experiments with the highest (Run 10) and lowest (Run 2) leaching efficiencies were characterized using XRF. The BFS sample primarily consisted of SiO_2 (35.1 wt.%), Al_2O_3 (16.1 wt.%), CaO (30.6 wt.%), and MgO (10.5 wt.%). Other components included trace amounts of Fe_2O_3, MnO, Na_2O, K_2O, TiO_2, P_2O_5, Cr_2O_3. Beneficiation of BFS resulted in a considerable reduction in CaO and MgO. In Run 2, the composition of CaO and MgO was 21.8 wt.% and 8.1 wt.%, respectively. In contrast, Run 10 had a composition of 4.83 wt.% CaO and 2.54 wt.% MgO. The PTS obtained from Run 10 exhibited low levels of CaO and MgO and was utilized as feedstock for zeolite synthesis. Notably, the composition of Al_2O_3 in the PTS (Run 10) was considerably reduced to 4.46 wt.% (***Table 3.3***). This reduction was attributed to the propensity of Al_2O_3 to react with HCl and dissolve in solution (Duan et al., 2022a). Consequently, this alteration would influence the SiO_2/Al_2O_3 ratio in the resulting zeolite, leading to variations in its physicochemical properties.

Wajima and Ikegami (2008) conducted an investigation on the acid leaching of paper sludge ash (PSA) with the aim of synthesizing zeolite. The composition of the ash primarily consisted of SiO_2

(43.0 wt.%), Al_2O_3 (28.3 wt.%), CaO (19.0 wt.%), and MgO (7.6 wt.%). Post leaching, the composition of CaO and MgO decreased to 6.9 and 6.6 wt%, respectively. It was found that using raw PSA as a source of Si and Al resulted in the formation of Hydroxysodalite-type zeolite, while using the leached PSA led to the synthesis of zeolite-P. This indicated that the reduction in Ca and Mg content and the increase in Si and Al concentrations played a significant role in zeolite synthesis. In a similar study, Sugano et al. (2005) synthesized two blast furnace slag samples resembling industrial-type blast furnace slag (SiO_2 = 32.4 wt.%, Al_2O_3 = 27.6 wt.% and CaO = 40.0 wt.%) and leached slag (SiO_2 = 46.0 wt.%, Al_2O_3 = 39.0 wt.% and CaO 15.0 wt.%). The products obtained from the raw slag were inorganic minerals (hydrogarnet and tobermorite), while the leached slag formed zeolite A. This demonstrates that the composition of CaO and MgO in the feedstock significantly influences the type of product obtained, whether it be an inorganic mineral compound or a zeolitic material. The chemical makeup of blast furnace slag makes it a suitable candidate for zeolite synthesis. However, the pretreatment stage is often necessary to achieve the desired product (Kuwahara et al., 2008; Murakami et al., 2011).

Table 3.3. Chemical composition of BFS.

Compound		SiO_2	Al_2O_3	Fe_2O_3	MnO	MgO	CaO	Na_2O	K_2O	TiO_2	P_2O_5	Cr_2O_3
Blast Furnace Slag (wt.%)		35.1	16.1	2.33	0.93	**10.5**	**30.6**	0.23	1.05	2.55	0.02	0.03
Pre-treated slag (wt.%)	*Run 2*	42.3	19.7	1.13	0.21	**8.1**	**21.8**	0.02	0.08	0.78	0.02	0.02
	Run 10	53.4	4.46	0.75	0.11	**2.54**	**4.83**	0.07	0.27	0.57	0.01	0.21

3.3.4. X-ray Diffraction Patterns of Powdered Samples

Zeolitic porous materials were successfully synthesized using the hydrothermal method. This involved using a 3M NaOH solution to dissolve Si and Al, forming a synthetic gel. Two precursors, BFS and PTS, were used as Si and Al sources, allowing for a comprehensive comparison. The gel, rich in Si and Al, underwent hydrothermal treatment under specific conditions, that is, crystallization temperature and time of 200°C and 13 h, respectively. ***Figure 3.3*** presents the XRD patterns of the raw slag (BFS) and the leached slag (PTS), along with their derived products, which provide valuable insight into the changes in their crystalline structures. The analysis revealed that the BFS used in this study contained akermanite ($Ca_2Al_{0.99}Mg_{0.46}Si_{1.52}O_7$), a mineral commonly found in Ca- and Mg-rich silicate slags from the iron and steel industry (Chukwuma et al., 2021). The melilite group, to which akermanite belongs, was confirmed as part of the crystalline mineral group present in the BFS. This observation was further supported by the substantial amounts of CaO (30.6 wt.%) and MgO (10.5 wt.%) detected in the BFS (***Table 3.3***). Additionally, the unidentified diffraction peaks observed can be attributed to other complex aluminosilicate minerals.

The XRD pattern of the PTS is shown in ***Figure 3.3b***. Augite [$Ca(MgFeAl)(Si_2Al_2)O_6$] was identified as the mineral phase present in the PTS. The change in the mineral phase subsequent to the leaching process can be attributed to the amorphous nature of the slags, as shown by the compact background diffraction patterns observed at $2\theta < 25°$ (***Figure 3.3a and b***). The results indicate that akermanite transformed into a distinct mineral phase, namely augite, during the leaching process. The reduced

concentrations of CaO (4.83 wt.%) and MgO (2.54 wt.%) in the PTS lead to a shift in the crystalline structure, as denoted by the emergence of new diffraction peaks in ***Figure 3.3b***. Wajima and Ikegami (2008) conducted acid-leaching tests on paper sludge ash (PSA) to reduce the CaO composition to 19.0 wt.%. The mineral phases identified in the raw PSA were gehlenite ($Ca_2Al_2SiO_7$) and anorthite ($CaAl_2Si_2O_8$). Following leaching, the remaining mineral phase was determined to be anorthite. Hence, it is evident that the acid leaching of silicate slags rich in calcium and magnesium causes a transformation in the mineral phase.

Figure 3.3c shows the XRD patterns of the product derived from BFS. The crystalline mineral phase was identified to be augite [$Ca_{0.74}Fe_{0.087}(Mg_{0.016}Fe_{0.075})(Si_{1.5}Al_{0.5})O_6$]. It is important to note that while the augite in ***Figure 3.3b*** resulted from the leaching of BFS, the augite in ***Figure 3.3c*** was formed through the hydrothermal treatment of BFS. Although both figures showcase the same mineral phase, there is a notable difference in the composition of CaO and MgO. Augite, a crystalline mineral commonly found in steel slag, is primarily composed of SiO_2, Al_2O_3, CaO, and MgO. It is extensively utilized in the production of glass ceramics, which are polycrystalline composite materials (Deng et al., 2020). The production process involves a one-step heat treatment that encompasses nucleation and crystallization (Zhang et al., 2016). ***Figure 3.3d*** illustrates the XRD peaks of the product derived from PTS. The hydrothermal treatment of PTS resulted in the formation of a crystalline zeolite material. The zeolite phase observed was identified to be ZSM-5, although the presence of augite was still evident, as indicated by the two theta peaks at 30° and 36°. ZSM-5 is a microstructured zeolite that contains a three-dimensional tetrahedral aluminosilicate framework. It is widely employed in catalytic reactions to produce petrochemicals or the conversion of ethanol into a range of hydrocarbons. The diffractograms obtained highlighted that a high content of Ca and Mg in the slag significantly hinders the formation of zeolite during hydrothermal treatment.

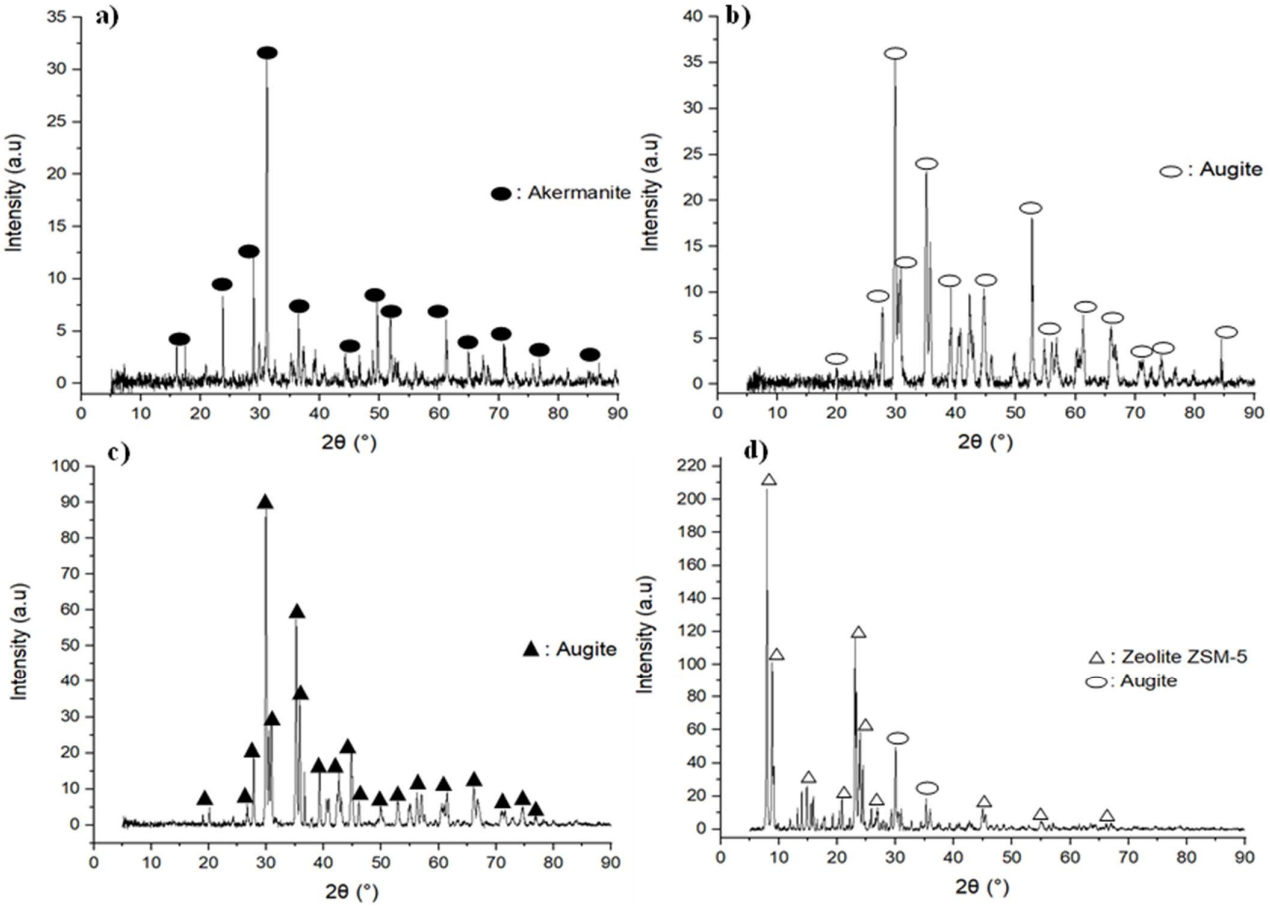

Figure 3.3. Powder X-ray diffractograms: a) Blast furnace slag [BFS], b) pretreat slag [PTS], c) product derived from BFS, and d) product derived from PTS.

3.3.5. Scanning Electron Microscopy (SEM) Images of Powdered Samples

Figure 3.4 presents the corresponding micro-images of the raw slag (BFS), the leached slag (PTS), and their corresponding synthesized products. The corresponding EDS elemental data for the powered samples are shown in *7.1* Appendix A (Acid Leaching Experiments). In ***Figure 3.4a*** **and** ***b***, the micro-images depict an amalgamation of bulky, irregularly shaped stonelike formations with diverse particle sizes and fibrous surfaces. These distinct characteristics can be attributed to the amorphous composition of the powdered samples before and after the leaching process. The morphology of BFS used by Yong et al. (2021) was characterized by non-homogenous bulky particles with sharp edges and subangular and subrounded shapes. The surface was reported to consist of fibrous structures containing detrital grains. ***Figure 3.4c*** **and** ***d*** present the micrographs of the products derived from BFS and PTS, respectively. Most of the particles in ***Figure 3.4c*** had large irregular stonelike morphologies (like in ***Figure 3.4b***) with small rectangular-shaped prism crystals. The morphology observed in ***Figure 3.4c*** exhibited micro-sized rectangular prisms formed by stacked sheets of flat crystals. However, it was observed that BFS was unable to produce a zeolitic material. The morphology observed in ***Figure 3.4d*** displayed agglomerated ball-shaped crystals with uneven surfaces. The average particle sizes in ***Figure 3.4c*** **and** ***d*** were 20 and 8 μm, respectively. The leached slag resulted in the formation of ZSM-5 crystals, but only in the form of ball-shaped crystals. Jiang et

al. (2022) synthesized ZSM-5 catalysts with various morphologies (spherical-like, flat sheet-like, and brick-like) for the combustion of toluene. The diverse morphologies were achieved by varying the crystallization conditions; that is, spherical-like crystallized at 24 h and 150°C, and flat sheet-like and brick-like were crystallized at 72 h and 180°C.

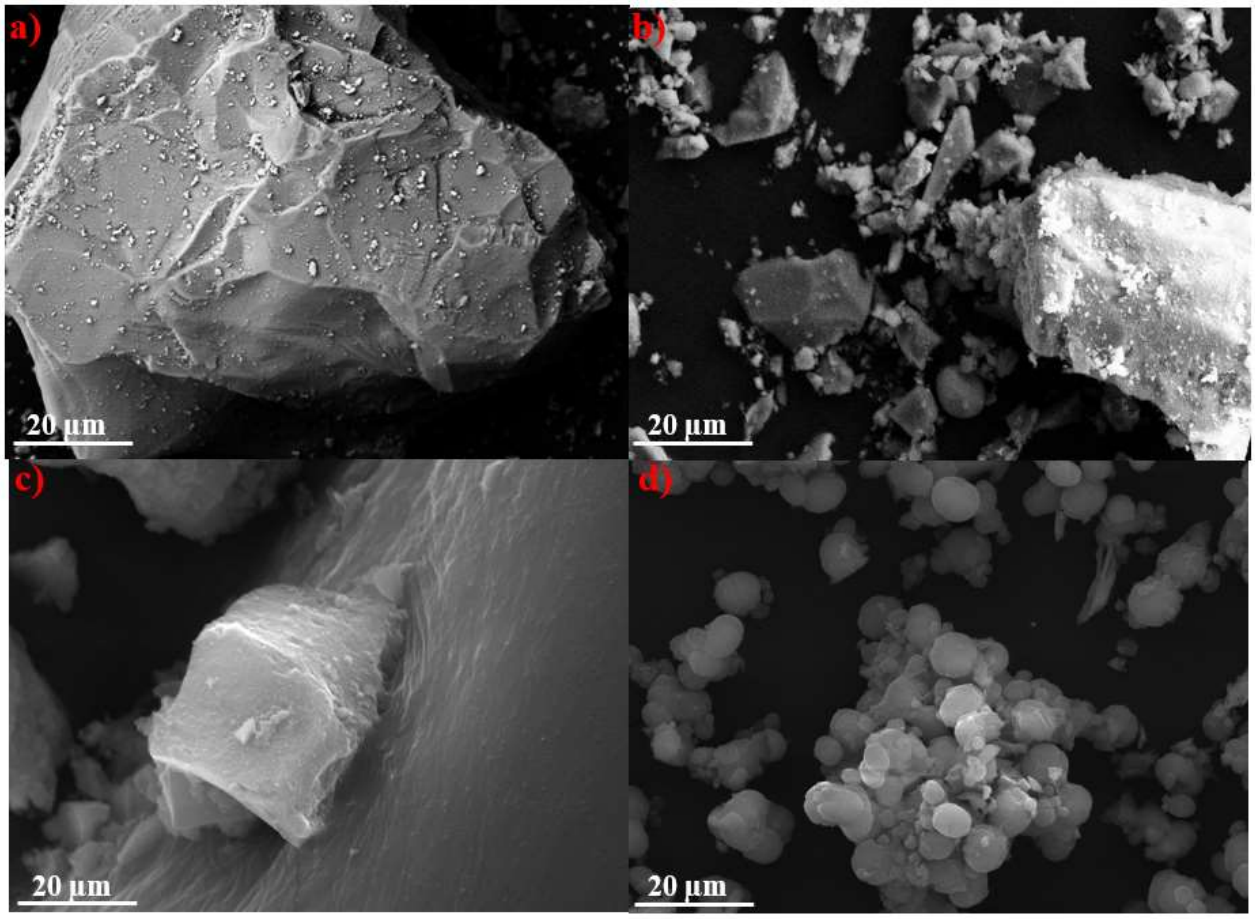

Figure 3.4. SEM micrographs: a) BFS, b) PTS, c) product synthesized from BFS, and d) product synthesized PTS.

3.3.6. Fourier-Transform Infrared Spectroscopy (FTIR)

Figure 3.5 shows the mid-FTIR spectra and the corresponding wavenumbers of the synthesized ZSM-5 against the commercial ZSM-5. The 426 and 546 cm^{-1} absorption bands indicate the tetrahedral (SiO_4 and AlO_4) bending vibration and the formation of the double five ring (D_5R) by the tetrahedral (SiO_4 and AlO_4) units. The D_5R is characteristic of the MFI-type zeolite structure. Furthermore, the area ratio of these absorption bands (426 and 546 cm^{-1}) can be used to confirm the zeolite structure (Kim & Chung, 2003). The absorption band at 798 cm^{-1} was attributed to the T−O−T (T = Si and Al atoms) internal symmetrical stretching bond. The 1075 and 1224 cm^{-1} absorption bands are characterized by external asymmetrical stretching and asymmetric stretch vibrations, respectively. The absorption bands in the synthesized ZSM-5 are comparable to those found in the commercial ZSM-5 and mentioned in the literature (Gurdal & Yasar, 2023; Prabhu et al., 2022; Salim & Saed, 2023).

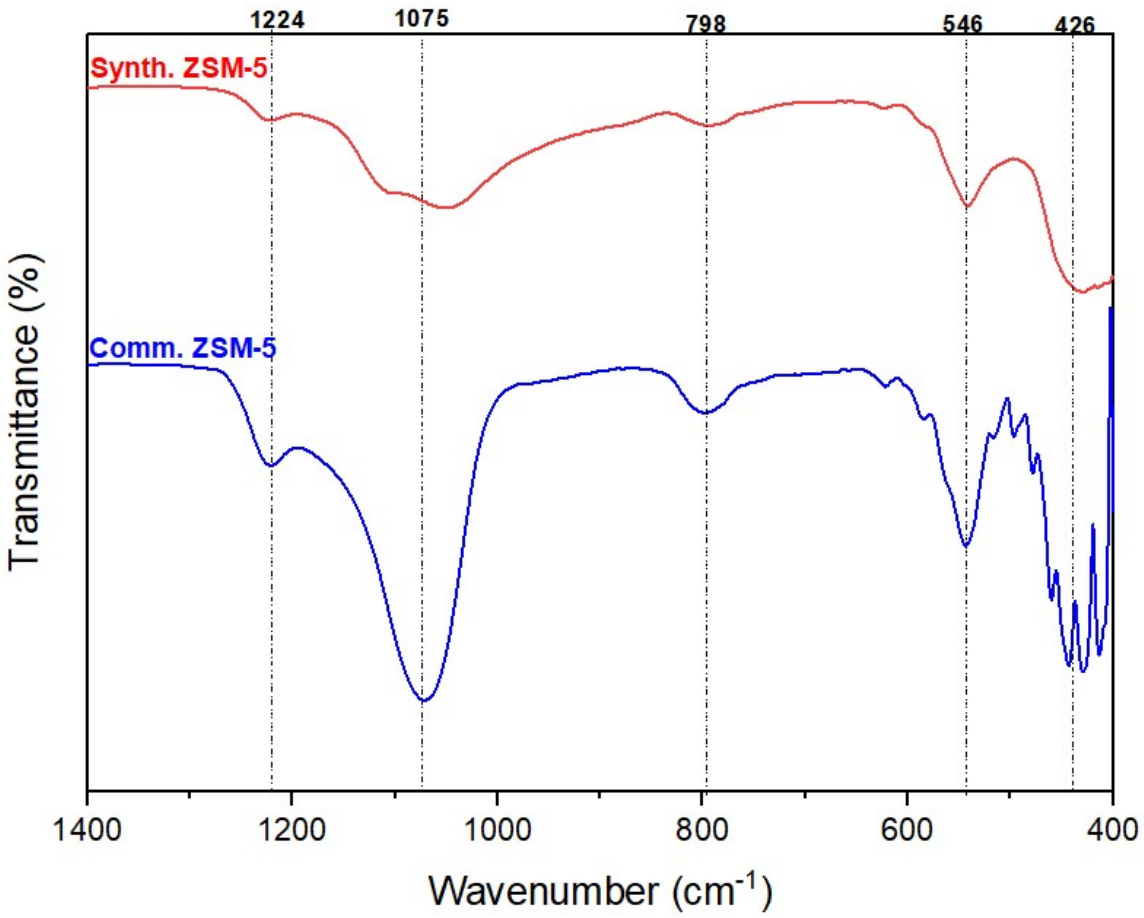

Figure 3.5. FTIR spectra of powdered products.

3.4. Conclusion

The successful investigation of Ca and Mg removal from blast furnace slag via a series of acid-leaching tests was carried out to assess the leaching conditions needed to enhance the synthesis of zeolite ZSM-5 from waste slag. The study revealed that the acid-leaching process effectively solubilized Ca and Mg. The resulting pretreated slag contained the main components (53.4 wt.% SiO_2 and 4.45 wt.% Al_2O_3) for ZSM-5 synthesis, along with trace metal elements. The optimal leaching conditions were determined to be a leaching time of 90 min, an acid concentration of 3 mol/L, and a solids concentration of 8 wt.%. These conditions allowed for a maximum leaching efficiency of 80.4% for Ca and 71.1% for Mg. Consequently, the pretreatment of BFS utilizing these specific leaching conditions significantly reduced the composition of CaO and MgO in the PTS to 4.83 wt.% and 2.54 wt.%, respectively. Subsequently, zeolite ZSM-5 was successfully synthesized using the pretreated slag as a Si and Al precursor. The acid leaching of BFS significantly reduced the impurities, thus leading to an improved hydrothermal synthesis method. However, the altered mineral phase and the formation of ball-shaped zeolite crystals suggest the necessity for further investigation and optimization of the synthesis process.

References

Chen, J., Xing, Y., Wang, Y., Zhang, W., Guo, Z., & Su, W. (2022). Application of iron and steel slags in mitigating greenhouse gas emissions: A review. *Science of The Total Environment*, *844*, 157041.

Chukwuma, J. S., Pullin, H., & Renforth, P. (2021). Assessing the carbon capture capacity of South Wales' legacy iron and steel slag. *Minerals Engineering*, *173*, 107232.

Deng, L., Yun, F., Jia, R., Li, H., Jia, X., Shi, Y., & Zhang, X. (2020). Effect of SiO2/MgO ratio on the crystallization behavior, structure, and properties of wollastonite-augite glass-ceramics derived from stainless steel slag. *Materials Chemistry and Physics*, *239*.

Duan, W., Wang, D., Wang, Z., & Yu, Q. (2022a). Hydrometallurgical Leaching Behavior and Kinetic Modeling of Blast Furnace Slag in Hydrochloric Acid. *Journal of Sustainable Metallurgy*, *8*(1), 170–185.

Duan, W., Wu, Q., Li, P., & Cheng, P. (2022b). Techno-economic analysis of a novel full-chain blast furnace slag utilization system. *Energy*, *242*, 123049.

Gurdal, S., & Yasar, M. (2023). Dimethyl ether synthesis on clinoptilolite zeolite and HZSM5-based hybrid catalysts in a fixed-bed reactor. *International Journal of Hydrogen Energy*, *48*(60), 22978–22987.

Hunter, J. G., & Kang, D. H. (2022). Bioreactor media for treatment of slag leachate. *Chemosphere*, *308*, 136319.

Jiang, Z., Chen, D., Deng, W., & Guo, L. (2022). Different morphological ZSM-5 zeolites supported Pt catalysts for toluene catalytic combustion. *Chemical Physics Impact*, *5,* 100134.

Kim, D. J., & Chung, H. S. (2003). Synthesis and characterization of ZSM-5 zeolite from serpentine. *Applied Clay Science*, *24*(1–2), 69–77.

Kuwahara, Y., Ohmichi, T., Kamegawa, T., Mori, K., & Yamashita, H. (2009). A novel synthetic route to hydroxyapatite–zeolite composite material from steel slag: investigation of synthesis mechanism and evaluation of physicochemical properties. *Journal of Materials Chemistry*, *19*(39), 7263–7272.

Kuwahara, Y., Ohmichi, T., Mori, K., Katayama, I., & Yamashita, H. (2008a). Synthesis of zeolite from steel slag and its application as a support of nano-sized TiO_2 photocatalyst. *Journal of Materials Science*, *43*(7), 2407–2410.

Lee, Y. H., Eom, H., Lee, S. M., & Kim, S. S. (2021). Effects of pH and metal composition on selective extraction of calcium from steel slag for $Ca(OH)_2$ production. *Royal Society of Chemistry (RSC) Advances*, *11*(14), 8306–8313.

Li, G., Li, M., Zhang, X., Cao, P., Jiang, H., Luo, J., & Jiang, T. (2022). Hydrothermal synthesis of zeolites-calcium silicate hydrate composite from coal fly ash with co-activation of Ca(OH)2-NaOH for aqueous heavy metals removal. *International Journal of Mining Science and Technology*, *32*(3), 563–573.

Liu, Y., Lin, Q., Li, L., Fu, J., Zhu, Z., Wang, C., & Qian, D. (2014). Study on hydrometallurgical process and kinetics of manganese extraction from low-grade manganese carbonate ores. *International Journal of Mining Science and Technology*, *24*(4), 567–571.

Meng, L., Qu, J., Guo, Q., Xie, K., Zhang, P., Han, L., Zhang, G., & Qi, T. (2015). Recovery of Ni, Co, Mn, and Mg from nickel laterite ores using alkaline oxidation and hydrochloric acid leaching. *Separation and Purification Technology*, *143*, 80–87.

Murakami, T., Sugano, Y., Kinami, T., Narushima, T., Iguchi, Y., & Ouchi, C. (2011). Alkali Hydrothermal Synthesis of Zeolite A Using Oxide By-products. *Iron and Steel Institute of Japan (ISIJ) International*, *51*(1), 158–165.

Ojha, P., Singh, A., Singh, B., Sen, S., & Kumar, R. (2023). Studies on Portland Slag Cement Made Using Blast Furnace and Linz-Donawitz Slag. *ACI Materials Journal*, *120*(1), 143–154.

Prabhu, S., Elumalai, N., Selvaraj, M., Harish, S., Ramesh, R., Silambarasan, A., Navaneethan, M., & Ramu, P. (2022). Synthesis and characterization of CeO2 supported ZSM-5 zeolite for organic dye degradation. *Journal of Materials Science: Materials in Electronics*, *33*(12), 9211–9223.

Raaleka, T. I. (2017). *The sustainability of the steel industry in South Africa* [MBA Thesis]. Johannesburg (RSA): University of the Witwatersrand, Available at: https://hdl.handle.net/10539/23901 (Accessed: 05 May 2023).

Salim, M. A. R., & Saed, U. A. (2023). Production of High-Octane Number Gasoline from Basra Low Octane-Number Gas Condensate and Ethanol over Modified Zn/ZSM5 Zeolite Catalyst. *Bulletin of Chemical Reaction Engineering and Catalysis*, *18*(1), 59–70.

Sugano, Y., Sahara, R., Murakami, T., Narushima, T., Iguchi, Y., & Ouchi, C. (2005). Hydrothermal synthesis of zeolite a using blast furnace slag. *ISIJ International*, *45*(6), 937–945.

Vigil de la Villa Mencía, R., Goiti, E., Ocejo, M., & Giménez, R. G. (2020). Synthesis of zeolite type analcime from industrial wastes. *Microporous and Mesoporous Materials*, *293*, 1–9.

Wajima, T., & Ikegami, Y. (2008). Zeolite synthesis from paper sludge ash via acid leaching. *Chemical Engineering Communications*, *195*(3), 305–315.

Wang, Z., Feng, Z., Yang, L., & Wang, M. (2021). Effective removal of calcium and magnesium ions from water by a novel alginate–citrate composite aerogel. *Gels*, *7*(3), 125.

Yong, H. C., Ween, O. S., Ming, L. Y., Abdullah, M. M. A. B., & En, O. W. (2021). Development of Ash-Based and Slag-Based Pressed Geopolymer. *Sustainable Waste Utilization in Bricks, Concrete, and Cementitious Materials, 129*, 51–72.

Zhang, S., Yang, J., Liu, B., Pan, D., Wu, C., & Volinsky, A. A. (2016). One-step Crystallization Kinetic Parameters of the Glass-ceramics Prepared from Stainless Steel Slag and Pickling Sludge. *Journal of iron and steel research*, *23*(3), 220–224.

Zhang, X., Matsuura, H., & Tsukihashi, F. (2012). Dissolution Mechanism of Various Elements into Seawater for Recycling of Steelmaking Slag. *Iron and Steel Institute of Japan (ISIJ) International*, 52(5), 928–933.

CHAPTER 4

4. SYNTHESIS AND CHARACTERIZATION OF ZEOLITE-BASED CATALYST DERIVED FROM SLAG WASTE

Research paper under review.

Abstract

A rapid hydrothermal synthesis method was employed to prepare a novel Zeolite Socony Mobil-5 (ZSM-5) material impregnated with intrinsic metal alloys (Fe_2O_3, MnO, TiO_2, Cr_2O_3, and NiO). Green chemistry was paired with the synthesis method by utilizing microwave irradiation as a heat source and blast furnace slag as a SiO_2 and Al_2O_3 precursor. The synthesis temperature and time were varied to explore their effects on the physicochemical, textural, and structural properties of the synthesized ZSM-5 products. Commercial ZSM-5 was used as a reference sample. Pretreatment of the raw slag through acid leaching significantly reduced from 29.15 wt. % and 8.57 wt.% to 3.48 wt.% and 1.54 wt.% for CaO and MgO, respectively. The maximum synthesis conditions were found to be 180°C and 13h. The maximum conditions produced a crystalline ZSM-5 product of well-defined cubic prism shapes with microsized intergrown rectangular crystals. The synthesized ZSM-5 has a mesoporous structure with a relative crystallinity of 52.4% and a relatively low specific surface area (108.4 m^2/g) compared to the reference sample (436.4 m^2/g). This was attributed to the presence of trace metals occupying the mesopores. Conclusively, the synthesis temperature strongly affected the crystal size, while the synthesis time affected the morphology. However, neither the synthesis temperature nor the time affected the chemical composition of the products. The use of microwave irradiation significantly reduced the synthesis time. ZSM-5 was successfully synthesized from waste slag using microwave-assisted synthesis.

4.1. Introduction

Zeolite Socony Mobil-5 (ZSM-5) is one of the most sought-after synthetic zeolites that belongs to the Mobil Five (MFI) crystalline structural group and is widely used as an industrial catalyst to promote reactions such as cracking, alkylation, isomerization, and oligomerization (Tung et al., 2012). The three-dimensional crystalline framework in ZSM-5 consists of Si and Al atoms that are tetrahedrally coordinated to form 8-membered and 10-membered rings. The rings are interconnected to form channels and pores. The centrally located atoms (Si and Al) are surrounded by and connected through their shared oxygen atoms, resulting in balanced (SiO_4) and imbalanced (AlO_4^-) ions. The net negative charge is compensated by introducing an extra cation (Na^+, Mg^{2+}, Ca^{2+}, K^+, or H^+) into the tetrahedral units (AlO_4^-). Metallic components can exist in different forms inside the synthesized zeolite. That is, (*1*) a stable ionic bond can be achieved by metal ions that are directly integrated within the tetrahedral framework (Derbe et al., 2021), (*2*) certain metals within the tetrahedral network may present as exchangeable cations due to the porous nature of zeolite (Eren et al., 2024), and (*3*) in some cases, metal ions can be deposited on the zeolite pores and aggregate to form small clusters of amorphous oxides (Zhang et al., 2023). The physicochemical properties that make ZSM-5 attractive to industrialists are its cation exchange capacity (CEC), chemical composition, pore diameter, and channel length (Liu et al., 2019). Zeolites are ranked from low-silica zeolites (Si/Al < 2) to high-silica zeolites (Si/Al > 5), and the ranking is based on the Si/Al molar ratio. ZSM-5 is considered a high-silica zeolite, and its chemical composition is used to manipulate properties such as hydrophobicity, thermal stability, catalytic reactivity, and acid resistivity (Jha & Singh, 2011). The uniform pore sizes and long channels found in ZSM-5 contribute to its catalytic activity and shape selectivity, thus enabling it to target compounds of specific shapes and sizes to be adsorbed or catalytically transformed. Regrettably, the narrow micropores (0.5 nm – 0.6 nm) prohibit bulky organic molecules from diffusing into the channels to access the active acidic sites, leading to coke formation, reduced catalytic activity, and catalyst deactivation (Wang et al., 2023). Attempts to address these drawbacks involved modifying the synthesis procedure, incorporating strategies such as metal doping, or creating larger pores (mesopores).

ZSM-5 is commonly synthesized using the conventional hydrothermal synthesis method, which involves heat treatment of an aluminosilicate gel in alkaline media under harsh and costly conditions. The gel mixture often consists of alumina and silica precursors, an alkali activator, and a structure-directing agent (SDA). Several studies have noted the lack of green chemistry in the hydrothermal synthesis method. Furthermore, the method has been criticized for the feedstock used, harsh synthesis conditions, extensive energy requirements, and prolonged reaction periods. A structure-directing agent (organic template) aims to achieve the desired pore size and framework topology. However, the SDA is often organic and is removed by heat treatment, which releases harmful gasses (Zhang et al., 2022). Parnham and Morris (2006) noted safety concerns that might arise due to the high autogenous pressure that develops during nucleation and crystallization. Moreover, the efficiency of the hydrothermal synthesis method is reduced by operating at elevated temperatures (80–200°C) for extended periods (1–24 days). This significantly increases the energy requirements of the process (Meng & Xiao, 2014). Recent zeolite synthesis studies have focused on addressing the shortfalls in the hydrothermal synthesis process. These include but are not limited to replacing the organic template (SDA) with a seed-assisted synthesis method (Han et al., 2019), avoiding autogenous pressure by using the solvent-free synthesis route (Wu et al., 2014), and using aluminosilicate-rich industrial wastes as feedstock

(Liu et al., 2019). ZSM-5 obtained from these green synthesis studies has been reported to have improved crystallinity, textural properties, and catalytic reactivity. Furthermore, the synthesis methods have significantly reduced the synthesis time, produced less harmful gasses, and decreased energy requirements.

Using blast furnace slag (BFS) as a silicon and aluminum precursor has been reported as a promising technique for coupling green chemistry with the hydrothermal synthesis method (Kumar et al., 2020). This is due to the fact that blast furnace slag is a waste byproduct generated by the iron- and steel-making industry and mainly consists of SiO_2 and Al_2O_3 along with impurities (mostly CaO and MgO). Using BFS as a source of SiO_2 and Al_2O_3 could make the synthesis method innovative and environmentally friendly while reducing overall costs. However, the slag's fluctuating mineral and chemical compositions (impurities) significantly affect the purity of the final product (zeolite). Therefore, beneficiation of BFS mitigates the presence of impurities. It can be achieved by pretreatment of the slag through acid leaching (Mohiuddin et al., 2016). Another technique for making the hydrothermal synthesis method a greener chemistry process is using microwave radiation as an energy source. Microwave energy is an efficient heating method due to the heating mechanisms used. That is, an alternating magnetic and electric field is propagated, and it penetrates the sample, thus heating it from the inside out (Morgan et al., 2017). The benefits of using the microwave-assisted synthesis method are the enhancement of reaction rates, reproducibility of the radiation field, and high product yield and purity (Kumar et al., 2020). Furthermore, microwave energy accelerates the nucleation of the initial crystals, resulting in the rapid and consistent growth of the crystals. This leads to a product (ZSM-5) with uniform textural properties (pore size and channels) and versatile composition [Si/Al ratio] (Meng & Xiao, 2014).

Therefore, this communication seeks to enhance a microwave-assisted hydrothermal synthesis method by coupling it with green chemistry processes. This was achieved by employing the microwave-assisted hydrothermal synthesis method to produce a novel ZSM-5 zeolite impregnated with intrinsic metal alloys (Fe_2O_3, MnO, TiO_2, Cr_2O_3, and NiO). Furthermore, blast furnace slag, a waste material from the iron- and steel-making industry, was used as an aluminosilicate precursor. The secondary use of waste slag has the advantages of valorization and resource management. The BFS was initially beneficiated using acid leaching to extract Ca and Mg from the slag. The pretreated slag was combined with an alkaline activator and an organic template to create the synthetic gel mixture. A laboratory-scale microwave system was used to supply microwave energy to control the nucleation and crystallization processes during synthesis. Furthermore, the synthesis conditions, such as the synthesis time and temperature, were investigated systematically. The synthesized ZSM-5 was characterized to determine its structural properties and morphology.

4.2. Materials and Methods

4.2.1. Chemical and Materials

Blast furnace slag was obtained from the iron and steel-making industry in South Africa. The reagents used for the preparation of the synthesis gel were tetrapropylammonium bromide (TPABr, 98% purity), sodium hydroxide pellets (NaOH, 98% purity), and sulfuric acid (H_2SO_4, 98% purity). Hydrochloric acid (HCl, 32% purity) beneficiated the raw slag. Commercial ZSM-5 (99.5% purity) was used as the reference zeolite. The chemicals and materials used in this study were obtained from

local South African suppliers and used as received. Deionized water was used to prepare all the solutions and was obtained from a Milli-Q® water purification system.

4.2.2. Blast Furnace Slag Beneficiation

Acid leaching was employed as a pretreatment step to remove impurities (CaO and MgO) and make the slag more suitable for zeolite synthesis. The raw slag was crushed, milled, and screened to a fine particle size passing through a 100 µm sieve and represented as BFS. The prepared BFS was acid-leached using a 3M HCl solution at 60°C for 90 minutes (according to *section 3.2.2*). Subsequently, the leached material was separated from the leachate by gravity filtration, washed with deionized water, air-dried, and ground to prepare pretreated slag (PTS). PTS was used as an aluminosilicate precursor for the synthesis experiments. A detailed description of the pretreatment process, as well as the characterization of the raw and pretreated slags, is available in Nyembe & Isa (2025).

4.2.3. Microwave-assisted Hydrothermal Synthesis

The conversion of BFS to zeolite ZSM-5 was achieved using a microwave-assisted hydrothermal synthesis technique (***Figure 4.1***). This implies that microwave irradiation was used to crystallize the synthesis gel. Calculated amounts of PTS and NaOH were dispersed in deionized water to form suspension 1. Concurrently, TPABr was dissolved in deionized water to form solution 2. Both mixtures were individually stirred and heated to achieve homogeneity. Subsequently, solution 2 was slowly added to suspension 1 while heating (80°C) and stirring (225 rpm) continued for 30 min. The pH level of the resulting mixture was adjusted to 9.0 using H_2SO_4, and a gel mixture was obtained using the following chemical composition:

$$\mathbf{21.7SiO_2 : 3.45Al_2O_3 : 0.75Na_2O : 1.00TPABr : 2225.38H_2O}$$

The gel mixture was then transferred into modified Teflon reaction vessels with a maximum capacity of 50 mL. The reaction vessels were then placed inside the microwave cavity and heated, using microwave irradiation, to 90°C, 120°C, 150°C, 180°C and 200°C and the heating was performed for 5, 7, 9, 11, and 13 h under autogenous pressure. After crystallization, the products were filtered, washed to a neutral pH level, and oven-dried at 90°C for 24 hours. The resulting solids were calcined at 550°C for 5 h to remove the structure-directing agent (TPABr) and produce Na-ZSM-5.

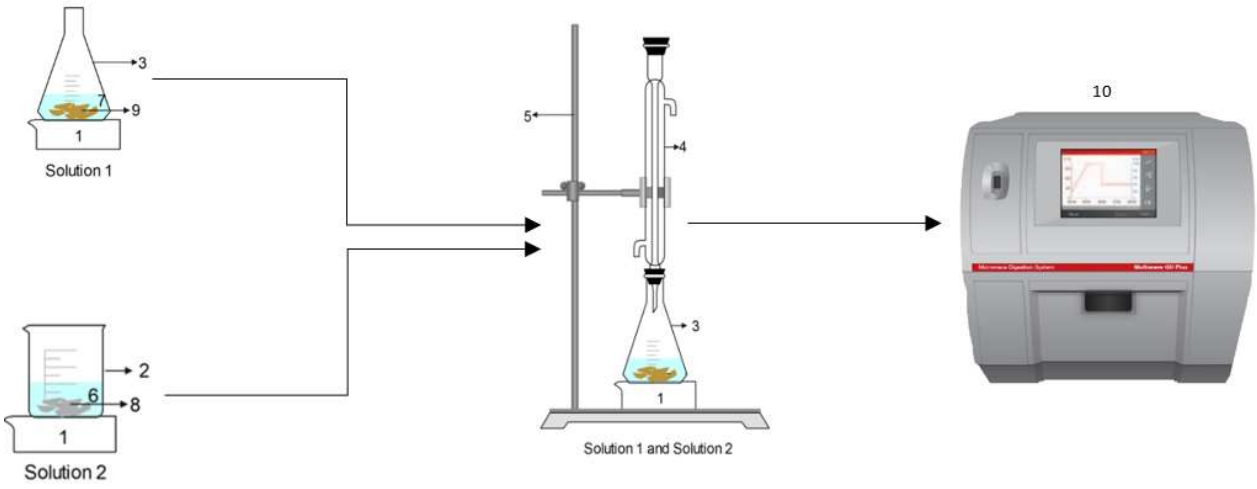

Figure 4.1. Hydrothermal synthesis process. 1) heating-magnetic stirring plate, 2) glass beaker, 3) flat-bottomed flask, 4) glass condenser, 5) clamp stand, 6) deionized water, 7) deionized water and NaOH solution, 8) TPABr, 9) pretreated slag, and 10) microwave system.

4.3.4. Characterization Methods

An X-ray fluorescence (XRF) spectrometer was used to determine the chemical compositions of all the powered samples (BFS, PTS, synthesized ZSM-5, and commercial ZSM-5). The Norrish Fusion technique and an X-ray spectrometer were used to analyze at 50 kV and 50 mA. Major elements were fused using the Johnson Matthey Spectrolflux from 105 to 1000°C, and the raw data were corrected using in-house software. The powdered samples' X-ray diffraction (XRD) patterns were obtained using a Bruker D2 Phaser powder X-ray analyzer. The instrument consisted of CuK_α tubes (λ = 1.5418 Å), and the data was recorded at a 2θ working range of 5 – 90° at 40 kV. The step increment was maintained at 0.026°/2θ and a counting time of 0.2 s per step. Semi-quantitative analysis of the powders was performed using custom software, which quantified the mineral phases in each sample. The sample's microstructures (morphology and size) were observed using a high-resolution Tescan Vega scanning electron microscope (SEM). During the analysis, the working distance was maintained between 10 and 15 mm, and the accelerating voltage was set to 5 kV. All samples were coated with carbon and Au/Pd before imaging. Fourier transform infrared spectroscopy (FT-IR) measurements were conducted using a PerkinElmer spectrometer at room temperature after background correction. The sample was placed on the ATR diamond crystal and secured by setting the force gauge to 60 (arbitrary units). It ensured good contact between the diamond crystal and the sample. The infrared spectra were recorded in the 400 – 4000 cm^{-1} region with a resolution of 4 cm^{-1}. The textural and structural properties (pore size, specific surface area, and pore volume) of all powdered samples were determined from N_2 adsorption/desorption isotherms collected at –196°C using a Quantachrome Autosorb iQ3 instrument (Anton Paar, USA). The samples were degassed under vacuum for 3 hours at 300°C. The Brunauer-Emmett-Teller (BET) is used to calculate theory calculates the specific surface area (S_{BET}). The micropore volume (V_{micro}) was determined by using the *t*-plot method. The total pore volume (V_{tot}) was computed at a relative pressure (p/p_0) of 0.98. The

adsorption branch of isotherms was used to derive the Barrett-Joyner-Halenda (BJH) model, which was applied to evaluate the mesopore size distributions.

4.3. Results and Discussion

4.3.1. Slag Beneficiation

The chemical compositions of BFS and PTS are presented as oxides in ***Table 4.1***. The main components found in BFS were SiO_2 (40.98 wt.%), Al_2O_3 (14.51 wt.%), MgO (8.57 wt.%), and CaO (29.15 wt.%). These reflect the common metals in waste slag generated by the iron- and steel-making industry. Acid leaching of the BFS effectively reduced the concentration of impurities (MgO and CaO). However, a significant amount of Al_2O_3 was equally removed. The concentrations of CaO, MgO, and Al_2O_3 in the PTS were reduced to 3.48, 1.54, and 5.85 wt.%, respectively. This was due to the reactivity of the components to form aqueous mineral salts ($CaCl_2$, $MgCl_2$, and $AlCl_3$), and our findings agree with those of Duan et al. (2022). The resulting beneficiated slag (PTS) consisted of a high amount of SiO_2 (55.23 wt.%) and a low amount of Al_2O_3 (5.85 wt.%). As shown in ***Table 4.1***, the Si/Al molar ratio increased from 2.4 (BFS) to 8.0 (PTS) due to the significant reduction in Al_2O_3. The beneficiation process removed 59.7% of Al_2O_3.

Anuwattana et al. (2008) used acid-leached cupola slag, a waste generated by an iron smelting process, to produce ZSM-5. The slag mainly consisted of SiO_2 (70.1 wt.%), Al_2O_3 (18.9 wt.%), MgO (1.3 wt.%), and CaO (3.3 wt.%). The acid-treated slag resulted in an oxide composition of 90.2 wt.% (SiO_2), 5.1 wt.% (Al_2O_3), 0.9 wt.% (MgO), and 2.8 wt.% CaO). The acid leaching tests significantly reduced the composition of CaO and MgO, however, a considerable amount (73%) of Al_2O_3 was removed. A similar phenomenon was observed by Duan et al. (2022), who investigated the acid-leaching kinetics of blast furnace slag using hydrochloric acid. The waste slag consisted of SiO_2 (34.85 wt.%), Al_2O_3 (10.99 wt.%), MgO (8.42 wt.%), and CaO (42.21 wt.%). However, 97.3% of Al_2O_3 was removed during leaching. It has been reported that Ca^{2+}, Mg^{2+}, and Al^{3+} species are highly reactive to Cl^- ions. In contrast, studies involving the acid leaching of paper sludge ash have shown minimum removal of Al_2O_3 during acid treatment (Wajima & Ikegami, 2008). Paper sludge ash is an industrial waste generated while manufacturing paper products. It mainly comprises SiO_2 (43.0 wt.%), Al_2O_3 (28.3 wt.%), MgO (7.62 wt.%) and CaO (19.0 wt.%). In Wajima and Ikegami (2008), only 9.54% of Al_2O_3 was removed during leaching.

Table 4.1. Chemical analysis of BFS and PTS as determined by XRF.

Compound	SiO_2	Al_2O_3	CaO	MgO	Fe_2O_3	MnO	Na_2O	K_2O	TiO_2	P_2O_5	Cr_2O_3	NiO	Si/Al ratio
Blast Furnace Slag (wt.%)	40.98	14.51	**29.15**	**8.57**	2.18	0.84	0.25	1.14	0.65	0.02	0.10	0.06	2.4
Pre-treated slag (wt.%)	55.23	5.85	**3.48**	**1.54**	0.70	0.03	0.03	0.04	0.90	0.02	0.01	0	8.0

4.3.2. Diffraction Patterns of the Synthesized Products

Synthesis conditions such as crystallization time and temperature are crucial for controlling the crystallinity and purity of ZSM-5. ***Figure 4.2*** shows the X-ray diffractograms of the synthesized

products. Commercial (comm.) ZSM-5 was used as a reference sample, as shown in ***Figure 4.2a and b***—the characteristic peaks of comm. ZSM-5 are located in the 7.6 – 8.2° and 22.8 – 24.5° ranges and were used to establish the presence of ZSM-5 crystals in the synthesized products. The diffraction peaks observed at 30° and 36° were identified as those of augite [$Ca_{0.74}Fe_{0.087}(Mg_{0.016}Fe_{0.075})(Si_{1.5}Al_{0.5})O_6$] and were present in the synthesized products. These peaks were inherited from the pretreated slag, which comprised of augite. Augite is a crystalline mineral produced by the steel industry. It is mainly used to synthesize polycrystalline composite materials (such as glass ceramics) via heat treatment in the presence of nucleating agents (Deng et al., 2020).

Figure 4.2a shows the effect of crystallization time on the formation of ZSM-5 at a constant temperature of 180°C. The product obtained at a crystallization time of 5h consisted of a broad, narrow, and flat amorphous mineral phase corresponding to an aluminosilicate (17.6 – 26.5°). The ZSM-5 characteristic peaks (7.6 – 8.2° and 22.8 – 24.5°) began to form as the crystallization time was increased to 7h, and the peak intensity increased with an increase in crystallization time to 11h. At this point, the relative crystallinity was less than 17%, which implied incomplete crystallization of the amorphous pretreated slag (precursor). As the crystallization time was increased to 13h, the characterized peaks were well-resolved, and the relative crystallinity leaped to 52.4%. As a result, the maximum crystallization time was 13h. Liu et al. (2019) investigated the effect of crystallization time on the synthesis of ZSM-5 from natural clay. A significant jump in the relative crystallinity was observed between 3 and 6h, and well-resolved diffraction peaks were obtained at 7h, with the crystallinity reaching 88%. Therefore, the crystallization time is an essential parameter in controlling the crystallinity of the synthesized ZSM-5.

Figure 4.2b shows the effect of crystallization temperature on the formation of ZSM-5 at a constant synthesis time of 13h. Temperature plays a vital role in increasing the rate of nucleation and crystal growth during the synthesis. The products obtained at 90, 120, and 150°C crystallization temperatures displayed a prominent amorphous peak (7.2 – 26.1°) corresponding to an aluminosilicate mineral. The crystallization temperatures of 180 and 200°C produced ZSM-5 materials with 52.4 and 51.2% crystallinities, respectively. Mohiuddin et al. (2016) synthesized ZSM-5 from kaolin and investigated the effect of crystallization temperature. It was reported that a crystallization temperature of 120°C produced an amorphous aluminosilicate product, and the pure crystalline ZSM-5 was obtained at 150 and 190°C. Conclusively, the nucleation rate increased due to an increase in the crystallization temperature up to 180°C and began to decrease at 200°C, thus resulting in thermodynamically stable crystals of ZSM-5. Furthermore, the metastable phase of ZSM-5 is converted to more successive phases, which Ostwald's law of successive reactions can describe (Mohiuddin et al., 2016).

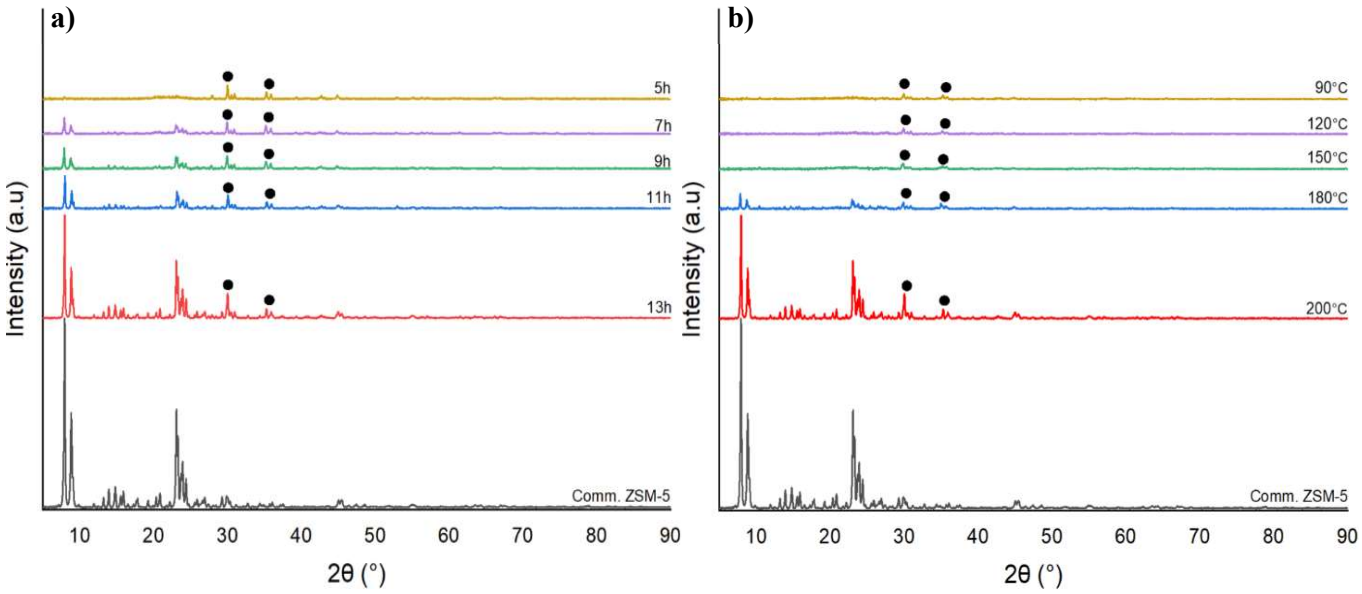

Figure 4.2. XRD patterns of the powered samples: a) Effect of synthesis time at 180°C, b) Effect of synthesis temperature at 13h, and (●) Augite mineral.

4.3.3. Morphology of the Synthesized Products

Figure 4.3 shows the crystal morphology and size of the products at different synthesis times. Commercial ZSM-5 was used as a reference sample and consisted of cubic prism shapes with small intergrown rectangular crystals. The product obtained after a synthesis time of 5h consisted of flat-thin sheets stacked to form a cubic prism. An increase in the synthesis time from 5 to 7h resulted in the appearance of a morphology similar to that of comm. ZSM-5. However, the surfaces of the crystals were unrefined and surrounded by irregular-shaped particles. The surfaces of the crystals developed to be more refined with increased synthesis time, resulting in well-refined cubic prism shapes with microsized intergrown rectangular crystals at a synthesis time of 13h. Furthermore, the average crystal size remained constant as the synthesis time was increased from 7 to 13h.

Jiang et al. (2014) converted clay mineral waste (palygorskite) into high siliceous ZSM-5 while varying the synthesis time (6 – 120h). Irregular, spherical, and cubic particles were obtained at 6, 12, and 24h, respectively. In addition, the particle size of the crystals remained unchanged as the synthesis time increased to 24h. Anuwattana et al. (2008) synthesized ZSM-5 from cupola waste slag and obtained octagonal prism shapes with twin intergrown crystals at 20 and 24h synthesis times. Like Jiang et al. (2014), they obtained spherical crystals at 12h. In comparison to Jiang et al. (2014), Liu et al. (2019) used a different clay mineral waste (hydromuscovite) to synthesize ZSM-5. The morphologies of the ZSM-5 products were found to be uniform hexagonal plate particles (at a synthesis time of 7h) with a constant crystal size.

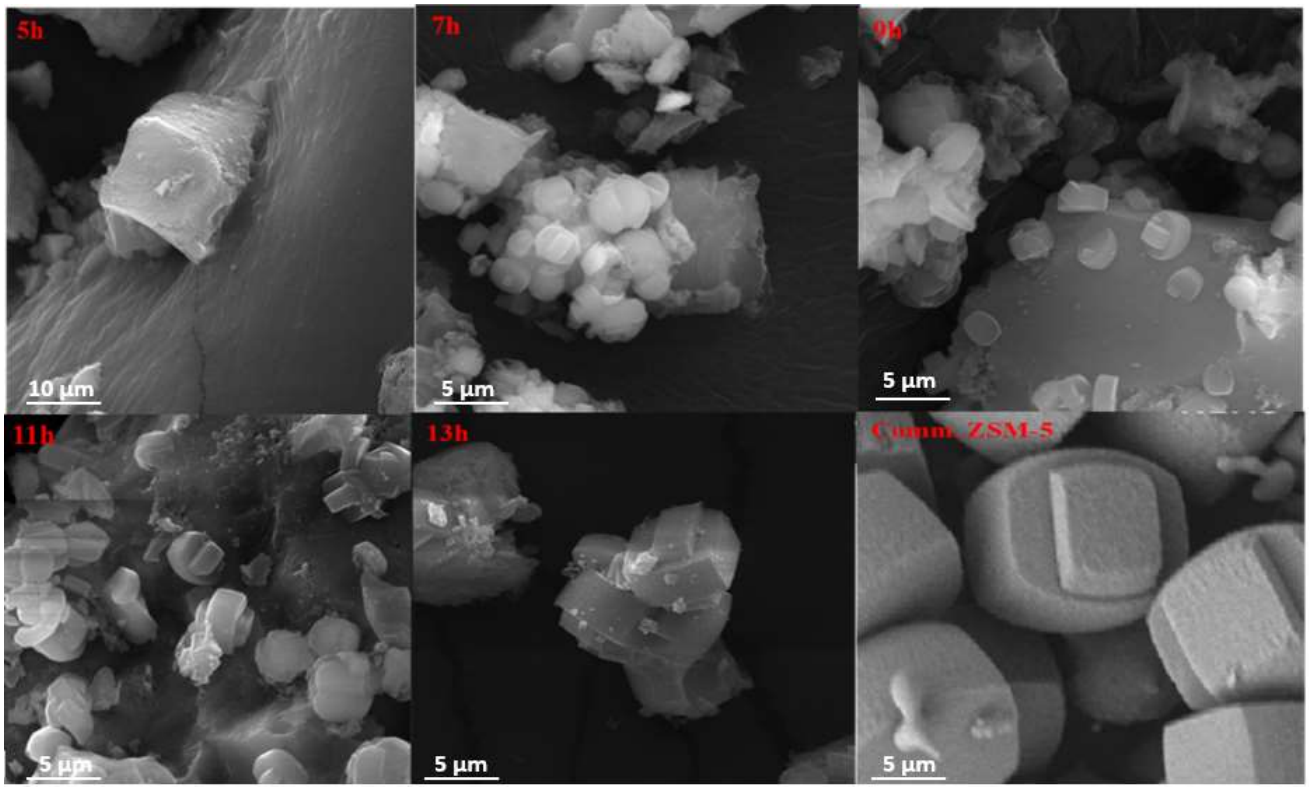

Figure 4.3. SEM micro-images of powered samples at different synthesis times at 180°C.

4.3.4. Framework Structure of Synthesized Products

The mid-FTIR spectra illustrating the lattice vibrational modes of the synthesized products are shown in ***Figure 4.4***. Due to the absence of functional groups (> 1500 cm^{-1}), only the fingerprint region (1400 – 400 cm^{-1}) was considered. The silanol (Si-OH) stretching vibrational band, which appears between 3400 and 3600 cm^{-1}, was undetected in all the synthesized products. In ***Figure 4.4a and b***, the reference sample (comm. ZSM-5) exhibited absorption bands at 1224 and 1075 cm^{-1}, characteristic of the external and internal TO_4 (T = Si and Al) asymmetric stretching vibrations, respectively. Moreover, the bands at 798, 546, and 426 cm^{-1} correspond to the internal vibrations of TO_4 symmetric stretching, distorted double five-membered rings, and TO_4 bending, respectively (Ahedi et al., 2001). The spectra of the synthesized products displayed the typical structure of comm. ZSM-5 with slight modifications due to the presence of trace metals (***Figure 4.4a and b***). Synthesis time and temperature had a noticeable effect on the spectra of the synthesized products. The products obtained at 5h, 7h, 90°C, 120°C, and 150°C did not contain the vibration band at 1224 cm^{-1}. This indicates the lack of crystallization to form ZSM-5 crystals (Jiang et al., 2014). Furthermore, the absence of the vibration band at 546 cm^{-1} for the following products (5h, 7h, 90°C, 120°C, and 150°C) further confirms the incomplete crystalline structure, and their respective diffraction patterns support this.

Ali et al. (2017) reported that absorption bands at 1220 and 1090 cm^{-1} signify the formation of ZSM-5 crystals and the presence of 3D pores. Furthermore, the internal symmetric stretching (780 cm^{-1}) and TO bending (465 cm^{-1}) absorption bands reveal the formation of Si–O and Al–O tetrahedra during hydrothermal heating. Comparatively, the double five-ring absorption bands were obtained at 546 cm^{-1} by Wang et al. (2007), 542 cm^{-1} by Luo et al. (2017), and 547 cm^{-1} by Mohiuddin et al. (2016). This

exposes the three-dimensional nature of the pore channels found in the aluminosilicate framework. Alternatively, the molecular structure of ZSM-5 can be identified and verified using the infrared (IR) optical density ratio. This is done by computing the area ratio of the vibrational bands at 426 and 546 cm^{-1}. An ideally synthesized ZSM-5 zeolite has an IR optical density of approximately 0.72 (Kim & Chung, 2003). In the current study, the reference ZSM-5 has an optical density of 0.67, whereas the values of the synthesized products could not be determined due to the incomplete crystalline structures.

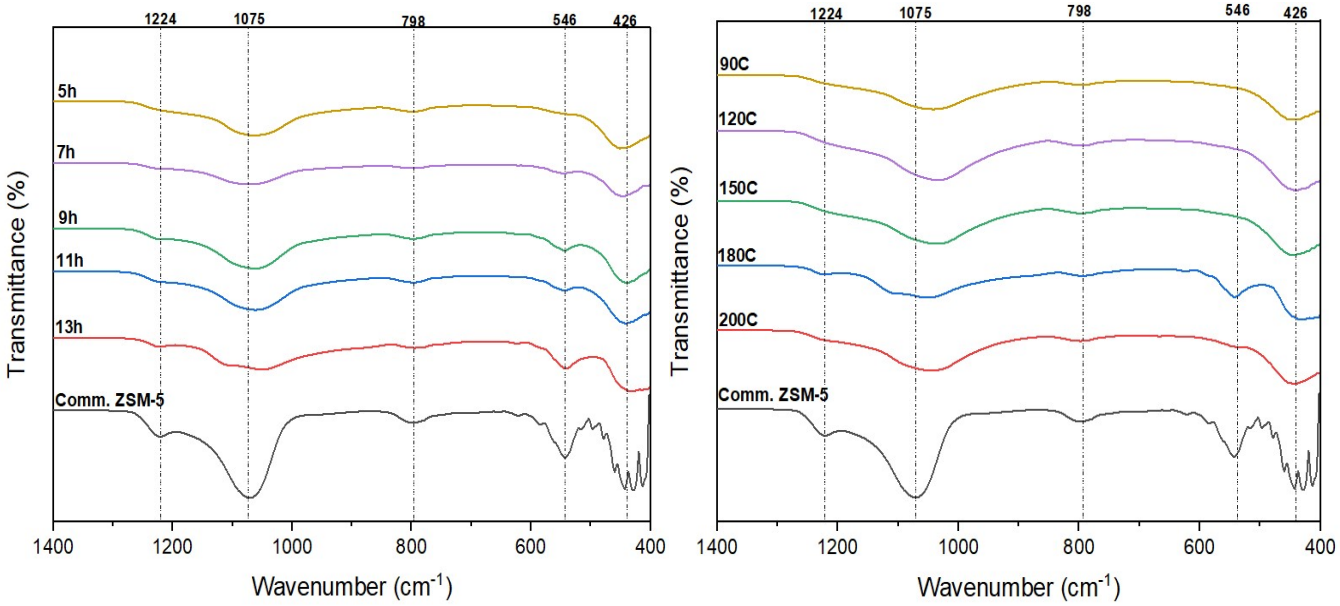

Figure 4.4. FT-IT spectra of powdered samples: a) Effect of synthesis time at 180°C and b) Effect of synthesis temperature at 13h.

4.3.5. Texture Properties of the Synthesized Properties

Table 4.2 presents the specific surface area and porosity characteristics of the synthesized ZSM-5 samples. It is crucial to note that only those products that displayed the distinctive diffraction profiles (***Figure 4.2***) of the unique ZSM-5 were considered. The reference sample contained an average pore size and specific surface area of 2.62 nm and 436.4 m^2/g, respectively. This shows a micro- and mesopore structure, as noted by the micropore volume (0.105 cm^3/g), further confirmed by the sorption isotherm in ***Figure 4.5***. An increase in synthesis time (from 9 to 13h) decreased pore size from 70.6 to 14.8 nm. However, the pore sizes of the synthesized ZSM-5 products were greater than those of the reference sample, whereas the specific surface areas were significantly less. The synthesized ZSM-5 products comprised mesopores, whereas those obtained at 9h comprised macropores (70.6 nm). The specific surface area and crystallinity of the synthesized ZSM-5 products were relatively low due to the trace metals deposited onto the mesopores. This was supported by the FT-IR spectra (***Figure 4.4***), which showed indistinct infrared optical density and weak vibrational intensities. Overall, the low crystallinity achieved by the synthesized ZSM-5 products displayed incomplete crystallization (Popova et al., 2021); however, the highest relative crystallinity was 52.4% (13h). The Si/Al molar ratio was constant for all synthesized ZSM-5 products, indicating that the variations in the synthesis time and temperature do not affect the chemical composition of the products (***Table 4.2***). Jiang et al. (2014) reported that the increased

synthesis time (6 to 120h) increased the specific surface area from 50 to 271 m^2/g. The pore diameter results are not reported. The specific surface area of ZSM-5 synthesized at 180°C and 13h in the current study was 108.4 m^2/g, which is less than that of ZSM-5 synthesized by Wu et al. (2020) from palygorskite (263 m^2/g, 48h), Zhou et al. (2013) from attapulgite (339 m^2/g, 12h) and Krisnandi et al. (2017) from rice husk ash (294.75 m^2/g, 144h).

Table 4.2. Textural and structural properties of the powdered samples.

Sample	S_{BET} (m^2/g)	V_{tot} (cm^3/g)	V_{micro} (cm^3/g)	Pore diameter (nm)	Crystallinity (%)	Si/Al molar ratio
Comm. ZSM-5	436.4	0.286	0.105	2.62	100	25
13h	108.4	0.394	n.d.	14.8	52.4	11.9
11h	106.6	0.448	n.d.	16.5	16.9	11.9
9h	95.7	0.169	n.d.	70.6	12.7	11.9
200°C	104.6	0.403	n.d.	24.9	51.2	11.9

n.d. = not detected.

Figure 4.5 shows the nitrogen physisorption isotherms and hysteresis curves of the synthesized ZSM-5 products. It can be observed that none of the products exhibited a sharp increase in adsorption at a relative pressure of $10^{-6} < p/p_0 < 0.01$. This is due to the lack of a microporous structure in all the products (Liu et al., 2019). Furthermore, all the samples displayed a type-IV adsorption isotherm with distinct hysteresis loops characteristic of capillary condensation occurring at high relative pressure, indicating the presence of mesopore structures (Liu et al., 2014a). The type-IV adsorption isotherm is typically obtained when synthesizing hierarchical ZSM-5 zeolite. Wu et al. (2020) obtained it using fibrous clay to synthesize large mesoporous intracrystals, Nandiwale et al. (2015) obtained it using a mesopore structure directing agent, and Popova et al. (2021) converted a microporous ZSM-5 to hierarchical ZSM-5 using a mixture of ammonium fluoride and hydrofluoric acid. In the high relative pressure ($p/p_0 > 0.6$) region, the synthesized ZSM-5 products depicted steep hysteresis loops that differed from the reference sample, suggesting varying mesoporous and macroporous structures. In other words, the products obtained at 13, 11, and 9h consisted of the type-H1 hysteresis loop, indicative of uniform mesopores with an open geometry in a narrow range (Liu et al., 2014a). A type-H4 hysteresis loop was observed in the reference sample, which indicates a mesoporous structure with narrow slit-like pores. Lastly, the product obtained at 9h comprised a type-H2 hysteresis loop, which describes a mesoporous and macroporous distribution of pore sizes and shapes that are not well-defined (Sing et al., 1985).

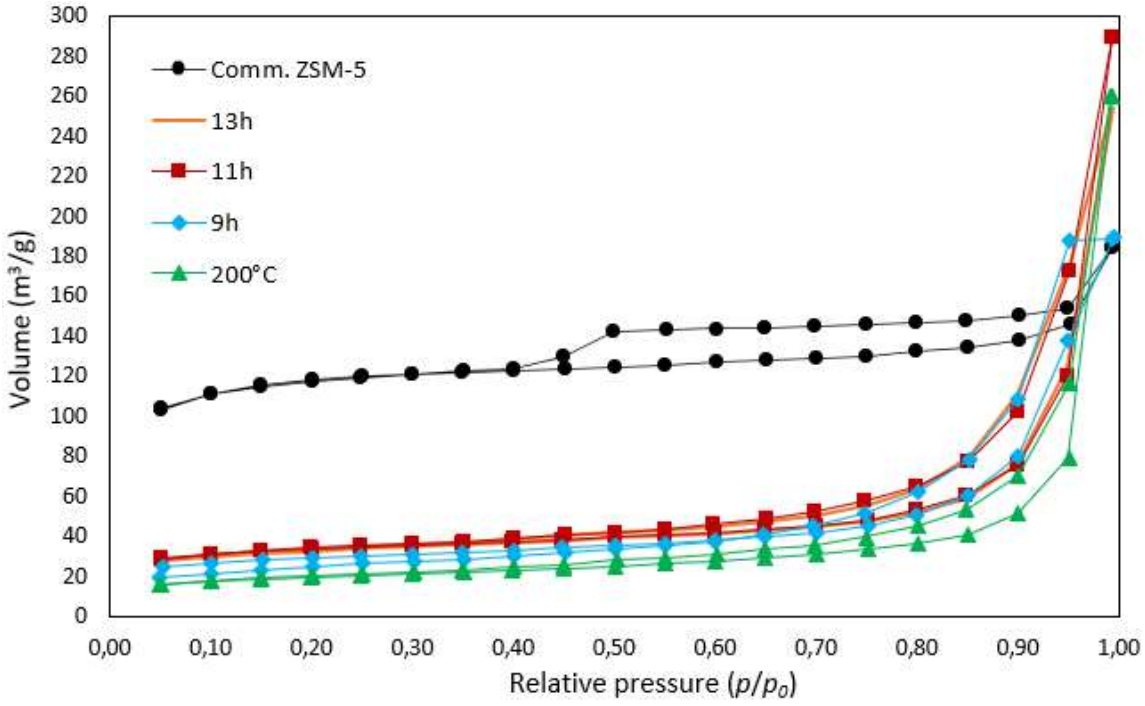

Figure 4.5. Nitrogen sorption isotherms of powdered samples.

4.3.6. Chemical Composition of ZSM-5

Table 4.3 compares the chemical composition of the synthesized ZSM-5 to the reference sample. The synthesized ZSM-5 was selected based on the maximum synthesis conditions, which were 13h and 180°C. Both porous materials consisted mainly of SiO_2 and less Al_2O_3. The chemical composition of the synthesized ZSM-5 was found to be unaffected by the synthesis temperature and time (**Table 4.*2***). Consequently, the characterization results were omitted. However, the synthesized ZSM-5 contained foreign compounds such as CaO (5.34 wt.%), MgO (2.36 wt.%), and trace metals (11.6 wt.%). This was due to the starting material used (blast furnace slag) during synthesis. Studies have shown that the incorporation of Ca and Mg into ZSM-5 leads to increased formation of olefins. That is, Yarulina et al. (2016) adjusted the distribution of acidic sites of ZSM-5 by impregnating it with Ca. It was found that the presence of Ca leads to increased selectivity for propylene and other light olefins while suppressing the formation of paraffins, thus enhancing catalyst lifetime. Magnesium, on the other hand, decreased the Brønsted acid sites with an increase in the Lewis acidity, as detailed by Yuan et al. (2019). Furthermore, the Mg-modified ZSM-5 showed higher selectivity towards propene with a shorter catalytic lifespan. Therefore, the incorporation of Ca and Mg into the ZSM-5 framework moderates its acidity, improves selectivity towards desired products, and advances catalyst stability.

Since ZSM-5 is mainly used to catalyze reactions found in the petrochemical industry, the presence of trace metals could improve the catalytic reactivity of the material. Researchers have shown that doping transitional metals into the porous structure of ZSM-5 has the benefits of ion exchange and catalytic reactivity. For instance, Wang et al. (2018) impregnated ZSM-5 with copper and manganese to improve its adsorptive properties and reduce the oxides of nitrogen from the atmosphere. In another study, Chiosso et al. (2023) dopped Zn, Cr, and Fe to modify the properties of hierarchal ZSM-5 for the catalytic cracking of bio-oil. The Si/Al ratio of commercial ZSM-5 was observed to be twice that

of synthesized ZSM-5, with both falling under the category of high-silica zeolites (Si/Al > 5). The transition in Si/Al ratio from the pretreated slag (8.0; ***Table 4.1***) to the synthesized ZSM-5 (11.9; ***Table 4.3***) suggests that the synthesis process favored the incorporation of more silicon relative to aluminum. The process of ZSM-5 synthesis consists of various stages, including the dissolution of Si and Al components, generation of reactive species, formation of ZSM-5 building blocks, and eventual crystal growth (Liu et al., 2014b). It is within these stages that factors such as preferential silicon integration, aluminum dissolution, or the emergence of secondary phases may impact the Si/Al ratio of ZSM-5.

Table 4.3. Chemical composition of ZSM-5.

Compound	SiO_2	Al_2O_3	CaO	MgO	Traces	Si/Al ratio
Synthesized ZSM-5 (wt.%)	75.29	5.38	5.34	2.36	11.6	**11.9**
Commercial ZSM-5 (wt.%)	96.67	3.28	0	0	0.05	**25.0**

Traces: Fe_2O_3, MnO, Na_2O, K_2O, TiO_2, P_2O_5, Cr_2O_3 and NiO

4.4. Conclusion

The current study demonstrated the coupling of green chemistry with the hydrothermal synthesis method to enhance the production of a novel ZSM-5 zeolite. This was accomplished using blast furnace slag (industrial waste) as a silica and alumina source and microwave irradiation as a heat source. The industrial waste slag was successfully beneficiated through acid leaching to reduce impurities (CaO and MgO) to 3.48 and 1.54 wt.%, respectively. The pretreated slag mainly comprised SiO_2 (55.23 wt.%), less Al_2O_3 (5.85 wt.%), and trace metals. Microwave irradiation drastically decreased the synthesis time to 13h, producing a moderately crystalline (52.4%) phase of ZSM-5 consisting of well-defined cubic prism shapes with microsized intergrown rectangular crystals. It was observed that the morphology of the synthesized ZSM-5 depends on the starting material, that is, the type of industrial waste used. Furthermore, the synthesis time affects the morphology of the crystals, whereas the synthesis temperature affects the crystal size. Conclusively, the maximum synthesis conditions were 13h and 180°C.

The synthesized ZSM-5 products exhibited mesoporous (13h, 11h, and 200°C) and macroporous structures with relatively low specific surface areas compared with the reference sample. The low specific surface areas were attributed to the presence of trace metal alloys deposited onto the mesoporous pores. The Si/Al molar ratio of the synthesized ZSM-5 products was constant (11.9) and was not affected by changes in the synthesis temperature or time. Therefore, the products were ranked as high-silica zeolites. Absorption bands that represent the structure of ZSM-5 appeared at 1224, 1075, 798, 546, and 426 cm^{-1}. This study demonstrated the successful coupling of green chemistry with hydrothermal synthesis to produce ZSM-5 zeolite with suitable physicochemical, textural, and structural properties. The novel ZSM-5 zeolite was successfully synthesized, consisting of metal alloys such as Fe_2O_3, MnO, TiO_2, Cr_2O_3, and NiO.

References

Ahedi, R. K., Kotasthane, A. N., Rao, B. S., Manna, A., & Kulkarni, B. D. (2001). Synthesis of ferrierite-type zeolite in the presence of a catalytic amount of pyrrolidine and sodium bis(2-ethyhlhexyl) sulfosuccinate. *Journal of Colloid and Interface Science*, *236*(1), 47–51. https://doi.org/10.1006/jcis.2000.7390

Ali, I., Hassan, A., Shabaan, S., & El-Nasser, K. (2017). Synthesis and characterization of composite catalysts Cr/ZSM-5 and their effects toward photocatalytic degradation of p-nitrophenol. *Arabian Journal of Chemistry*, *10*, S2106–S2114. https://doi.org/10.1016/j.arabjc.2013.07.042

Anuwattana, R., Balkus, K. J., Asavapisit, S., & Khummongkol, P. (2008). Conventional and microwave hydrothermal synthesis of zeolite ZSM-5 from the cupola slag. *Microporous and Mesoporous Materials*, *111*(1–3), 260–266. https://doi.org/10.1016/j.micromeso.2007.07.039

Chiosso, M. E., Crespo, I., Merlo, A. B., & Valle, B. (2023). Metal-Doped HZSM-5 Zeolite Catalysts for Catalytic Cracking of Raw Bio-Oil: Exploring Activity toward Value-Added Products. *Catalysts, Vol. 13, Page 1198*, *13*(8), 1198. https://doi.org/10.3390/CATAL13081198

Deng, L., Yun, F., Jia, R., Li, H., Jia, X., Shi, Y., & Zhang, X. (2020). Effect of SiO2/MgO ratio on the crystallization behavior, structure, and properties of wollastonite-augite glass-ceramics derived from stainless steel slag. *Materials Chemistry and Physics*, *239*, 122039. https://doi.org/10.1016/J.MATCHEMPHYS.2019.122039

Derbe, T., Temesgen, S., & Bitew, M. (2021). A Short Review on Synthesis, Characterization, and Applications of Zeolites. *Advances in Materials Science and Engineering*, *2021*, 0–17. https://doi.org/10.1155/2021/6637898

Duan, W., Wang, D., Wang, Z., & Yu, Q. (2022). Hydrometallurgical Leaching Behavior and Kinetic Modeling of Blast Furnace Slag in Hydrochloric Acid. *Journal of Sustainable Metallurgy*, *8*(1), 170–185. https://doi.org/10.1007/s40831-021-00473-w

Eren, S., Türk, F. N., & Arslanoğlu, H. (2024). Synthesis of zeolite from industrial wastes: a review on characterization and heavy metal and dye removal. *Environmental Science and Pollution Research*, *31*(29), 41791–41823. https://doi.org/10.1007/s11356-024-33863-0

Han, S., Liu, Y., Yin, C., & Jiang, N. (2019). Fast synthesis of submicron ZSM-5 zeolite from leached illite clay using a seed-assisted method. *Microporous and Mesoporous Materials*, *275*, 223–228. https://doi.org/10.1016/j.micromeso.2018.08.028

Jha, B., & Singh, D. N. (2011). A review on synthesis, characterization and industrial applications of Flyash zeolites. *Journal of Materials Education*, *33*(1–2), 65–132.

Jiang, J., Duanmu, C., Yang, Y., Gu, X., & Chen, J. (2014). Synthesis and characterization of high siliceous ZSM-5 zeolite from acid-treated palygorskite. *Powder Technology*, *251*, 9–14. https://doi.org/10.1016/j.powtec.2013.10.020

Kim, D. J., & Chung, H. S. (2003). Synthesis and characterization of ZSM-5 zeolite from serpentine. *Applied Clay Science*, *24*(1–2), 69–77. https://doi.org/10.1016/S0169-1317(03)00149-2

Krisnandi, Y. K., Yanti, F. M., & Murti, S. D. S. (2017). Synthesis of ZSM-5 zeolite from coal fly ash and rice husk: characterization and application for partial oxidation of methane to

methanol. In *IOP Conference Series: Materials Science and Engineering*, *188*, 012031. https://doi.org/10.1088/1742-6596/755/1/011001

Kumar, A., Kuang, Y., Liang, Z., & Sun, X. (2020). Microwave chemistry, recent advancements, and eco-friendly microwave-assisted synthesis of nanoarchitectures and their applications: a review. *Materials Today Nano*, *11*, 100076. https://doi.org/10.1016/J.MTNANO.2020.100076

Liu, B., Zheng, L., Zhu, Z., Zhang, K., Xi, H., & Qian, Y. (2014a). Effect of synthesis conditions on the structural and catalytic properties of hierarchically structured ZSM-5 zeolites. *RSC Advances*, *4*(27), 13831–13838. https://doi.org/10.1039/C4RA00124A

Liu, C., Kong, D., & Guo, H. (2014b). The morphology control of zeolite ZSM-5 by regulating the polymerization degree of silicon and aluminum sources. *Microporous and Mesoporous Materials*, *193*, 61–68. https://doi.org/10.1016/j.micromeso.2014.03.015

Liu, Y., Han, S., Guan, D., Chen, S., Wu, Y., Yang, Y., & Jiang, N. (2019). Rapid green synthesis of ZSM-5 zeolite from leached illite clay. *Microporous and Mesoporous Materials*, *280*, 324–330. https://doi.org/10.1016/j.micromeso.2019.02.027

Luo, W., Yang, X., Wang, Z., Huang, W., Chen, J., Jiang, W., Wang, L., Cheng, X., Deng, Y., & Zhao, D. (2017). Synthesis of ZSM-5 aggregates made of zeolite nanocrystals through a simple solvent-free method. *Microporous and Mesoporous Materials*, *243*, 112–118. https://doi.org/10.1016/j.micromeso.2017.01.040

Meng, X., & Xiao, F. S. (2014). Green routes for synthesis of zeolites. In *Chemical Reviews*, *114*(2), 1521–1543. https://doi.org/10.1021/cr4001513

Mohiuddin, E., Isa, Y. M., Mdleleni, M. M., Sincadu, N., Key, D., & Tshabalala, T. (2016). Synthesis of ZSM-5 from impure and beneficiated Grahamstown kaolin: Effect of kaolinite content, crystallisation temperatures and time. *Applied Clay Science*, *119*, 213–221. https://doi.org/10.1016/j.clay.2015.10.008

Morgan, H. M., Bu, Q., Liang, J., Liu, Y., Mao, H., Shi, A., Lei, H., & Ruan, R. (2017). A review of catalytic microwave pyrolysis of lignocellulosic biomass for value-added fuel and chemicals. *Bioresource Technology*, *230*, 112–121. https://doi.org/10.1016/j.biortech.2017.01.059

Nandiwale, K. Y., Pande, A. M., & Bokade, V. V. (2015). One step synthesis of ethyl levulinate biofuel by ethanolysis of renewable furfuryl alcohol over hierarchical zeolite catalyst. *RSC Advances*, *5*(97), 79224–79231. https://doi.org/10.1039/c5ra13520f

Parnham, E. R., & Morris, R. E. (2006). The ionothermal synthesis of cobalt aluminophosphate zeolite frameworks. *Journal of the American Chemical Society*, *128*(7), 2204–2205. https://doi.org/10.1021/JA057933L/SUPPL_FILE/JA057933LSI20051122_094614.CIF

Popova, M., Szegedi, Á., Oykova, M., Lazarova, H., Koseva, N., Mihályi, M. R., & Shestakova, P. (2021). Selective production of phenol on bifunctional, hierarchical zsm-5 zeolites. *Molecules*, *26*(12). https://doi.org/10.3390/molecules26123576

Sing, K. S. W., Everett, D. H., Haul, R. A. W., Moscou, L., Pierotti, R. A., Rouquerol, J., & Siemieniewska, T. (1985). Reporting physisorption data for gas/solid systems-with special reference to the determination of surface area and porosity. *Pure & App. Chem.*, *57*(4), 603–619.

Tung, D., Phương, N. T., Tri, T. V., Xuan, D. T. T., & Thu, N. H. (2012). Effect of feedstock properties on the performance of ZSM-5 additive in catalytic cracking reaction. *Petrovietnam Journal*, *10*, 59–64.

Wajima, T., & Ikegami, Y. (2008). Zeolite synthesis from paper sludge ash via acid leaching. *Chemical Engineering Communications*, *195*(3), 305–315. https://doi.org/10.1080/00986440701555258

Wang, S., Jiang, X., Nie, G., Wang, Z., Yu, H., Liu, Y., Wu, Q., Yu, S., & Liu, S. (2023). Trash into treasure: Nano ZSM-5 catalyst for cracking waste cooking oil to bio-gasoline with enhanced selectivity. *Fuel Processing Technology*, *242*, 107666. https://doi.org/10.1016/j.fuproc.2023.107666

Wang, T., Zhang, X., Liu, J., Liu, H., Wang, Y., & Sun, B. (2018). Effects of temperature on NOx removal with Mn-Cu/ZSM5 catalysts assisted by plasma. *Applied Thermal Engineering*, *130*, 1224–1232. https://doi.org/10.1016/J.APPLTHERMALENG.2017.11.113

Wang, P., Shen, B., & Gao, J. (2007). Synthesis of ZSM-5 zeolite from expanded perlite and its catalytic performance in FCC gasoline aromatization. *Catalysis Today*, *125*(3–4), 155–162. https://doi.org/10.1016/j.cattod.2007.03.010

Wu, M., Jiang, W., Jiang, J., Zou, Y., Zhang, P., Mao, P., Xu, Y., & Shi, Y. (2020). Synthesis of ZSM-5 zeolites using palygorskite as raw material under solvent-free conditions. *Bulletin of Materials Science*, *43*, 289. https://doi.org/10.1007/s12034-020-02263-8S

Wu, Q., Wang, X., Qi, G., Guo, Q., Pan, S., Meng, X., Xu, J., Deng, F., Fan, F., Feng, Z., Li, C., Maurer, S., Müller, U., & Xiao, F. S. (2014). Sustainable synthesis of zeolites without addition of both organotemplates and solvents. *Journal of the American Chemical Society*, *136*(10), 4019–4025. https://doi.org/10.1021/ja500098j

Yarulina, I., Bailleul, S., Pustovarenko, A., Martinez, J. R., Wispelaere, K. De, Hajek, J., Weckhuysen, B. M., Houben, K., Baldus, M., Van Speybroeck, V., Kapteijn, F., & Gascon, J. (2016). Suppression of the Aromatic Cycle in Methanol-to-Olefins Reaction over ZSM-5 by Post-Synthetic Modification Using Calcium. *ChemCatChem*, *8*, 3057–3063. https://doi.org/10.1002/cctc.201600650

Yuan, D., Sang, Y., Xing, A., Wang, C., Miao, P., & Sun, Q. (2019). Tuning of Magnesium Distribution in ZSM-5 via Different Impregnation Methods and Its Effect on Methanol to Propene Reaction. *Industrial and Engineering Chemistry Research*, *58*, 5112–5120. https://doi.org/10.1021/acs.iecr.8b04434

Zhang, Q., Gao, S., & Yu, J. (2023). Metal Sites in Zeolites: Synthesis, Characterization, and Catalysis. *Chemical Reviews*, *123*, 6039–6106. https://doi.org/10.1021/acs.chemrev.2c00315

Zhang, H., Samsudin, I. bin, Jaenicke, S., & Chuah, G. K. (2022). Zeolites in catalysis: sustainable synthesis and its impact on properties and applications. *Catalysis Science & Technology*, *12*(19), 6024–6039. https://doi.org/10.1039/D2CY01325H

Zhou, X., Liu, Y., Meng, X., Shen, B., & Xiao, F. (2013). Synthesis and catalytic cracking performance of Fe/Ti-ZSM-5 zeolite from attapulgite mineral. *Cuihua Xuebao/Chinese Journal of Catalysis*, *34*(8), 1504–1512. https://doi.org/10.1016/S1872-2067(12)60638-X

CHAPTER 5

5. CATALYTIC PERFORMANCE AND SELECTIVITY OF SYNTHESIZED ZSM-5 CATALYST IN BIOMASS PYROLYSIS

Conference paper under review.

Abstract

Microwave-irradiated pyrolysis has emerged as a highly efficient technique for processing lignocellulosic biomass feedstocks. This fast pyrolysis method is gaining widespread recognition due to its precise temperature control, high heating efficiency, rapid and volumetric heating efficiency, and processing of large-sized particles. The current study demonstrated the use of a FlexiWave microwave synthesis lab station (power output of 950 W) for the pyrolysis of corn cob in the presence of a ZSM-5 zeolite catalyst. The catalyst was synthesized from slag waste and featured a three-dimensional mesoporous crystalline structure inhabited by trace metal elements (Fe, Mn, Ti, Cr, and Ni). The synthesized catalyst consisted of a large pore size (15.6 nm) coupled with a relatively low specific surface area (107.5 m^2/g) and a high SiO_2/Al_2O_3 ratio (24.8). The catalyst was evaluated by varying the catalyst-to-biomass ratio (1:9–1:2), pyrolysis time (3–7 min), and pyrolysis temperature (150–350°C). The synthesized ZSM-5 catalyst exhibited a comparable bio-oil conversion rate (43.6 wt.%) to commercial ZSM-5 (41.9 wt.%), suggesting similar catalytic activity under the tested conditions. The synthesized catalyst exhibited a significant selectivity for phenols (23.2%) and ketones (36.9%). The identified ketones were ethenone and cyclohexanone, while the phenolic compounds included catechol and cresol. Although the primary product targeted was bio-oil, the gas yield exceeded that of the bio-oil. The ketonic- and phenolic-rich bio-oil obtained in this research can be improved and utilized as raw material for producing bio-based products for the chemical industry.

5.1. Introduction

There are numerous ways to generate energy from lignocellulosic biomass residues using different techniques such as biological, thermochemical, and mechanical processing. Most of these processes are comparatively selective, resulting in the production of a limited variety of products. Pyrolysis, a thermochemical conversion process, is known for its non-selective nature. This process can produce various products, such as bio-oil, biochar, and non-condensable gases, in a short reaction time (Yildiz et al., 2016). During the high-temperature conversion of lignocellulosic biomass, primary intermediates are formed, which undergo subsequent reactions such as decarboxylation, dehydration, reforming, decarbonylation, and oligomerization, to yield various products where bio-oil is the primary one. The liquid product forms a crude bio-oil comprising a wide range of oxygenated hydrocarbon derivates such as alcohols, ketones, phenols, ethers, carboxylic acids, esters, and aldehydes (Grams & Ruppert, 2021). Bio-oil, characterized by its dark-brown and free-flowing consistency, faces technical limitations regarding commercialization. Bio-oil cannot be directly used as a fuel for transportation due to its poor chemical stability, high oxygen and moisture content, low storage time, low caloric value (16.79 – 19 MJ/kg), acidity (pH 2 – 3), and a high polarity which causes it to be immiscible with conventional fuels (Rahman et al., 2018). In contrast, biochar is also a product of the pyrolytic conversion of lignocellulosic biomass. The physicochemical properties of biochar make it unsuitable for secondary use. Hence, biochar needs to be treated to remove impurities and improve its specific surface area (Mohamed et al., 2016). In addition, the gaseous stream typically consists of syngas (CO and H_2) amongst other compounds (CO_2, CH_4, and light hydrocarbons). However, the quality of the gas stream might be compromised by impurities such as heavy metals (present in the biomass), nitrogen oxides, and sulfur compounds (Kosanić et al., 2014). The gas stream composition depends on the type of feedstock used. Therefore, there is a need to incorporate a catalyst during the pyrolysis of lignocellulosic biomass to catalytically upgrade the physicochemical properties of the products (bio-oil, biochar, and non-condensable gases). Catalysts used in converting lignocellulosic biomass are assembled from various materials, among which zeolite-based catalysts play a crucial role in boosting catalytic activity and selectivity.

Among the multifarious zeolites, Zeolite Socony Mobil-5 (ZSM-5) shows an impressive capability as an industrial catalyst to catalyze reactions found in the petrochemical refinery industry (Bai et al., 2019). ZSM-5 is a microporous material that consists of an aluminosilicate crystalline framework. The silica (SiO_2) and alumina (Al_2O_3) are tetrahedrally bonded to form layers of membered rings, which create micropores and channels inside the framework (Zhou et al., 2013). The pores and channels permit various-sized and -shaped organic molecules to diffuse through and react with the acidic sites to form complex hydrocarbon compounds (aromatics, aliphatics, and their derivates). Thus, their shape-selective nature permits the control of product distribution and increases the yield of aromatics that are in high demand. Several studies have reported that pore structure, composition (SiO_2/Al_2O_3 ratio), and stability significantly influence the catalyst's activity and selectivity. Various methods have been practiced to synthesize ZSM-5 with specific textural properties (acidity, pore size, and shape) to achieve selectivity and activity toward aromatic compounds. Moreover, the incorporation of transitional metals (Fe, Co, Pb, Zn, Ni, Ga, and Mo) into the ZSM-5 framework improves bio-oil production, limits water formation, supports reforming reactions, and promotes hydrogen transfer (Grams & Ruppert, 2021). However, the increased activity still favors the formation of gases instead of the liquid fraction. Li et al. (2014) investigated the catalytic fast pyrolysis of lignocellulosic biomass

in the presence of a desilicated ZSM-5 zeolite. The desilication process was used to modify the pore structure of the catalyst. It was reported that the mesoporous structure improved the diffusion of bulky organic molecules, resulting in an increased yield of aromatic hydrocarbons (26.2 to 30.2%). Similarly, Zhang et al. (2013) pyrolyzed straw biomass in the presence of a ZSM-5 catalyst, resulting in an increase in the yield of aromatics (12.8%) and C2-C4 olefins (10.5%). Liang et al. (2017) doped ZSM-5 with various transition metals (Co, Zn, and Ni) to improve bio-oil composition. The study pyrolyzed rice straw via microwave-assisted pyrolysis to increase the composition of bio-oil to above 50% on average. The current study used green chemistry and hydrothermal synthesis techniques to synthesize a mesoporous ZSM-5 catalyst from blast furnace slag. Blast furnace slag (BFS) is an industrial waste generated by the iron- and steelmaking industry. It primarily consists of Al_2O_3, SiO_2, MgO, and CaO, amongst other trace metals (Mn, Ti, Fe, Cr, Ni, and Na).

Microwave-assisted pyrolysis, a fast pyrolysis method, has rapidly gained prominence as a preferred technique for processing lignocellulosic biomass feedstocks. These feedstocks encompass various residues generated by the forestry (pine, douglas fir, wood pellets) and agricultural (wheat straw, corn residues, bagasse) industries (Suriapparao et al., 2015). This technique has several advantages compared to the conventional pyrolysis technique. It offers the ability to process large-sized particles, minimal pre-treatment requirement of raw materials, high heating efficiency, immediate and homogeneous heating of raw materials, shorter residence time requirement, and the possibility to use different feedstocks (Ravikumar et al., 2017). As such, size control of biomass particles and rapid agitation are unnecessary, unlike pyrolysis using fluidized bed reactors. The rapid heating of lignocellulosic biomass feedstocks using microwaves is attributed to polar molecules within the materials. When exposed to microwave electromagnetic radiation, these polar molecules experience continuous rotation, known as dipole rotation. As these molecules rotate, they collide with surrounding molecules and transfer their energy in the form of heat, resulting in the rapid heating of the material (Wu et al., 2014). The influence of microwaves increases with higher induced polarity, making microwave heating advantageous due to its volumetric and selective heating capabilities.

Materials can be classified into three categories: absorbers such as water and activated carbon that can absorb microwaves, conductors that reflect microwaves (lignocellulosic biomass), and insulators or microwave-transparent materials (ceramics). Due to their poor ability to absorb microwave energy, microwave absorbers are commonly added to lignocellulosic biomass to increase absorption. This results in faster heating rates and lower microwave power requirements for achieving pyrolysis temperatures (Shang et al., 2015). Microwave absorbing materials, often referred to as susceptors, are pivotal in transforming the incoming microwave energy into thermal energy, primarily due to the diminished dielectric loss factor inherent in biomasses. Notable among such materials are carbonaceous compounds, including but not limited to biochar, activated carbon, and graphite. Certain ceramics, such as metal hydroxides, metals, silicon carbide, and metal oxides, have been documented as efficient susceptors. These materials are mixed with biomass to induce pyrolysis (Suriapparao et al., 2015). Shang et al. (2015) investigated the effect of microwave absorbers (coke, AC, SiC, NaOH, and K_2CO_3) on the microwave-assisted pyrolysis of lignocellulosic biomass. It was reported that (1) the significant difference between the densities of silicon carbide and biomass creates non-uniform mixing, which results in low liquid and gas yields, (2) Sodium hydrate and potassium carbonate achieved high absorption of microwaves and primarily produced gases, and (3) coke and activated carbon (AC) had different effects on pyrolysis, that is, AC produced the highest liquid fraction but

both favored gas production. Overall, microwave absorbers influenced the properties and yield of the final products.

Several studies have demonstrated the effective conversion of waste blast furnace slag into zeolite ZSM-5, with detailed analyses of the physicochemical properties of the resulting material. However, limited studies evaluate the catalytic activity of a catalyst derived from slag waste. The present study sought to address this gap by assessing the ability of a mesoporous catalyst (ZSM-5) synthesized from slag waste to catalyze the conversion of lignocellulosic biomass via microwave-assisted pyrolysis. Corn cob residue was selected as a suitable model for lignocellulosic biomass, given that maize is the largest food crop grown in South Africa, with the Free State province being the foremost producer. An annual yield of approximately 10 million metric tons leads to considerable amounts of corn cob residues, which harm the environment (Ala-Kokko et al., 2021). The catalytic pyrolysis of corn cob residue provides multiple benefits, including the transformation of industrial waste into valuable energy products, the utilization of waste materials, the advancement of sustainable agriculture, the diversification of energy sources, and the reduction of dependency on fossil fuels.

5.2. Materials and Methods

5.2.1. Chemicals and Materials

Raw corn samples (2.0 kg) were collected from a local maize plantation in Vereeniging, South Africa. The corn was oven-dried at 120°C for 24 h to remove excess moisture. The corn kernels were manually removed, resulting in corn cob (CC) residues of 6 and 20 cm in average diameter and length, respectively. The CC underwent additional processing through crushing, milling, and sieving to obtain the desired size range of 2 – 1.2 mm. The powdered CC samples were used as biomass feedstock. Granular activated carbon (GAC 830 PLUS) was used as a high-purity microwave absorber. Raw blast furnace slag (BFS) was collected from the iron and steelmaking industry. The BFS was prepared through crushing and milling and used as feed for ZSM-5 synthesis. Commercial ZSM-5 zeolite (Si/Al ratio = 25 and particle diameter = 2 – 5 µm) was used as a reference catalyst. The materials and chemicals used were analytical grades obtained from local suppliers in South Africa. Air Liquide supplied pure nitrogen gas (99.99%).

5.2.2. ZSM-5 Synthesis Method

ZSM-5 was synthesized using the hydrothermal synthesis method. It involved preparing two solutions containing precise amounts of tetrapropylammonium bromide (TPABr), deionized water (solution A), and NaOH, BFS, and deionized water (mixture B). The solutions were then carefully combined to form a gel mixture and transferred to a hydrothermal reactor. The gel mixture underwent hydrothermal treatment at a high temperature and pressure, producing ZSM-5 crystals. For a comprehensive understanding of the synthesis method, refer to ***section 4.2.3***. The resulting solids were calcined at 550°C for 5 h to remove the structure-directing agent (TPABr) and produce Na-ZSM-5 zeolite. Na-ZSM-5 was suspended in 1.5M NH_4Cl solution (10 mL/g of ZSM-5) under the following conditions: 2 h, 110°C, and reflux. This was done to substitute Na^+ ions with NH_4^+ ions. The mixture was subsequently filtered, washed, and oven-dried overnight. The acidic H^+ form of ZSM-5 was obtained via calcination at 550°C for 5 h.

5.2.3. Microwave-assisted Pyrolysis Experiments

During the pyrolysis experiments, batch mixtures containing activated carbon (20 g), varying amounts of biomass (CC), and catalyst (ZSM-5) were prepared, blended, and loaded into the round bottom flask. The catalyst-to-biomass ratio was varied at 1:9, 1:5, 1:4, 1:3, and 1:2. Activated carbon (AC) was used as a microwave absorbent due to its excellent absorption properties for microwaves. This resulted in a significantly enhanced heating rate. The rapid microwave-assisted pyrolysis experiments were conducted as outlined in ***Figure 5.1***. Nitrogen gas was used as a carrier gas for each experimental run. Before each run, nitrogen was purged through the system at a flow rate of 0.8 L/min for 15 min to ensure an inert environment. The pyrolysis temperature (150, 200, 250, 300, and 350°C) and time (3, 4, 5, 6, and 7 min) were varied at a fixed microwave power output of 950 W and frequency of 2.45 GHz. The power setting was maintained at a consistent heating rate of 150°C/min. An advanced infrared temperature sensor was used to measure the temperature inside the FlexiWave microwave synthesis lab station manufactured by Milestone S.r.l company (Bergamo, Italy). The desired reaction temperatures were controlled and maintained by a continuous power PID controller operated by the microwave lab station at a minimum power rating (0 – 100 W). During pyrolysis, the volatile matter produced was purged out of the system using nitrogen as a sweep gas with a flow rate of 0.8 L/min. The temperature inside the reaction vessel was monitored using an infrared temperature sensor. The heavier volatiles underwent condensation, resulting in bio-oil formation, while the lighter volatiles were collected as syngas for analysis. Char was collected as residue at the bottom of the round bottom flask.

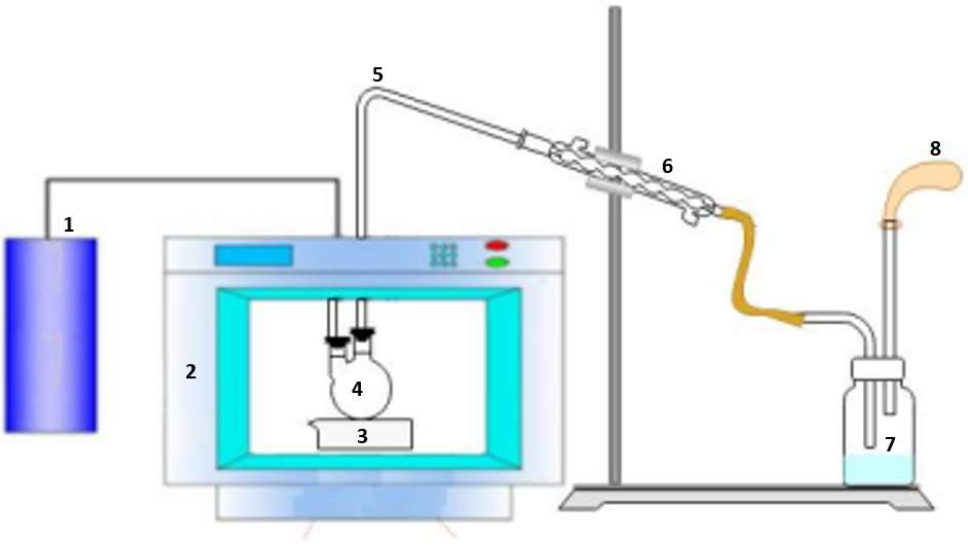

Figure 5.1. Microwave-assisted pyrolysis setup: 1) nitrogen gas tank, 2) microwave lab station, 3) weflon base plate, 4) round-bottomed flask, 5) glass connecting tube, 6) Allihn condenser, 7) bio-oil collection vessel, and 8) gas collection bag.

Each fraction of the solid and liquid pyrolysis products was weighed to determine the collected masses. The yield (Y) of the liquid and solid products were calculated from Equations 5.1 and 5.2, respectively. At the same time, the gas yield was determined by difference (Eq. 5.3).

$$Y_{bio-o} = \left(\frac{M_{bio-oil}}{M_0}\right) \times 100. \quad (5.1)$$

$$Y_{biochar} = \left(\frac{M_{biochar}}{M_0}\right) \times 100\% \quad (5.2)$$

$$Y_{gas} = 100\% - [Y_{char} + Y_{bio-oil}] \quad (5.3)$$

$$Con_{bio-o} = \left(\frac{M_{bio-o}}{M_0 \times X_{vol}}\right) \times 100\% \quad (5.4)$$

where M_0 is the initial mass of corn cob (g), $M_{biochar}$ is the mass of biochar (g), M_{bio-o} is the mass of bio-oil (g), $Con_{bio-oil}$ is the conversion rate of bio-oil (%), and X_{vol} is the mass fraction of volatile matter in the corn cob.

5.2.4. Biomass and Catalyst Characterization

The proximate analysis involved determining the fixed carbon (FC), volatile matter (VM), moisture content (MC), and ash content of the samples. The ASTM D5142 method was employed to analyze the corn cob samples. This analysis used a Thermogravimetric Analyzer (TGA; SDT-600, Advanced laboratory solutions). A SUPERCAL 2 modular calorimeter system was used to determine the calorific value of corn cob. This was done by pelletizing 10 mg of sample into a sample holder (crucible) and placing the steel capsule into the bomb calorimeter. The analysis was conducted in accordance with the ASTM D5865-13 standard. A Bruker D2 Phaser powder X-ray analyzer equipped with CuK_α radiation tubes ($\lambda = 1.5418$ Å) was used to perform x-ray diffraction (XRD) measurements of the powdered samples. The data was recorded at a continuous scanning range of 5 – 90°/2θ and a counting time of 0.2 s per step. The postprocessing of the data was done using the DIFFRAC.EVA software. The analysis of nitrogen sorption-desorption isotherms at –196°C was used to calculate the textural properties (pore size, pore volume, and specific surface area) of the catalysts using a Quantachrome Autosorb iQ3 instrument (Anton Paar, USA). Degassing of the powdered samples was done under vacuum at 300°C for 3 hours. The total amount of gas absorbed at a relative pressure (p/p_0) of 0.98 was used to calculate the total pore volume (V_{tot}). The micropore volume (V_{micro}) was calculated using the *t*-plot method applied to the fraction of the isotherm at $p/p_0 < 0.01$. An X-ray fluorescence (XRF) spectrometer (Panalytical brand, model Axios) was used to determine the chemical composition of the powdered samples. The X-ray spectrometer is fitted with an Rh tube and three detectors, and the loss of ignition (LOI) was determined at 1050°C for 1 hour. To ensure robust reproducibility of the data sets, characterization was conducted in triplicate, and a standard deviation of less than 5% was enforced using the STDEV function in Excel.

5.2.5. Pyrolysis Product Characterization

The product yield, both liquid and solid, was quantified based on the initial mass of biomass. Additionally, the gas yield was determined by the difference. The liquid product consisted of bio-crude oil collected after condensing the volatile products. A gas chromatography-mass spectrometer (GC-MS; GC-2010 Plus; MS QP2010 Ultra; Shimadzu) was used to detect the chemical compounds present in bio-oil. The GC was programmed to initially heat to 60°C for 2 min, then to 280°C at a rate of 20 °C/min. A sample size of 1 µL was injected, and the carrier gas (helium) flowed at 1.61 mL/min. The ion source temperature for the mass-selective detector was set to 200°C. The NIST Mass Spectral library was used to identify the detected compounds by comparing the spectral data. A gas

chromatograph (GC; 430-GC) manufactured by Bruker analytical solutions and equipped with a thermal conductivity detector was used to determine the chemical composition of gases. The equipment allows for accurate and precise identification of various components present in the gas samples.

The area percentages of the chromatograph peaks were used to estimate the relative content of each compound in the liquid and gaseous products. This was done using the following equation:

$$R_{content} = \frac{P_i}{P_{total}} \times 100\% \quad (5.5)$$

where P_{total} is the total peak area under a specific condition, and P_i is the peak area of a particular identified product. The selectivity (S) of the organic compounds in the bio-oil was also calculated as follows:

$$S_{compound} = \frac{R_i}{\sum(R_i)} \times 100\% \quad (5.6)$$

R_i is the compound's relative content, and $\Sigma(R_i)$ is the relative content of all the identified compounds.

5.3. Results and Discussion

5.3.1. Proximate Analysis of Corn Cob (CC)

Table 5.1 presents the proximate analysis of the corn cob conducted in this study, along with corresponding values obtained from relevant literature. The results were obtained from the thermogram plots shown in *7.2*. Appendix B (Microwave-assisted Pyrolysis Experiments). The volatile matter (75.98 wt.%), fixed carbon (16.55 wt.%), and ash content (3.01 wt.%) were consistent with the results reported in the literature. Meanwhile, the moisture content (4.46 wt.%) was comparably low. The corn cob's energy value (16.75 MJ/kg) was measured to determine its use as a solid fuel.

Table 5.1. Proximate analysis of corn cob.

Source	Properties				
	Moisture Content (wt.%)	**Volatile Matter (wt.%)**	**Fixed Carbon (wt.%)**	**Ash Content (wt.%)**	**Calorific value (MJ/kg)**
Corn cob	4.46 ± 0.38	75.98 ± 0.72	16.55 ± 0.35	3.01 ± 0.71	16.75 ± 0.29
Liu et al. (2015)	8.28	71.16	17.86	2.70	17.36
Kpalo et al. (2020)	9.27	74.39	13.92	2.42	16.13

5.3.2. Diffraction Patterns of the Catalysts

Figure 5.2 shows the powder X-ray diffraction (XRD) peaks at 7.90°, 8.80°, 23.11°, 23.82°, and 24.32°, indicating the consistent presence of the Mobil Five (MFI) crystalline topology. These peaks were observed in both the commercial and synthesized catalysts, confirming the ZSM-5 crystalline structure. However, the commercial catalyst exhibited larger and more refined peak intensities than

the synthesized catalyst. This difference can be attributed to the synthesized catalyst's lower crystallinity (%), as shown in ***Table 5.2***. In addition, an extra peak, at 29.2°, was observed in the synthesized catalyst, which can be attributed to the presence of trace metals (**Table *5.3***). This peak corresponds to Augite, an inorganic mineral commonly used to produce glass ceramics (Zhang et al., 2016). Jiang et al. (2014) successfully synthesized a high siliceous ZSM-5 zeolite using the hydrothermal method, starting from a fibrous clay material. The resulting synthesized zeolites exhibited characteristic peaks of ZSM-5 within the range of 7.8 – 23.9°, indicating the presence of the MFI crystalline structure.

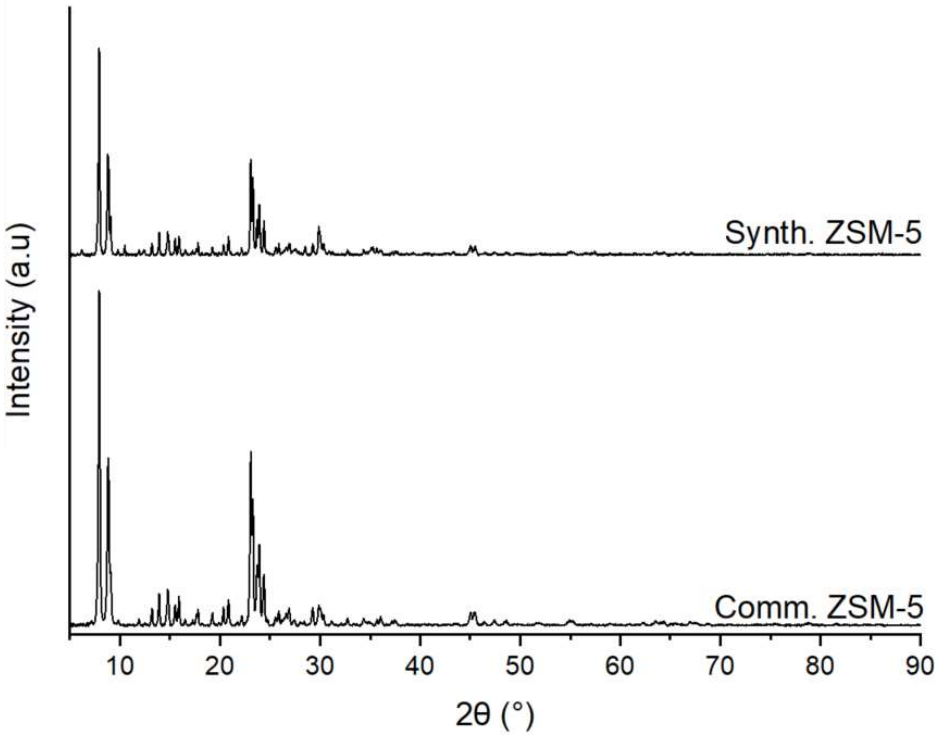

Figure 5.2. XRD patterns of commercial and synthesized catalysts.

5.3.3. Texture Properties of the Catalysts

Table 5.2 presents the texture properties of both the commercial and synthesized catalysts. The results indicate that the specific surface area of the synthesized catalyst was significantly lower (107.5 m^2/g) than that of the commercial catalyst (436. 4 m^2/g). This disparity can be attributed to the synthesized catalyst's incomplete crystallization (51.8%). The commercial catalyst displayed a two-level porous structure consisting of micro- and mesopores (0.105 cm^3/g), while the synthesized catalyst solely possessed a mesoporous structure (V_{micro} = n.d.). Furthermore, the synthesized catalyst exhibited a larger pore size of 15.6 nm, which offers advantageous capabilities to catalyze reactions from petrochemical manufacturing. Bai et al. (2019) asserted that the mesopores in the hierarchical ZSM-5 (HZSM-5) structure enhance the mass transfer of bulky organic molecules and facilitate access to active acid sites, thereby overcoming limitations related to steric hindrance, diffusion, and coke formation in catalytic reactions. That absence of a micropore structure ($10^{-6} < p/p_0 < 0.01$) in the synthesized catalyst was further confirmed by the physisorption isotherms (***Figure 5.3***). Both catalysts displayed a type-IV adsorption isotherm with distinct hysteresis loops, characteristic of capillary

condensation at high relative pressure. This confirms the presence of a mesoporous structure (Liu et al., 2014). Similar type-IV adsorption isotherms were observed during the synthesis of hierarchical ZSM-5 catalysts by Popova et al. (2021) and Nandiwale et al. (2015). In the region of high relative pressure ($p/p_0 > 0.6$), the synthesized ZSM-5 catalyst exhibited a steep hysteresis loop, which differed from the commercial catalyst, suggesting variations in the mesoporous and macroporous structures (Sing et al., 1985). The commercial catalyst displayed a type-H4 hysteresis loop, while a type-H1 hysteresis loop was observed in the synthesized catalyst.

Table 5.2. Structural properties of commercial and synthesized catalysts.

Catalyst	S_{BET} (m^2/g)	V_{tot} (cm^3/g)	V_{micro} (cm^3/g)	Pore diameter (nm)	Crystallinity (%)
Comm. ZSM-5	436,4	0,286	0,105	2,62	100
Synth. ZSM-5	107,5	0,421	n.d	15,6	51,8

n. d. = not detected

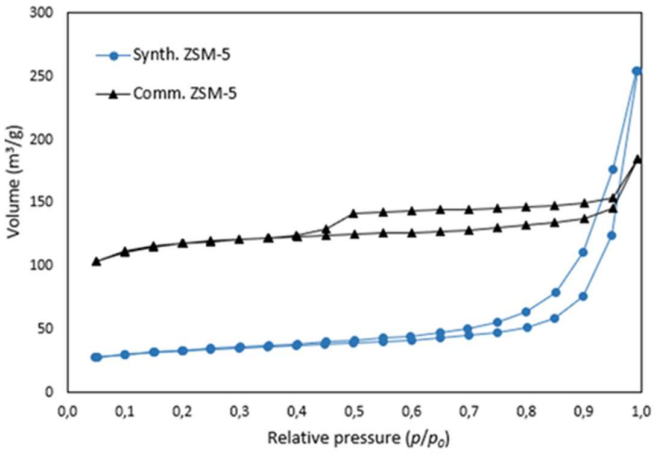

Figure 5.3. Physical adsorption isotherms.

5.3.4. Chemical Composition of the Catalysts

Table 5.3 compares the chemical composition of the synthesized and commercial catalysts. Both catalysts primarily consisted of high SiO_2, with fewer of Al_2O_3. Nevertheless, the synthesized catalyst contained additional compounds such as CaO, MgO, and trace metals. These additional compounds were inherited from blast furnace slag during the synthesis process. The loss on ignition constituted the residual composition, ensuring the total reached 100 wt.%. Alkaline earth metals (CaO and MgO) severely affect the zeolite synthesis process by impeding the nucleation of zeolite crystals (Kuwahara et al., 2009); thus, they are considered impurities. As such, the composition of impurities needs to be significantly low prior to synthesis. Considering that ZSM-5 is primarily used to catalyze reactions in the petrochemical industry, the presence of trace metals may enhance the catalytic reactivity of the material. Researchers have demonstrated that incorporating transitional metals into the porous structure of ZSM-5 offers the advantages of ion exchange and improved catalytic reactivity. Anekwe et al. (2024) synthesized a metal-modified ZSM-5 catalyst containing Ni, Co, and Fe for converting ethanol to hydrocarbons. It was reported that metal loading affects the physicochemical properties and catalytic performance of ZSM-5 catalysts.

Table 5.3. Chemical composition of the catalysts.

Compound	SiO_2	Al_2O_3	CaO	MgO	Fe_2O_3	MnO	Na_2O	K_2O	TiO_2	P_2O_5	Cr_2O_3	NiO	SiO_2/Al_2O_3 ratio
Comm. ZSM-5 (wt.%)	96.7	3.28	0	0	0	0	0	0	0	0	0	0	50
Synth. ZSM-5 (wt.%)	74.6	5.1	**5.2**	**3.0**	3.8	0.1	0.9	0.3	0.9	0.03	0.3	0.04	24.8

5.3.5. Effect of Temperature on Product Distribution

Figure 5.4 shows the influence of pyrolysis temperature on the product distribution. The biochar yield decreased from 28.8 to 6.8 wt.% as the temperature increased from 150 to 350°C. The decrease in biochar can be attributed to the primary decomposition of biomass at higher temperatures or through the secondary decomposition of the biochar residue (Demiral et al., 2012). However, this shows a positive effect of temperature on improving the pyrolysis conversion yield. The bio-oil and gas yields increased to a maximum of 32.5 and 60.7 wt.%, respectively, at a temperature of 350°C. The increase in bio-oil yield at higher temperatures is due to the devolatilization of organic matter into fragments, thus enforcing the re-polymerization and hydrolysis reactions to form bio-oil (Nizamuddin et al., 2019). The higher gas yield is attributed to the secondary cracking of the pyrolysis vapors at elevated temperatures. Furthermore, the higher temperatures prompt the secondary decomposition of the biochar, resulting in the generation of additional non-condensable gaseous products (Demiral & Ayan, 2011). These factors collectively contribute to the overall increase in gas yield, which correlates directly with the temperature increment during pyrolysis. It is worth noting that the heating rate was kept constant at 150 °C/min. The pyrolysis temperatures (150 – 350°C) considered in this study were significantly lower than conventional pyrolysis [~400 to ~600°C] (Kosanić et al., 2014) due to the efficient heating mechanism used by microwave-assisted pyrolysis. These temperature ranges (150 – 350°C) are often associated with the release of light volatiles, bond weakening, and, dehydroxylation which constitute the initial thermal degradation of biomass (Demiral et al., 2012). Wu et al. (2014) compared biomass pyrolysis using two heating mechanisms (microwave and conventional). The microwave setup was heated to 200°C, whereas the conventional setup was heated to 520°C. It was concluded that the microwave experiments were faster.

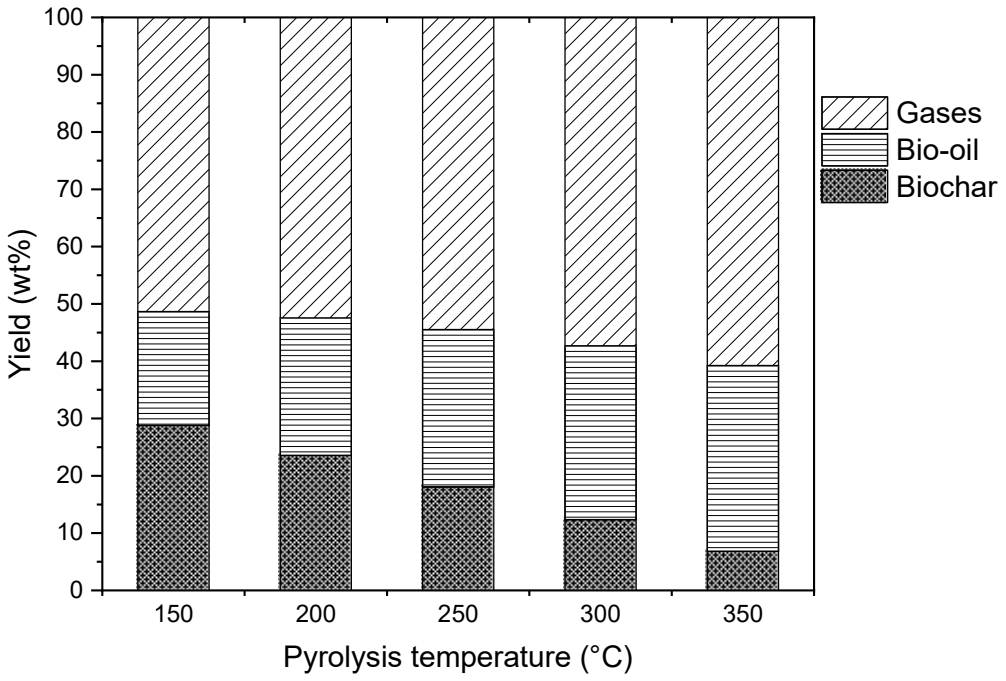

Figure 5.4. Effect of pyrolysis temperature on Product Distribution (time of 3 min & catalyst-to-biomass ratio of 1:9).

5.3.6. Effect of Catalyst-to-Biomass Ratio on Product Distribution

The application of a synthesized HZSM-5 catalyst in a microwave-assisted pyrolysis setup and the relationship between product distribution and the catalyst-to-biomass ratio are shown in ***Figure 5.5***. The catalyst-to-biomass ratio was found to be a crucial factor influencing the distribution and yield of products. The increase in the catalyst-to-biomass ratio from 1:9 to 1:2 decreased the bio-oil yield linearly from 32.5 to 22.9 wt.%, while the gas yield increased significantly from 39.8 to 69.9 wt.%. ZSM-5 is a bifunctional catalyst, that is, it promotes deoxygenation and shape-selectivity. The deoxygenation function depends on the number of acidic active sites in the catalyst, which yields various hydrocarbon species. The shape-selective function depends on the catalyst's internal pore structure, which screens the dynamic size/structure of the compound (such as benzene ring-containing chemicals). Therefore, a low catalyst-to-biomass ratio promotes shape-selectivity, and a high catalyst-to-biomass ratio promotes deoxygenation (Cai et al., 2018). The three-dimensional porous structure of the synthesized catalyst converts the larger molecules into smaller-sized gaseous hydrocarbons, which increases the gas yield (Liu et al., 2017). Furthermore, oxygen is converted to light gaseous products (CO_2, CO, and H_2O). A high catalyst-to-biomass ratio favors secondary reactions such as carbon deposition, polymerization, and cracking (Rahman et al., 2018). Therefore, the increase in the catalyst-to-biomass ratio results in bio-oil decomposition to yield more gaseous products (Naqvi et al., 2014). The biochar yield decreased from 27.7 to 7.2 wt.% with increased catalyst-to-biomass ratio. The re-usability of the synthesized catalyst was not carried out due to the difficulty of separating it from the homogeneous mixture (activated carbon and biochar) post-pyrolysis.

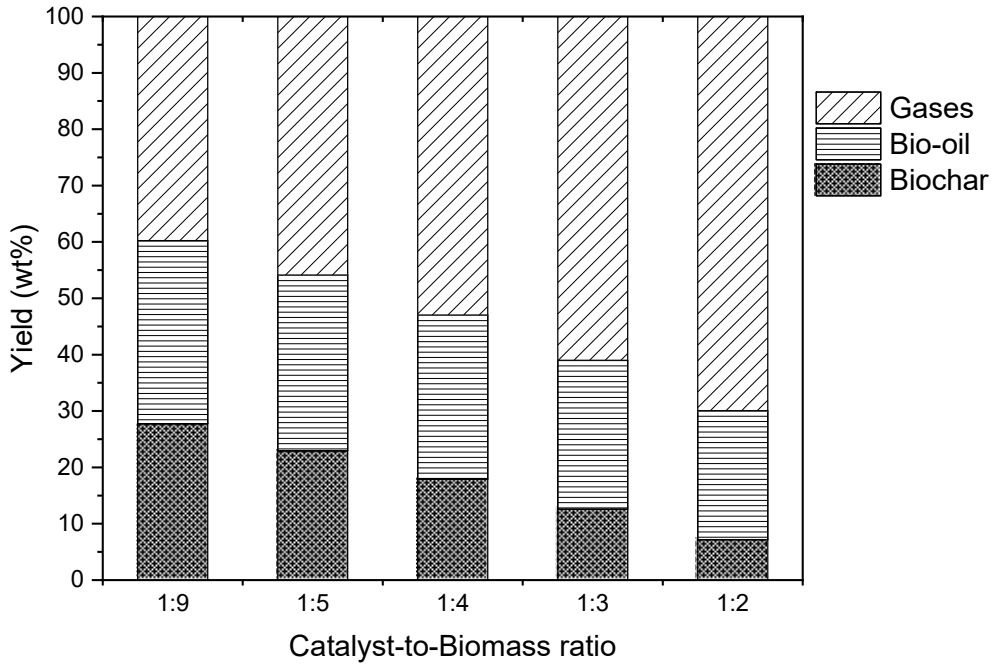

Figure 5.5. Effect of catalyst-to-biomass ratio on product distribution (time of 3 min & temperature of 350°C).

5.3.7. Effect of Time on Product Distribution

Figure 5.6 shows the influence of reaction time on the product distribution. The biochar and bio-oil yields decreased to 19.8 and 25.3 wt.%, respectively, as the reaction time was increased from 3 to 7 min. Inversely, the gas yield increased from 42.6 to 54.8 wt.% with an increase in reaction time. The impact of reaction time on the product distribution was comparatively less pronounced when compared to the influence of pyrolysis temperature (***Figure 5.4***) and the catalyst-to-biomass ratio [***Figure 5.5***] (Bu et al., 2012).

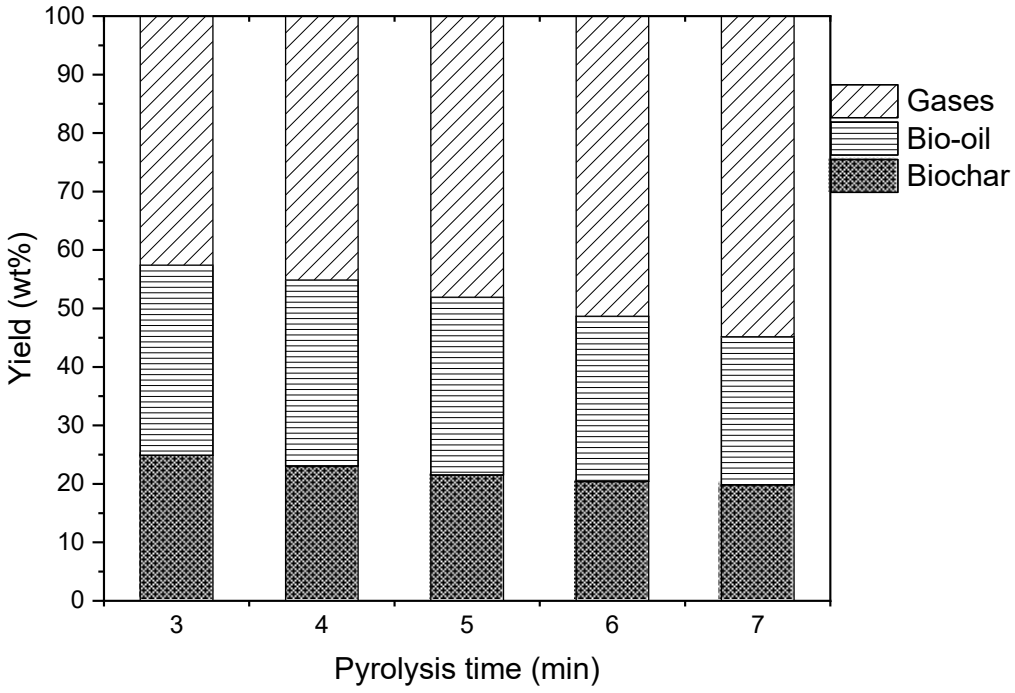

Figure 5.6. Effect of time on product distribution (temperature of 350°C & catalyst-to-biomass ratio of 1:9).

5.3.8. Bio-oil Conversion

Figure 5.7 shows the mass balance for the bio-oil conversion of the feedstock at maximum pyrolysis conditions: pyrolysis temperature = 350°C, pyrolysis time = 3 min, and catalyst-to-biomass ratio = 1:9. It is worth noting that the biomass experiments solely comprised of corn cob and activated carbon. A lower rate of conversion (26.9%) was observed during the thermal pyrolysis of the biomass (no catalyst). The conversion rate significantly increased, nearly two-fold, during the catalytic pyrolysis of the biomass. The acidic active sites in the catalysts act as deoxidizers, that is, the removal of the oxygen in the form of CO_2, CO, and H_2O vapor (Cai et al., 2018). Furthermore, the critical role of ZSM-5 during biomass pyrolysis is to deoxygenate the oxygenated intermediates and improve the bio-oil content selectively. Therefore, the bio-oil conversion was increased in the presence of the ZSM-5 catalyst due to the primary product vapors diffusing through the mesoporous crystalline structure of the catalyst, promoting cracking and upgrading reactions (Zhang et al., 2015). The commercial catalyst achieved a conversion rate of 41.9%, and the synthesized catalyst obtained 43.6%. The synthesized catalyst obtained relatively lower textural properties (107.5 m^2/g and 51.8% crystallinity) and contained trace metals (***Table 5.3***). Transitional metals in zeolite catalysts change the textural and acidic properties, thereby improving the catalytic behavior (Liang et al., 2021). This was shown by Botas et al. (2012), who incorporated Ni and Mo into ZSM-5 for pyrolytic biomass conversion into raw chemicals and fuels. There were variations in the acidic and textural properties of the impregnated catalysts, which resulted in improved catalytic activity.

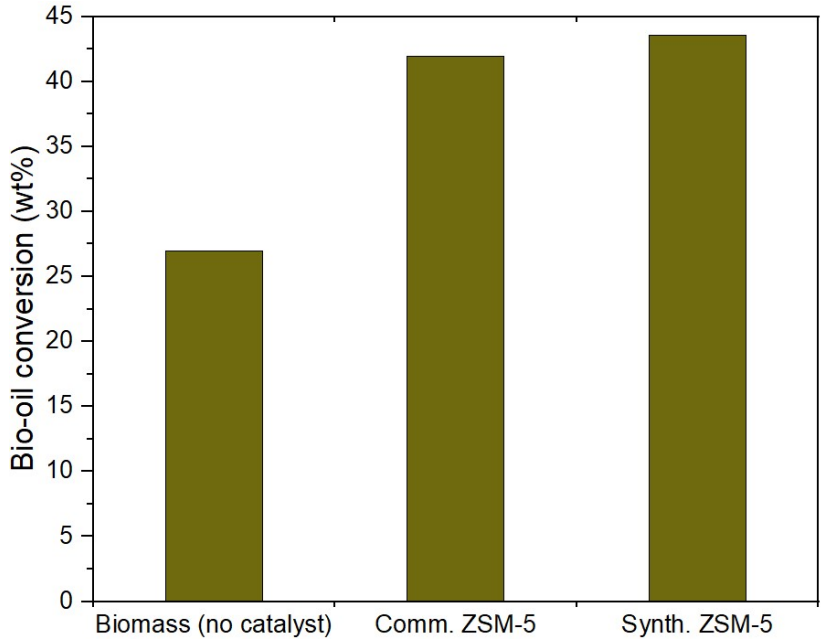

Figure 5.7. Effect of catalyst type on bio-oil conversion (350°C, 3 min, and 1:9).

5.3.9. Chemical Component Analysis of Bio-oil by GC-MS

Boi-oil consists of various compounds grouped based on their characteristic functional groups, such as phenols, esters, sugars, ketones furans, guaiacol, acids, and hydrocarbons. A more comprehensive list is provided in *Appendix C*. ***Figure 5.8*** shows the GC-MS analysis of these functional groups present in bio-oil obtained through the microwave-assisted pyrolysis of corn cob at maximum conditions (350°C, 3 min, and 1:9). The results indicated that the bio-oil obtained from all the experiments mainly consisted of acids, ketones/aldehydes, phenols, and alcohols. However, the selectivity shifted considerably based on the catalyst used. The selectivity of thermal pyrolysis was acids (27%), ketones/aldehydes (19.4%), phenols (20.6%), and alcohols (20.6%). Adding a catalyst significantly reduced the relative contents of acids, amine, and alcohols and produced esters (5.9% = commercial and 4.7% = synthesized). The reduction of oxygenated hydrocarbons is due to the decarbonylation, decarboxylation, and dehydration reactions occurring inside the porous structure of the catalysts (Zhang et al., 2012). The selectivity of the catalytic pyrolysis was towards phenols (28.8% = commercial and 23.2% = synthesized) and ketones/aldehydes (22.8% = commercial and 36.9% = synthesized), whereby the aromatic content was increased (8.1%) for the synthesized catalyst. ZSM-5 is a shape-selective catalyst whose porous structure affects the bio-oil composition based on the reactant, product, and transition-state shape selectivities. That is, reactant selectivity refers to reactants whose diameters are smaller than the catalyst's pore diameter, product selectivity refers to large organic molecules that can be cracked into smaller ones, and transition-state refers to the controlling of molecular traffic through the pore channels/cavities (Liang et al., 2021). Cai and Liu (2016) investigated the catalytic performance of biomass pyrolysis at a commercial scale (throughput of 1–3 ton/h) using a ZSM-5 catalyst. The bio-oil obtained consisted mainly of phenols (14.92%) and ketones (9.38%), amongst other oxygenated hydrocarbons.

Ketones play a crucial role as a chemical substance in various applications, such as extraction and synthesis of valuable compounds (Bu et al., 2018). Phenols and phenolic derivatives are formed during

the thermal decomposition (depolymerization) of lignin, which then diffuses into the ZSM-5 pores and is transformed into monoaromatic hydrocarbons (MAHs) through a series of deoxygenation reactions (Fan et al., 2018). The impregnation of transitional metals into ZSM-5 affects the oxygen release rejection by preferring decarboxylation and decarbonylation reactions, leaving more hydrogen available for aromatic compound formation. The presence of metallic species has been found to enhance the deoxygenation activities of zeolites significantly. However, it is essential to note that the specific effects on biomass pyrolysis routes can vary depending on the type of metal present. Ni has a selectivity towards phenols and aromatics (Iliopoulou et al., 2012), Mo has a selectivity towards aromatics (Botas et al., 2012), Zn has a selectivity towards aromatics and phenols (Wang et al., 2014), and Fe has a selectivity towards aromatics and furans (Li et al., 2021). The GC-MS results indicated that the bio-oil produced was rich in oxygenated hydrocarbons (phenols and ketones), which restricts the direct application of the bio-oil as a transportation fuel due to the low content of aromatic compounds (3.3 – 8.1%). However, oxygenated hydrocarbons are vital chemical substances in producing raw petrochemicals.

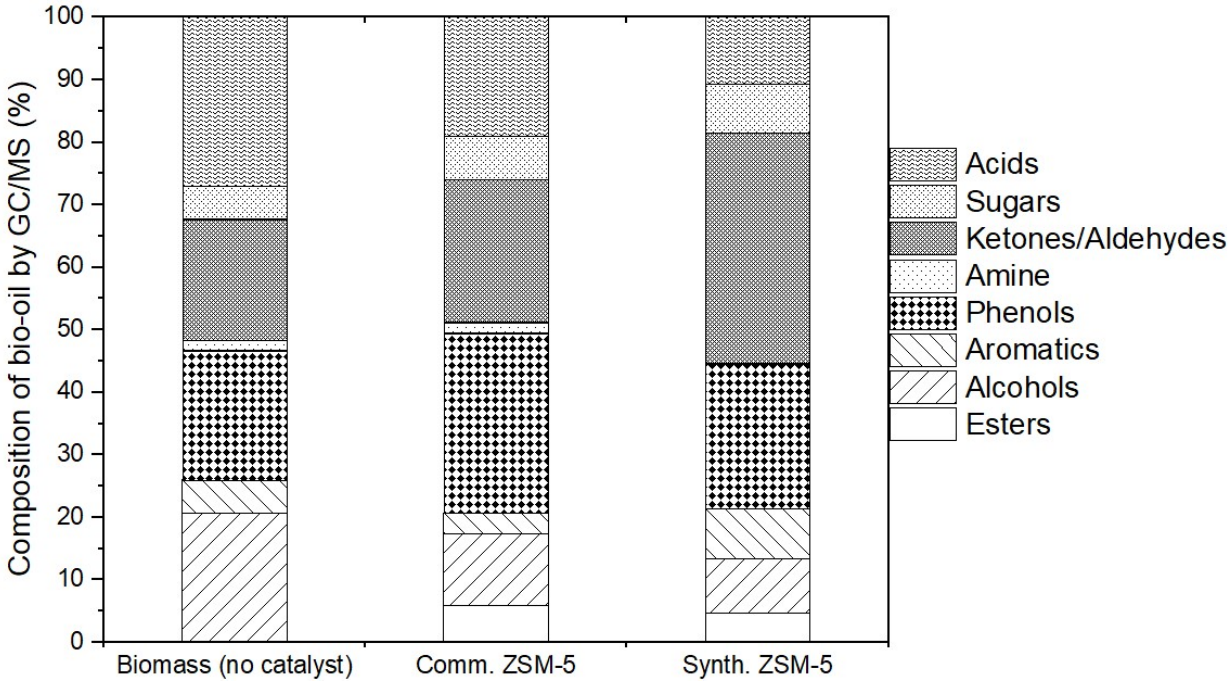

Figure 5.8. GC-MS analysis of the chemical composition of bio-oils.

5.3.10. Chemical Compounds Identified by GC-MS

The primary individual compounds in the pyrolysis oil samples are listed in ***Table 5.4***. Based on the results of the GC-MS analysis, it is evident that pyrolytic oils are intricate compositions of organic liquids with diverse chemicals. The GC-MS analysis detected hundreds of compounds, and the retention time ranged from 3.016 to 14.015 min. However, the identified chemicals have been segmented into various categories for better comprehension and assessment. A more comprehensive list is provided in *Appendix C*. The bio-oil derived from the catalytic (ZSM-5) microwave pyrolysis of corn cob exhibited a substantial amount of phenols and ketones (***Figure 5.8***). The most prominent chemical compounds in each functional group were cyclohexanone and ethenone for ketones, and the phenolic derivatives were cresol and catechol (***Table 5.4***). Ethanone is a type of ketene compound that

is highly reactive, consisting of a ketene structure (>C=C=O). It has several industrial applications, such as the manufacture of acetic acid, dye intermediates, medicines, and pesticides (Jiang et al., 2023). Cyclohexanone is used as an organic solvent in the textile and plastic industries. In contrast, phenols and phenol derivatives are prevalent structural motifs in pharmaceuticals, bulk chemicals, and polymers (Pun et al., 2013). Apart from the prevalent compounds identified under ketones and phenols, small amounts of benzaldehyde, stearic acid, ethylene carbonate, 3-hexadecyloxycarbonyl, and propanoic acid were also detected in the bio-oil. However, these chemical compounds are considered undesirable due to decreasing bio-oil quality. That is, organic acids and sugars promote acidity and corrosiveness of the bio-oil, esters reduce the heating value, and the aldehyde content causes instability during transportation and storage (Naqvi et al., 2014). In addition, the nitrogen-containing compounds (amine) are detrimental to the environment.

Table 5.4. Major compounds identified by GC-MS: Bio-oil from microwave-assisted pyrolysis of corn cob at maximum conditions.

Number	Residence time (min)	Compound name	Molecular formula	Functional Group	Area%		
					Biomass (no catalyst)	Comm. ZSM-5	Synth. ZSM-5
1	3,016	3-Hexadecyloxycarbonyl	$C_{24}H_{45}N_2O_3$	Ester	1,66	1,37	1,45
2	3.171/3.188	3-Chloro-2buten-1-ol	C_4H_7ClO	Alcohol	7,46	4,11	N.D.
3	3.319/3.249	Propanoic acid	$C_3H_6O_2$	Acid	4,16	7,6	N.D.
4	4.057/4.062/3.745	Cyclohexanone	$C_6H_{10}O$	Ketone	9,11	9,48	1,68
5	4.373/4.374	2-Isopropoxyethyl propionate	$C_8H_{16}O_3$	Ester	5,44	5,46	N.D.
6	4.738/4.739/4.725	Phenol, 4-methyoxy-	C_6H_5OH	Phenol	6,89	7,15	4,92
7	4.943/4.900	1,3-Dioxolan-2-one (ethylene carbonate)	$C_3H_4O_3$	Ester	0,73	N.D.	0,77
8	6.499/6.488	Creosol	$C_8H_{10}O_2$	Phenol	N.D.	1,4	1,02
9	6.850/6.850/6.849	1,2-Benzenediol (catechol)	$C_6H_6O_2$	Phenol	2,98	3,5	3,28
10	9.045/9.039	D-Allose	$C_6H_{12}O_6$	Sugar	2,84	2,32	N.D.
11	10.000/9.971/9.940	Benzaldehyde	C_7H_6O	Aldehyde	0,06	0,06	0,07
12	10.390/10.390/10.369	Ethanone	C_2H_2O	Ketone	0,02	0,05	0,04
13	12.505/13.399/13.357	Octadecanoic acid (stearic acid)	$C_{18}H_{36}O_2$	Acid	0,01	0,03	0,24

5.3.11. Chemical Composition of Gases

The gas composition presented in ***Table 5.5*** was measured against the maximum pyrolysis conditions of 350°C, 3 min, and 1:9. It was found that CO_2 and CO were the dominant gaseous products with contents of 46.1 and 28.1%, respectively. Carbon dioxide is usually released during the initial decomposition of biomass due to the cracking and reforming reactions of carbonyl and carboxyl groups. During the secondary thermal cracking of pyrolysis vapors, the production of CO is favored over CO_2 (Romero et al., 2022). Moderate production of H_2 (7.7%) and CH_4 (4.97%) was observed, with the light hydrocarbons (1.3%) being the least. Chen et al. (2014) showed that an increase in pyrolysis temperature (> 500°C) promotes the formation of C1–C3 hydrocarbons, whilst decreasing the CO_2. It was noted that H_2 was produced through aromatic cyclization and dehydrogenation of intermediate products (paraffins). This was further collaborated by Romero et al. (2022), who observed an increase in H_2, CH_4, CO, and C_nH_m at higher temperatures (>550°C), resulting in an

increase in the calorific value of the gas. Although the moderately low temperature used in this study positively influenced bio-oil and gas yields, it also favoured the production of CO_2 and CO.

Table 5.5. Pyrolysis gas composition.

Element	Area%
H_2	7.7 ± 0.515
CO	28.1 ± 0.346
CO_2	46.1 ± 0.609
CH_4	4.97 ± 0.893
Light hydrocarbons	1.3 ± 0.298

5.4. Conclusion

A ZSM-5 zeolite catalyst was successfully synthesized using slag waste from the iron- and steelmaking industry for the microwave-assisted pyrolysis of corn cob. Foreign trace metals in the catalyst's three-dimensional framework significantly impacted its physical properties. The XRD results verified the characteristic diffraction peaks indicative of the MFI crystalline topology. The crystalline structure of the synthesized catalyst exhibited mesopores (15.6 nm) with a relatively low specific surface area (107.5 m^2/g) and a SiO_2/Al_2O_3 ratio of 24.8. The impurities (CaO and MgO) remarkably influenced the synthesized catalyst's crystallinity (51.8%). The activity and selectivity of the catalyst are greatly influenced by factors such as catalyst composition and pore structure. These parameters play a crucial role in determining the performance of the catalyst. In addition, pyrolysis conditions such as catalyst-to-biomass ratio, time, and temperature were used to control the product distribution and the composition of the bio-oil. The maximum pyrolysis conditions were found to be pyrolysis temperature = 350°C, pyrolysis time = 3 min, and catalyst-to-biomass ratio = 1:9. The targeted primary product was bio-oil; however, the gas yield superseded that of the bio-oil. The production of phenol- and ketone-rich bio-oil can be achieved by microwave pyrolysis of corn cob under controlled experimental conditions. The synthesized ZSM-5 catalyst demonstrated similar catalytic efficiency in bio-oil conversion rates as the commercial ZSM-5 catalyst. The substantial content of ketones and phenols derived from this study indicates the potential use of microwave pyrolysis in producing fossil fuel substitutes after separating oxygenates for the chemical industry.

References

Ala-Kokko, K., Lanier Nalley, L., Shew, A. M., Tack, J. B., Chaminuka, P., Matlock, M. D., & D'Haese, M. (2021). Economic and ecosystem impacts of GM maize in South Africa. *Global Food Security*, *29*, 100544. https://doi.org/10.1016/j.gfs.2021.100544

Anekwe, I. M. S., Oboirien, B., & Isa, Y. M. (2024). Effects of transition metal doping on the properties and catalytic performance of ZSM-5 zeolite catalyst on ethanol-to-hydrocarbons conversion. *Fuel Communications*, *18*, 100101. https://doi.org/10.1016/J.JFUECO.2023.100101

Bai, R., Song, Y., Li, Y., & Yu, J. (2019). Creating Hierarchical Pores in Zeolite Catalysts. *Trends in Chemistry*, *1*(6), 601–611. https://doi.org/10.1016/j.trechm.2019.05.010

Botas, J. A., Serrano, D. P., García, A., De Vicente, J., & Ramos, R. (2012). Catalytic conversion of rapeseed oil into raw chemicals and fuels over Ni- and Mo-modified nanocrystalline ZSM-5 zeolite. *Catalysis Today*, *195*(1), 59–70. https://doi.org/10.1016/J.CATTOD.2012.04.061

Bu, Q., Lei, H., Ren, S., Wang, L., Zhang, Q., Tang, J., & Ruan, R. (2012). Production of phenols and biofuels by catalytic microwave pyrolysis of lignocellulosic biomass. *Bioresource Technology*, *108*, 274–279. https://doi.org/10.1016/j.biortech.2011.12.125

Bu, Q., Liu, Y., Liang, J., Morgan, H. M., Yan, L., Xu, F., & Mao, H. (2018). Microwave-assisted co-pyrolysis of microwave torrefied biomass with waste plastics using ZSM-5 as a catalyst for high quality bio-oil. *Journal of Analytical and Applied Pyrolysis*, *134*, 536–543. https://doi.org/10.1016/j.jaap.2018.07.021

Cai, W., Dai, L., & Liu, R. (2018). Catalytic fast pyrolysis of rice husk for bio-oil production. *Energy*, *154*, 477–487. https://doi.org/10.1016/j.energy.2018.04.157

Cai, W., & Liu, R. (2016). Performance of a commercial-scale biomass fast pyrolysis plant for bio-oil production. *Fuel*, *182*, 677–686. https://doi.org/10.1016/J.FUEL.2016.06.030

Chen, G., Liu, C., Ma, W., Zhang, X., Li, Y., Yan, B., & Zhou, W. (2014). Co-pyrolysis of corn cob and waste cooking oil in a fixed bed. *Bioresource Technology*, *166*, 500–507. https://doi.org/10.1016/j.biortech.2014.05.090

Demiral, I., & Ayan, E. A. (2011). Pyrolysis of grape bagasse: Effect of pyrolysis conditions on the product yields and characterization of the liquid product. *Bioresource Technology*, *102*(4), 3946–3951. https://doi.org/10.1016/j.biortech.2010.11.077

Demiral, I., Eryazici, A., & Şensöz, S. (2012). Bio-oil production from pyrolysis of corncob (Zea mays L.). *Biomass and Bioenergy*, *36*, 43–49. https://doi.org/10.1016/j.biombioe.2011.10.045

Fan, L., Chen, P., Zhou, N., Liu, S., Zhang, Y., Liu, Y., Wang, Y., Omar, M. M., Peng, P., Addy, M., Cheng, Y., & Ruan, R. (2018). In-situ and ex-situ catalytic upgrading of vapors from microwave-assisted pyrolysis of lignin. *Bioresource Technology*, *247*, 851–858. https://doi.org/10.1016/j.biortech.2017.09.200

Grams, J., & Ruppert, A. M. (2021). Catalyst stability—bottleneck of efficient catalytic pyrolysis. In *Catalysts* (Vol. 11, Issue 2, pp. 1–24). MDPI. https://doi.org/10.3390/catal11020265

Iliopoulou, E. F., Stefanidis, S. D., Kalogiannis, K. G., Delimitis, A., Lappas, A. A., & Triantafyllidis, K. S. (2012). Catalytic upgrading of biomass pyrolysis vapors using transition metal-modified ZSM-5 zeolite. *Applied Catalysis B: Environmental*, *127*, 281–290. https://doi.org/10.1016/J.APCATB.2012.08.030

Jiang, H., Xu, Y., Li, G., Yang, G., Zhang, M., Shu, X., & Wang, L. (2023). Proof-of-Concept of ketene chemistry: Experimental and theoretical calculations on the synthesis of p-methoxyacetophenone from ethenone with anisole. *Molecular Catalysis*, *551*. https://doi.org/10.1016/j.mcat.2023.113633

Jiang, J., Duanmu, C., Yang, Y., Gu, X., & Chen, J. (2014). Synthesis and characterization of high siliceous ZSM-5 zeolite from acid-treated palygorskite. *Powder Technology*, *251*, 9–14. https://doi.org/10.1016/j.powtec.2013.10.020

Kosanić, T. R., Ćeranić, M. B., Crossed D Signurić, S. N., Grković, V. R., Milotić, M. M., & Brankov, S. D. (2014). Experimental investigation of pyrolysis process of woody biomass mixture. *Journal of Thermal Science*, *23*(3), 290–296. https://doi.org/10.1007/s11630-014-0709-3

Kpalo, S. Y., Zainuddin, M. F., Manaf, L. A., & Roslan, A. M. (2020). Production and characterization of hybrid briquettes from corncobs and oil palm trunk bark under a low pressure densification technique. *Sustainability (Switzerland)*, *12*(6). https://doi.org/10.3390/su12062468

Kuwahara, Y., Ohmichi, T., Kamegawa, T., Mori, K., & Yamashita, H. (2009). A novel synthetic route to hydroxyapatite–zeolite composite material from steel slag: investigation of synthesis mechanism and evaluation of physicochemical properties. *Journal of Materials Chemistry*, *19*(39), 7263–7272. https://doi.org/10.1039/B911177H

Li, J., Li, X., Zhou, G., Wang, W., Wang, C., Komarneni, S., & Wang, Y. (2014). Catalytic fast pyrolysis of biomass with mesoporous ZSM-5 zeolites prepared by desilication with NaOH solutions. *Applied Catalysis A: General*, *470*, 115–122. https://doi.org/10.1016/j.apcata.2013.10.040

Li, Y., Nishu, Yellezuome, D., Chai, M., Li, C., & Liu, R. (2021). Catalytic pyrolysis of biomass over Fe-modified hierarchical ZSM-5: Insights into mono-aromatics selectivity and pyrolysis behavior using Py-GC/MS and TG-FTIR. *Journal of the Energy Institute*, *99*, 218–228. https://doi.org/10.1016/J.JOEI.2021.09.013

Liang, J., Morgan, H. M., Liu, Y., Shi, A., Lei, H., Mao, H., & Bu, Q. (2017). Enhancement of bio-oil yield and selectivity and kinetic study of catalytic pyrolysis of rice straw over transition metal modified ZSM-5 catalyst. *Journal of Analytical and Applied Pyrolysis*, *128*, 324–334. https://doi.org/10.1016/j.jaap.2017.09.018

Liang, J., Shan, G., & Sun, Y. (2021). Catalytic fast pyrolysis of lignocellulosic biomass: Critical role of zeolite catalysts. In *Renewable and Sustainable Energy Reviews* (Vol. 139). Elsevier Ltd. https://doi.org/10.1016/j.rser.2021.110707

Liu, C., Kong, D., & Guo, H. (2014). The morphology control of zeolite ZSM-5 by regulating the polymerization degree of silicon and aluminum sources. *Microporous and Mesoporous Materials*, *193*, 61–68. https://doi.org/10.1016/J.MICROMESO.2014.03.015

Liu, X., Chen, M., & Wei, Y. (2015). Combustion behavior of corncob/bituminous coal and hardwood/bituminous coal. *Renewable Energy*, *81*, 355–365. https://doi.org/10.1016/j.renene.2015.03.021

Liu, S., Zhang, Y., Fan, L., Zhou, N., Tian, G., Zhu, X., Cheng, Y., Wang, Y., Liu, Y., Chen, P., & Ruan, R. (2017). Bio-oil production from sequential two-step catalytic fast microwave-assisted biomass pyrolysis. *Fuel*, *196*, 261–268. https://doi.org/10.1016/j.fuel.2017.01.116

Mohamed, B. A., Kim, C. S., Ellis, N., & Bi, X. (2016). Microwave-assisted catalytic pyrolysis of switchgrass for improving bio-oil and biochar properties. *Bioresource Technology*, *201*, 121–132. https://doi.org/10.1016/j.biortech.2015.10.096

Nandiwale, K. Y., Pande, A. M., & Bokade, V. V. (2015). One step synthesis of ethyl levulinate biofuel by ethanolysis of renewable furfuryl alcohol over hierarchical zeolite catalyst. *RSC Advances*, *5*(97), 79224–79231. https://doi.org/10.1039/c5ra13520f

Naqvi, S. R., Uemura, Y., & Yusup, S. B. (2014). Catalytic pyrolysis of paddy husk in a drop type pyrolyzer for bio-oil production: The role of temperature and catalyst. *Journal of Analytical and Applied Pyrolysis*, *106*, 57–62. https://doi.org/10.1016/j.jaap.2013.12.009

Nizamuddin, S., Baloch, H. A., Mubarak, N. M., Riaz, S., Siddiqui, M. T. H., Takkalkar, P., Tunio, M. M., Mazari, S., & Bhutto, A. W. (2019). Solvothermal Liquefaction of Corn Stalk: Physico-Chemical Properties of Bio-oil and Biochar. *Waste and Biomass Valorization*, *10*(7), 1957–1968. https://doi.org/10.1007/s12649-018-0206-0

Popova, M., Szegedi, Á., Oykova, M., Lazarova, H., Koseva, N., Mihályi, M. R., & Shestakova, P. (2021). Selective production of phenol on bifunctional, hierarchical zsm-5 zeolites. *Molecules*, *26*(12). https://doi.org/10.3390/molecules26123576

Pun, D., Diao, T., & Stahl, S. S. (2013). Aerobic dehydrogenation of cyclohexanone to phenol catalyzed by Pd(TFA)2/2-dimethylaminopyridine: Evidence for the role of Pd nanoparticles. *Journal of the American Chemical Society*, *135*(22), 8213–8221. https://doi.org/10.1021/JA403165U/SUPPL_FILE/JA403165U_SI_001.PDF

Rahman, M. M., Liu, R., & Cai, J. (2018). Catalytic fast pyrolysis of biomass over zeolites for high quality bio-oil – A review. In *Fuel Processing Technology* (Vol. 180, pp. 32–46). Elsevier B.V. https://doi.org/10.1016/j.fuproc.2018.08.002

Ravikumar, C., Senthil Kumar, P., Subhashni, S. K., Tejaswini, P. V., & Varshini, V. (2017). Microwave assisted fast pyrolysis of corn cob, corn stover, saw dust and rice straw: Experimental investigation on bio-oil yield and high heating values. *Sustainable Materials and Technologies*, *11*, 19–27. https://doi.org/10.1016/j.susmat.2016.12.003

Romero, M., German, B., Rivadeneira, D., Chulde, D., Proano, A. C., Narváez, R. A. C., & Gómez, J. M. (2022). Assessment of Pilot Scale Pyrolysis Gas Production as Fuel for Cogeneration. *Chemical Engineering Transactions*, *92*, 211–216. https://doi.org/10.3303/CET2292036

Shang, H., Lu, R. R., Shang, L., & Zhang, W. H. (2015). Effect of additives on the microwave-assisted pyrolysis of sawdust. *Fuel Processing Technology*, *131*, 167–174. https://doi.org/10.1016/j.fuproc.2014.11.025

Sing, K. S. W., Everett, D. H., Haul, R. A. W., Moscou, L., Pierotti, R. A., Rouquerol, J., & Siemieniewska, T. (1985). Reporting physisorption data for gas/solid systems-with special reference to the determination of surface area and porosity. *Pure & App. Chem.*, *57*(4), 603–619.

Suriapparao, D. V., Pradeep, N., & Vinu, R. (2015). Bio-oil production from Prosopis juliflora via microwave pyrolysis. *Energy and Fuels*, *29*(4), 2571–2581. https://doi.org/10.1021/acs.energyfuels.5b00357

Wang, L., Lei, H., Bu, Q., Ren, S., Wei, Y., Zhu, L., Zhang, X., Liu, Y., Yadavalli, G., Lee, J., Chen, S., & Tang, J. (2014). Aromatic hydrocarbons production from ex situ catalysis of pyrolysis vapor over Zinc modified ZSM-5 in a packed-bed catalysis coupled with microwave pyrolysis reactor. *Fuel*, *129*, 78–85. https://doi.org/10.1016/J.FUEL.2014.03.052

Wu, C., Budarin, V. L., Gronnow, M. J., De Bruyn, M., Onwudili, J. A., Clark, J. H., & Williams, P. T. (2014). Conventional and microwave-assisted pyrolysis of biomass under different heating rates. *Journal of Analytical and Applied Pyrolysis*, *107*, 276–283. https://doi.org/10.1016/j.jaap.2014.03.012

Yildiz, G., Ronsse, F., Duren, R. Van, & Prins, W. (2016). Challenges in the design and operation of processes for catalytic fast pyrolysis of woody biomass. In *Renewable and Sustainable Energy Reviews* (Vol. 57, pp. 1596–1610). Elsevier Ltd. https://doi.org/10.1016/j.rser.2015.12.202

Zhang, B., Zhong, Z., Chen, P., & Ruan, R. (2015). Microwave-assisted catalytic fast pyrolysis of biomass for bio-oil production using chemical vapor deposition modified HZSM-5 catalyst. *Bioresource Technology*, *197*, 79–84. https://doi.org/10.1016/j.biortech.2015.08.063

Zhang, H., Carlson, T. R., Xiao, R., & Huber, G. W. (2012). Catalytic fast pyrolysis of wood and alcohol mixtures in a fluidized bed reactor. *Green Chemistry*, *14*(1), 98–110. https://doi.org/10.1039/C1GC15619E

Zhang, H., Xiao, R., Jin, B., Shen, D., Chen, R., & Xiao, G. (2013). Catalytic fast pyrolysis of straw biomass in an internally interconnected fluidized bed to produce aromatics and olefins: Effect of different catalysts. *Bioresource Technology*, *137*, 82–87. https://doi.org/10.1016/j.biortech.2013.03.031

Zhang, S., Yang, J., Liu, B., Pan, D., Wu, C., & Volinsky, A. A. (2016). One-step Crystallization Kinetic Parameters of the Glass-ceramics Prepared from Stainless Steel Slag and Pickling Sludge. *JOURNAL OF IRON AND STEEL RESEARCH*, *23*(3), 220–224.

Zhou, X., Liu, Y., Meng, X., Shen, B., & Xiao, F. (2013). Synthesis and catalytic cracking performance of Fe/Ti-ZSM-5 zeolite from attapulgite mineral. *Cuihua Xuebao/Chinese Journal of Catalysis*, *34*(8), 1504–1512. https://doi.org/10.1016/S1872-2067(12)60638-X

CHAPTER 6

6.1. Overall Conclusion

This study successfully demonstrated the feasibility of using blast furnace slag (BFS) as a sustainable precursor for ZSM-5 synthesis through a microwave-assisted hydrothermal process. The optimized conditions facilitated the selective removal of Ca and Mg while preserving the silica-alumina framework necessary for zeolite formation. The resulting ZSM-5 exhibited moderate crystallinity with mesoporous properties, indicating its potential for catalytic applications. However, the presence of residual impurities such as Fe_2O_3 and MnO may influence catalytic performance, warranting further investigation. Future research should focus on enhancing the purity of BFS-derived ZSM-5, optimizing synthesis conditions through multivariate approaches, and evaluating its long-term stability in catalytic processes.

The slag waste analysis revealed that the major compounds present were Al_2O_3 (16.1 wt.%), CaO (30.6 wt.%), SiO_2 (35.1 wt.%), and MgO (10.5 wt.%). Acid leaching was performed to reduce the levels of CaO and MgO, which resulted in the final composition of 4.83 wt.% and 2.54 wt.%, respectively. Further examination of the slag waste's chemical composition revealed the presence of trace elements (Fe_2O_3, MnO, Na_2O, K_2O, TiO_2, P_2O_5, and Cr_2O_3), which were attributed to the raw materials (iron ore or iron scrap) used during the production of molten iron. The acid leaching process was optimized and achieved leaching efficiencies of 71.1% and 80.4% for Mg and Ca, respectively. The highest leaching efficiencies were attained under the following optimized conditions: 8 wt% solids concentration, 90 min leaching time, and 3 mol/L HCl concentration. Morphological analysis of both the raw and pretreated slags showed irregular-shaped stonelike formations with varying particle sizes and fibrous surfaces. However, the mineral composition was determined to be akermanite for the raw slag and augite for the pretreated slag. The acid-leaching process not only reduced the presence of impurities (CaO and MgO) but also transformed the mineral composition of the slags from akermanite to augite. A comparative study was conducted to utilize both the raw and pretreated slags to synthesize zeolitic materials, and it was observed that the composition of CaO and MgO in the starting material significantly impacted the zeolite synthesis process. That is, higher levels of CaO and MgO during synthesis led to the formation of complex calcium- and magnesium-aluminosilicate minerals (gehlenite, tobermorite, hydrogarnet, or augite), while lower levels resulted in the formation of zeolitic materials (ZSM-5). Consequently, the pretreated slag proved successful in the synthesis of ZSM-5.

The prevalent technique of hydrothermal synthesis, traditionally employed in the creation of zeolite, has garnered increasing scrutiny due to its harsh synthesis conditions, which are prolonged reaction periods, substantial energy requirements, and the nature of feed materials used. Consequently, the current research employs the principles of green chemistry with the hydrothermal synthesis technique in a bid to enhance the production of ZSM-5. That is, the coupling was achieved via the utilization of an industrial byproduct (namely pretreated slag) as a feed material, and the application of microwave radiation as a heat source. The microwave-assisted hydrothermal synthesis technique effectively transformed the aforementioned slag into ZSM-5. Following its synthesis, the resultant ZSM-5 was subjected to a comprehensive characterization process to interpret its physiochemical properties, in comparison to the commercially available ZSM-5. Key parameters under investigation included synthesis time and temperature, with significant discoveries found. It was reported that the size of the resultant crystals was heavily dependent on the synthesis temperature, whilst the shape was

predominantly influenced by the synthesis time. The ideal synthesis conditions were realized to be 13 hours at 180°C. The ZSM-5 produced under those conditions was observed to possess major characteristic diffraction peaks similar to commercial ZSM-5, though the additional peaks detected were attributed to the presence of minor quantities of augite. The synthesized ZSM-5 was comprised of well-defined cubic prism shapes with small intergrown rectangular crystals. The morphology of the crystals was observed to fluctuate in response to variations in synthesis time. Subsequent analysis of the crystalline structure revealed moderate crystallinity (52.4%) with a mesoporous structure. A relatively high pore size (14.8 nm) was noted, alongside a low BET surface area (108.4 m2/g). Adjustments in synthesis conditions (namely time and temperature) demonstrated no discernible impact on the chemical composition of the resultant product, which was classified as a high-silica zeolite (Si/Al ratio of 11.9). A low-cost procedure of infrared analysis was employed to examine the structural framework of the synthesized zeolite. The FTIR analysis confirmed the structural characteristics of the synthesized ZSM-5 and provided insights into its crystallization behavior. The absence of a silanol (Si-OH) stretching band between 3400 – 3600 cm^{-1} suggests effective condensation of the zeolite framework. The commercial ZSM-5 exhibited well-defined vibrational bands whilst the synthesized ZSM-5 samples obtained at lower temperatures (90–150°C) and shorter crystallization times (5–7 h) lacked the 1224 and 546 cm^{-1} bands, confirming incomplete crystallization. Additionally, the sawtooth peak at 426 cm^{-1}, present in commercial ZSM-5, was absent in the synthesized samples, further indicating lower crystallinity and structural order.

Zeolite Socony Mobil-5 (ZSM-5) is a widely used catalyst in the petrochemical industry, facilitating complex chemical reactions. In this study, the catalytic performance and selectivity of the synthesized ZSM-5 were evaluated during microwave-assisted pyrolysis of corn cob. Corn cob was selected as a suitable lignocellulosic biomass substrate due to its high volatile matter content of 75.98 wt.%. To compare the performance of the synthesized catalyst, commercial ZSM-5 was used as a reference. The results revealed that the activity and selectivity of a catalyst were significantly influenced by its crystalline structure, chemical composition, and other factors. Interestingly, the synthesized ZSM-5 demonstrated a comparable bio-oil conversion rate to that of the commercial catalyst, which could be attributed to the presence of trace metal elements (Fe_2O_3, MnO, Na_2O, K_2O, TiO_2, P_2O_5, and Cr_2O_3). The product distribution was found to be significantly affected by various pyrolysis conditions, such as catalyst-to-biomass ratio, pyrolysis time, and pyrolysis temperature. Particularly, the pyrolysis temperature had a positive effect on improving the pyrolysis conversion rate. Furthermore, the catalyst-to-biomass ratio played a crucial role, where a higher ratio promoted deoxygenation while a lower ratio resulted in shape selectivity. This revealed the bifunctional nature of the synthesized catalyst. Interestingly, the impact of pyrolysis time on the product distribution was minimal. The maximum pyrolysis conditions were determined to be 350°C, 3 minutes, and a catalyst-to-biomass ratio of 1:9. The primary product obtained from the pyrolysis was bio-oil, although the gas yield surpassed that of the oil. Both catalysts exhibited selectivity towards phenols and ketones; however, the composition varied significantly. The most prominent chemical compounds identified in each group were catechol and cresol for phenols, and ethenone and cyclohexanone for ketones. The significant presence of ketones and phenols in the bio-oil obtained from this study highlights the potential applicability of the synthesized ZSM-5 catalyst for bio-oil production.

6.1. Recommendations and Future Work

The pretreatment process successfully reduced the composition of CaO and MgO. However, the acid used (HCl) is a strong mineral acid that now contains dissolved CaO and MgO post-leaching. This, in turn, has created a secondary waste stream that needs to be neutralized. The solubilized CaO and MgO can be recovered using processes such as crystallization, solvent extraction, or precipitation. Investigating the reaction kinetics of the acid-leaching process can be beneficial in providing a detailed analysis of the optimization study.

During the leaching of the raw slag, a significant amount of Al_2O_3 was solubilized. This resulted in an increase in the Si/Al ratio of the synthesized ZSM-5. The acid properties of ZSM-5 are mainly dependent on the composition of Al_2O_3. Therefore, varying the Si/Al ratio of ZSM-5 would alter the composition of active acid sites, which are responsible for promoting the complex chemical reactions found during the pyrolysis of lignocellulosic biomass. Furthermore, analysis of the catalyst's acid properties using NH_3-TPD is recommended. The crystallinity of the synthesized catalyst was found to be moderate (52.4%); therefore, broadening the synthesis conditions would provide valuable information to improve the crystallinity.

The characterization of corn cob should be extended to include elemental analysis (C, H, O, S, and N) and lignocellulosic content (lignin, hemicellulose, and cellulose). Characterization of the biochar should be conducted to understand its physicochemical properties. The physical properties of the bio-oil produced should be determined in comparison to commercial fuels (diesel, jet fuel, and gasoline). Considering that the synthesized catalyst inherited trace elements (Fe_2O_3, MnO, Na_2O, K_2O, TiO_2, P_2O_5, and Cr_2O_3) in its crystalline structure, the effect of each metal element should be investigated to determine its impact during the pyrolysis of lignocellulosic biomass. During the start of the pyrolysis process, the catalyst is evenly mixed with corn cob to form a homogenous mixture; this prevents the recovery of the catalyst post-pyrolysis, thus limiting the ability to investigate the catalyst's reusability. Thus, it is recommended that the catalyst bed be separated from the feedstock (ex-situ pyrolysis).

7. APPENDICES

7.1 Appendix A (Acid Leaching Experiments)

Table 7.1. Leaching Efficiency

Run	Factor 1 A: Raw slag conc. wt.%	Factor 2 B: HCl conc. mol/L	Factor 3 C: Leaching time min	Response 1 Ca extraction ppm	Response 2 Mg extraction ppm
1	5	2	90	5917	480
2	2	1	90	2038	324
3	8	1	90	18754	1234
4	2	3	90	7337	650
5	2	2	150	7937	621
6	8	2	150	30714	3407
7	5	2	90	21565	2394
8	5	2	90	14831	1277
9	5	3	150	23190	2425
10	8	3	90	30289	3947
11	5	2	90	16339	1498
12	8	2	30	25634	3157
13	5	1	150	14788	1028
14	5	3	30	16749	1317
15	2	2	30	5112	673
16	5	1	30	10660	407
17	5	2	90	16061	1637

Table 7.2. Elemental composition of powdered samples.

Element	Raw Slag		Pretreated slag		Zeolite ZSM-5	
	Weight%	Atomic%	Weight%	Atomic%	Weight%	Atomic%
O	48,09	63,38	53,07	66,47	51,45	65,05
Na	1,52	1,39	1,74	1,51	0,74	0,65
Mg	8,83	7,76	0,56	0,46	0,87	0,73
Al	10,36	8,09	10,84	8,05	2,94	2,2
Si	14,64	11,03	30,99	22,11	42,47	30,59
Ca	12,81	6,75	2,8	1,4	1,53	0,77
Ti	2,84	1,25	n.d.	n.d.	n.d.	n.d.
Mn	0,91	0,35	n.d.	n.d.	n.d.	n.d.

n.d. = not detected.

Table 7.3. Analysis of variance for Ca leaching experiments.

Source	Sum of Squares	df	Mean Square	F-value	p-value
Model	7468.38	9	829.82	104.68	< 0.0001
A-Raw slag conc.	6110.65	1	6110.65	770.81	< 0.0001
B-HCl conc.	843.37	1	843.37	106.38	< 0.0001
C-Time	299.64	1	299.64	37.8	0.0005
AB	76.56	1	76.56	9.66	0.0171
AC	9	1	9	1.14	0.322
BC	9.49	1	9.49	1.2	0.3102
A^2	6.09	1	6.09	0.768	0.4099
B^2	63.8	1	63.8	8.05	0.0252
C^2	55.56	1	55.56	7.01	0.0331
Residual	55.49	7	7.93		
Lack of Fit	18.54	3	6.18	0.6692	0.6139
Pure Error	36.95	4	9.24		
Cor Total	7523.87	16			

df = degrees of freedom.

Table 7.4. Analysis of variance for Mg leaching experiments.

Source	Sum of Squares	df	Mean Square	F-value	p-value
Model	5755.87	9	639.54	22.44	0.0002
A-Raw slag conc.	3637.62	1	3637.62	127.64	< 0.0001
B-HCl conc.	1157.77	1	1157.77	40.63	0.0004
C-Time	150.42	1	150.42	5.28	0.0552
AB	461.82	1	461.82	16.21	0.005
AC	7.37	1	7.37	0.2587	0.6267
BC	19.27	1	19.27	0.6763	0.438
A^2	192.94	1	192.94	6.77	0.0353
B^2	118.42	1	118.42	4.16	0.0809
C^2	23.54	1	23.54	0.8259	0.3937
Residual	199.49	7	28.5		
Lack of Fit	162.3	3	54.1	5.82	0.0609
Pure Error	37.18	4	9.3		
Cor Total	5955.36	16			

df = degrees of freedom.

7.2. Appendix B (Microwave-assisted Pyrolysis Experiments)

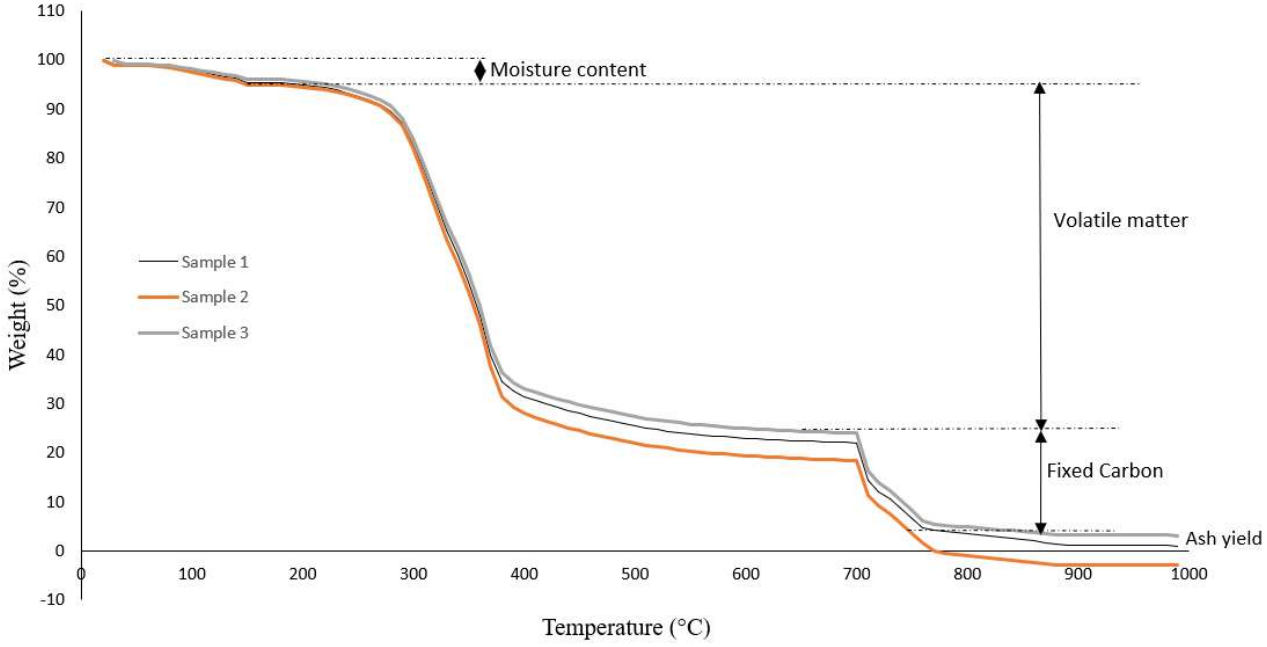

Figure 7.1. Thermogravimetric analysis of corn cob.

7.3. Appendix C (Compounds Identified by GC-MS)

Table 7.5. List of compounds identified by GC-MS.

Peak Report TIC

Peak#	R.Time	I.Time	F.Time	Area	Area%	Height	Height%	A/H	Mark	Name
1	3.016	3.005	3.105	30093381	2.76	13525451	7.82	2.22		5-Hexen-2-ol, 5-methyl-
2	3.156	3.105	3.185	21284130	1.95	4996482	2.89	4.26	V	L-5-Propylthiomethylhydantoin
3	3.214	3.185	3.265	22822103	2.09	5068266	2.93	4.50	V	Furan-2-carbonyl chloride, tetrahydro-
4	3.309	3.265	3.535	68420024	6.27	6100818	3.53	11.21	V	2-Propanone, 1-(acetyloxy)-
5	3.550	3.535	3.695	20234347	1.85	3101712	1.79	6.52	V	1,3-Propanediol, diacetate (CAS)
6	3.948	3.695	3.985	40013164	3.66	3319533	1.92	12.05	V	Dihydropyran
7	4.056	3.985	4.240	48786833	4.47	4042180	2.34	12.07	V	1,2-Cyclopentanedione
8	4.299	4.240	4.350	17670098	1.62	2983402	1.72	5.92	V	2-Isopropoxyethyl propionate
9	4.392	4.350	4.605	31850395	2.92	2970581	1.72	10.72	V	2-Cyclopenten-1-one, 3-methyl- (CAS)
10	4.743	4.605	4.895	64407868	5.90	6663843	3.85	9.67	V	Phenol (CAS)
11	4.976	4.895	5.005	12888129	1.18	2089712	1.21	6.17	V	1,3-DIOXOLAN-2-ONE, 4-METHYL-
12	5.057	5.005	5.215	49597234	4.54	6930422	4.01	7.16	V	2-Cyclopenten-1-one, 2-hydroxy-3-methy
13	5.295	5.215	5.325	17016373	1.56	3029137	1.75	5.62	V	Valeric acid, dodecyl ester
14	5.361	5.325	5.375	9777590	0.90	3430700	1.98	2.85	V	Phenol, 2-methyl- (CAS)
15	5.460	5.375	5.525	33776866	3.09	4053820	2.34	8.33	V	(+)-(S)-5-Hydroxymethyloxolan-2-one
16	5.589	5.525	5.690	63672907	5.83	9908070	5.73	6.43	V	Phenol, 4-methoxy- (CAS)
17	5.746	5.690	5.845	33397921	3.06	4712775	2.72	7.09	V	anhydro - sugar
18	5.905	5.845	6.060	40947747	3.75	4342032	2.51	9.43	V	2-acetylcyclopentanone
19	6.079	6.060	6.150	9008651	0.82	1834361	1.06	4.91	V	Phenol, 3,4-dimethyl- (CAS)
20	6.191	6.150	6.295	12762488	1.17	1756830	1.02	7.26	V	Phenol, 2,5-dimethyl- (CAS)
21	6.347	6.295	6.465	27734490	2.54	4372913	2.53	6.34	V	Phenol, 4-ethyl-
22	6.496	6.465	6.575	13655092	1.25	2955117	1.71	4.62	V	Creosol
23	6.661	6.575	6.705	18771270	1.72	2934458	1.70	6.40	V	Guanosine (CAS)
24	6.761	6.705	6.805	22358607	2.05	4639350	2.68	4.82	V	.GAMMA. HEXALACTONE
25	6.854	6.805	6.980	38653024	3.54	5245460	3.03	7.37	V	1,2-Benzenediol (CAS)
26	7.035	6.980	7.155	23032074	2.11	2873123	1.66	8.02	V	3-Octanone (CAS)
27	7.189	7.155	7.235	13668173	1.25	4762838	2.75	2.87	V	Phenol, 4-ethyl-2-methoxy-
28	7.282	7.235	7.335	14745712	1.35	2994920	1.73	4.92	V	Cyclobutene-3,4-diol, tetramethyl-
29	7.415	7.335	7.465	20302134	1.86	3138672	1.81	6.47	V	Ribofuranose, 1,5-anhydro-2,3-O-isoprop
30	7.491	7.465	7.515	7634023	0.70	2700673	1.56	2.83	V	2-Methoxy-4-vinylphenol
31	7.573	7.515	7.690	27482430	2.52	3022057	1.75	9.09	V	Isonicotinic acid, 2-ethylcyclohexyl ester
32	7.763	7.690	7.835	26309128	2.41	5985586	3.46	4.40	V	Phenol, 2,6-dimethoxy- (CAS)
33	7.874	7.835	7.890	7872913	0.72	2583158	1.49	3.05	V	2,5-Monoformal-l-rhamnitol
34	7.914	7.890	7.935	6764880	0.62	2630157	1.52	2.57	V	1-HEXADECANOL
35	7.965	7.935	7.985	7448082	0.68	2541648	1.47	2.93	V	1,3-Benzenediol, 5-methyl- (CAS)
36	8.007	7.985	8.090	14619741	1.34	2590368	1.50	5.64	V	1,2-Dioxolan-3-one, 5,5-diethyl-4-methyl
37	8.109	8.090	8.155	7592928	0.70	2210115	1.28	3.44	V	3-Octenoic acid, decyl ester
38	8.212	8.155	8.250	13210590	1.21	2984106	1.73	4.43	V	BENZALDEHYDE, 4-HYDROXY-3-MI
39	8.285	8.250	8.360	14736121	1.35	2870812	1.66	5.13	V	N1-(4-hydroxybutyl)-N3-methylguanidin
40	8.439	8.360	8.630	23778147	2.18	2479243	1.43	9.59	V	1,2,4-Trimethoxybenzene
41	8.665	8.630	8.715	4141267	0.38	845945	0.49	4.90	V	7,8,12-Tri-O-acetyl ingol
42	8.817	8.715	8.920	11012239	1.01	1102458	0.64	9.99	V	5-Hepten-3-yn-2-ol, 6-methyl-5-(1-methy
43	8.975	8.920	8.995	4107219	0.38	1083123	0.63	3.79	V	Benzene, 1,2,3-trimethoxy-5-methyl-
44	9.139	8.995	9.405	50115653	4.59	3923215	2.27	12.77	V	D-Allose
45	9.435	9.405	9.450	1406432	0.13	528096	0.31	2.66	V	Benzenepropanoic acid, 4-hydroxy-, meth
46	9.476	9.450	9.530	2613812	0.24	594681	0.34	4.40	V	Phenol, 2,6-dimethoxy-4-(2-propenyl)- ((
47	9.582	9.530	9.740	6204885	0.57	799185	0.46	7.76	V	4-Octanol, 7-methyl-, acetate
48	9.797	9.740	9.825	1586365	0.15	337389	0.20	4.70	V	(E)-2,6-Dimethoxy-4-(prop-1-en-1-yl)pha
49	9.845	9.825	9.915	1468648	0.13	294468	0.17	4.99	V	1-Nitro-.beta.-d-arabinofuranose, tetraace
50	9.954	9.915	10.065	2823452	0.26	374031	0.22	7.55	V	Benzaldehyde, 4-hydroxy-3,5-dimethoxy-
51	10.115	10.065	10.255	2483878	0.23	296098	0.17	8.39	V	Phenol, 2,6-dimethoxy-4-(2-propenyl)- ((
52	10.281	10.255	10.345	936257	0.09	186618	0.11	5.02	V	1-Octanol, 2,2-dimethyl- (CAS)
53	10.376	10.345	10.455	1181354	0.11	238405	0.14	4.96	V	Ethanone, 1-(4-hydroxy-3,5-dimethoxyph
54	10.499	10.455	10.535	808950	0.07	220119	0.13	3.68	V	9-EICOSENE, (E)-
55	10.560	10.535	10.770	1150074	0.11	251132	0.15	4.58	V	3,5-Dimethoxy-4-hydroxyphenylacetic ac
56	10.879	10.835	10.920	112966	0.01	51678	0.03	2.19		Ethanone, 1-(4-hydroxy-3,5-dimethoxyph
57	11.249	11.210	11.280	90091	0.01	65457	0.04	1.38		Tetratriacontane (CAS)
58	11.497	11.445	11.540	508851	0.05	250023	0.14	2.04		9-Octadecenoic acid (Z)- (CAS)
59	11.550	11.540	11.580	27906	0.00	22910	0.01	1.22	V	2-Butoxysulfonylhexadecane
60	12.095	12.065	12.265	161337	0.01	23943	0.01	6.74		Trichloroacetic acid, pentadecyl ester
61	12.404	12.370	12.470	116498	0.01	38438	0.02	3.03		9,12-Octadecadienoic acid (Z,Z)- (CAS)
62	13.128	13.095	13.175	59028	0.01	34122	0.02	1.73		METHYL ESTER OF RICINOLEIC AC
63	13.544	13.505	13.600	109571	0.01	41245	0.02	2.66		9-Octadecenamide (CAS)
				1092024541	100.00	172977680	100.00			